

Diagnostic studies of ion beam formation in inductively coupled plasma

mass spectrometry with the collision reaction interface

by

Jeneé L. Jacobs

A dissertation submitted to the graduate faculty
in partial fulfillment of the requirements for the degree of

DOCTOR OF PHILOSOPHY

Major: Analytical Chemistry

Program of Study Committee:
Robert S. Houk, Major Professor
Young-Jin Lee
Emily Smith
Patricia Thiel
Javier Vela

Iowa State University

Ames, Iowa

2015

Copyright © Jeneé L. Jacobs, 2015. All right reserved.

TABLE OF CONTENTS

ABSTRACT	vi
CHAPTER 1. GENERAL INTRODUCTION	1
Inductively Coupled Plasma Mass Spectrometry	1
ICP	1
Ion Extraction	3
Polyatomic Ion Interferences	4
Polyatomic Ion Mitigation Techniques	5
Characteristics of Collision Technology	7
Dissertation Organization	8
References	9
Figures	14
CHAPTER 2. UPDATED IONIZATION EFFICIENCY CALCULATIONS FOR INDUCTIVELY COUPLED PLASMA MASS SPECTROMETRY	16
Abstract	16
Introduction	16
Theory	19
Saha equation for singly charged ions	21
Saha equation for doubly charged ions	22
Ionization of metal oxide molecules	22
Dissociation of metal oxide ions	23
Updated ionization efficiency tables for singly charged ions	24
Ionization efficiency tables of doubly charged ion formation	25
Metal oxide ionization and dissociation	27

Conclusion	28
References	29
Tables	33
Figures	34
CHAPTER 3. FUNDAMENTALS OF THE COLLISION REACTION INTERFACE IN INDUCTIVELY COUPLED PLASMA MASS SPECTROMETRY: USING ION KINETIC ENERGIES TO CHARACTERIZE THE CRI COLLISION REGION	39
Abstract	39
Introduction	39
Experimental	43
Solutions and materials	43
Determination of ion collision cross-sections using hexapole collision cell	43
Determination of CRI dimensions and conditions	44
Results and discussion	45
Determination of ion collision cross-sections using hexapole collision cell	45
Determination of the CRI dimensions and conditions	50
Conclusion	53
Acknowledgements	54
References	54
Tables	58
Figures	61
CHAPTER 4. THE FORMATION OF SECONDARY METAL MONOHYDRIDE IONS IN ICP-MS WITH THE COLLISION REACTION INTERFACE	66
Abstract	66
Introduction	66

Experimental	69
Reagents and materials	69
Instrumentation	70
Results and discussion	71
Comparison of background spectra	71
Formation of metal monohydride (MH ⁺) ions	72
Contribution of the ion optics to MH ⁺ ion levels	74
Kinetic energy comparison of MH ⁺ ions and M ⁺ ions	75
Conclusion	77
Acknowledgements	79
References	79
Tables	81
Figures	82
CHAPTER 5. GENERAL CONCLUSIONS	86
APPENDIX A. GIANT MAGNETIC ANISOTROPY AND TUNNELLING OF THE MAGNETIZATION OF Li₂(Li_{1-x}Fe_x)N	88
Abstract	88
Introduction	89
Results	91
Basic properties of Li ₂ (Li _{1-x} Fe _x)N	91
Magnetization	92
Relaxation	95
Discussion	98
Methods	103
Crystal growth	103
Chemical analysis – ICP-MS	104
References	105
Figures and Tables	109

APPENDIX B. ALTERNATING MAGNETIC ANISOTROPY OF $\text{Li}_2(\text{Li}_{1-x}\text{T}_x)\text{N}$ WITH T = Mn, Fe, Co AND Ni	115
Abstract	115
Body	115
Acknowledgments	123
References	124
Figures and Table	126
ACKNOWLEDGEMENTS	130

ABSTRACT

This dissertation describes a variety of studies focused on the plasma and the ion beam in inductively coupled plasma mass spectrometry (ICP-MS). The ability to use ICP-MS for measurements of trace elements in samples requires the analytes to be efficiently ionized. Updated ionization efficiency tables are discussed for ionization temperatures of 6500 K and 7000 K with an electron density of $1 \times 10^{15} \text{ cm}^{-3}$. These values are reflective of the current operating parameters of ICP-MS instruments. Calculations are also discussed for doubly charged (M^{2+}) ion formation, neutral metal oxide (MO) ionization, and metal oxide (MO^+) ion dissociation for similar plasma temperature values. Ionization efficiency results for neutral MO molecules in the ICP have not been reported previously.

The collision reaction interface (CRI) removes polyatomic ions in ICP-MS by introducing a collision or reaction gas directly into the plasma expansion as ions are extracted into the mass spectrometer. The main gases implemented in CRI are helium and hydrogen. Experiments are described for the determination of the collision cross sections of singly charged cations by employing helium in a hexapole collision cell. Based on those determined cross sections, general characteristics of the CRI collision region are determined and discussed using helium as a collision gas. One concern with implementing H_2 as a reaction gas via the CRI is the possible formation of monohydride ions (MH^+ , $M = \text{atomic ion}$). The formation of MH^+ ions and the influence of increasing H_2 gas flow through the CRI skimmer cone are discussed to provide insight into the source of MH^+ ion formation in the CRI and plasma expansion regions.

CHAPTER 1. GENERAL INTRODUCTION

Inductively Coupled Plasma Mass Spectrometry

Inductively coupled plasma mass spectrometry (ICP-MS) is a commonly used analytical technique for elemental analysis. The main advantages of ICP-MS are ultra-trace detection limits in solution, ranging as low as parts-per-quadrillion (ppq), and a wide linear dynamic range spanning up to 8 orders of magnitude [1, 2]. Many elements can also be determined within a single sample under one set of plasma conditions with only slight compromise. Many areas employ ICP-MS for elemental analysis, including environmental chemistry [3, 4], geology [5], agriculture and food science [6, 7], biomedical and pharmaceuticals [8, 9], semiconductors [10], nuclear chemistry [11], and forensics [12]. ICP-MS is also commonly hyphenated with other instrumentation, such as ion chromatography [13], gas chromatography [14], and high performance liquid chromatography [15], for speciation information beyond general elemental composition. Solid samples can be analyzed directly and non-destructively by coupling laser ablation to ICP-MS [16].

ICP

The ICP plays a very important role in ICP-MS. The ICP is most commonly generated from argon gas. Three concentric gas flows (Figure 1) comprised of the outer gas, the auxiliary gas, and the sample gas are implemented to maintain the plasma. The outer gas cools the outer wall of the torch and supports the plasma. The auxiliary gas protects the injector portion of the torch. The sample gas carries the nebulized sample into the central portion of the plasma [1]. The plasma is formed by an induced electromagnetic field from the RF load coil, which

accelerates free electrons and ionizes approximately 0.1% of the argon gas [1]. The characteristics of the ICP, specifically the temperature and composition, determine the efficiency of analyte ionization, which, in turn, determines the ability to measure an analyte ion.

The inner-most region of the plasma, also known as the axial channel, is comprised of four distinct zones (Figure 1): the preheating zone (PHZ), the initial radiation zone (IRZ), the normal analytical zone (NAZ), and the plasma tail [17]. The sample is typically introduced into the axial channel as aerosol droplets of a nebulized solution. The droplets are vaporized in the PHZ, atomized in the IRZ, ionized in the NAZ, and then further reacted to form additional neutral atoms and oxides in the plasma tail [17, 18]. The region of the NAZ near the end of IRZ is the optimum sampling position within the plasma for analyte ion signal. At this position, analyte ions are highly abundant for many elements simultaneously. This is a key property for multielement analysis in ICP-MS. The ionization temperature (T_{ion}) of the NAZ is generally 6500 K to 7500 K [19, 20, 21]. T_{ion} is a measured value that corresponds to an ionization constant based on measured ion signal ratios [18].

The composition of the NAZ varies with the addition of supplemental gases and high concentration analyte ions; however, the most common and abundant constituents are argon, hydrogen, oxygen, and nitrogen [1]. These constituents are ionized generating a population of ions and electrons within the NAZ. The ionization reactions maintained within the plasma are generally represented as:



$$K_{ion} = \frac{(n_{X^+})(n_e)}{(n_X)} \quad (2)$$

where X represents the constituents. The ionization equilibrium constant, K_{ion} , is the relationship between the density of the ions (n_{X^+}), the density of electrons (n_e), and the density of the atoms (n_X) in the plasma. K_{ion} is dependent on T_{ion} . The density of electrons at the usual sampling position in the plasma is generally $1 \times 10^{15} \text{ cm}^{-3}$ to $2 \times 10^{15} \text{ cm}^{-3}$ [22, 19, 23]. These n_e values have been measured by several techniques, including Stark broadening of the H_β emission line, Thomson scattering, and Saha calculations [22, 19, 23, 24, 25, 26].

Using statistical mechanics, Saha derived an equation relating the degree of ionization of an atom to T_{ion} and n_e . Variations of the Saha equation for ionization (Equation 3), which are described further in Chapter 2, can be used to calculate the population of all ions in the ICP, including doubly charged and polyatomic ions.

$$\left(\frac{n_{M^+}n_e}{n_M}\right) = 2 \left(\frac{2\pi m_e k T_{ion}}{h^2}\right)^{3/2} \left(\frac{Z_{M^+}}{Z_M}\right) e^{(-IE(M)/kT_{ion})} \quad (3)$$

In this equation, n_{M^+} and n_M are the densities (cm^{-3}) of ions and atoms, respectively, m_e is the mass of an electron, Z_{M^+} and Z_M are the partition functions of the ion and atom, respectively, $IE(M)$ is the ionization energy (eV), and T_{ion} is the ionization temperature (K) at the sampling position within the plasma [27, 28].

Ion Extraction

After atomization and ionization, the central portion of the plasma is extracted into the MS via coaxial circular apertures in the sampler and skimmer cones. The sampler cone is positioned in the NAZ to transmit optimum levels of singly charged ions into the mass spectrometer. Behind the sampler, an interface pump reduces the pressure almost three orders of

magnitude to ~1 mbar. This drop in pressure causes a supersonic expansion of the ions, also known as a free jet [29]. In this free jet, the density of gas decreases on the same order as pressure, the temperature drops, and the flow speed is increased to exceed the speed of sound [29]. The skimmer cone is positioned within the free jet to achieve the highest ion signals.

The free jet is surrounded by a barrel shock that results in a shockwave as the supersonic expansion meets the skimmer face (Figure 2) [18]. If the skimmer were not present, an additional shockwave, known as a Mach disc, would form resulting in a “mess” of recombination reactions, formation reactions, and general scatter of analyte ions [18, 29]. The position of the skimmer cone gives the best neutral beam intensity while avoiding this “mess” of additional ions possible with the formation of a Mach disc [29]. The pressure beyond the skimmer cone is approximately 4 orders of magnitude lower than the pressure between the sampler and skimmer cones. This pressure is now low enough that ions can be focused without collisions with background gas and a sufficient ion beam is formed. After extraction, the ion beam is shaped, directed, and analyzed by the mass analyzer.

Polyatomic Ion Interferences

Polyatomic ions cause spectral interferences in ICP-MS analyses. If the plasma was hot enough to dissociate all polyatomic ions completely, the temperature would also be high enough to form very high levels of multiply charged ions, which are also undesirable. Polyatomic ions are problematic because they have the same nominal mass-to-charge ratio (m/z) as other analyte ions of interest, which prevents accurate quantification.

Although the temperature of the plasma is high enough to extensively atomize most molecules, large amounts of polyatomic ions from the main plasma constituents persist, such as

ArH^+ , H_3O^+ , H_2O^+ , NO^+ , O_2^+ , OH^+ , Ar_2^+ , and Ar_2H^+ [30]. With the addition of sample, polyatomic ions of the matrix or analytes are often formed as well. Polyatomic ions are suspected to arise from either incomplete atomization in the ICP or reactions during the extraction process into the mass spectrometer, especially in the first ~ 1 mm behind the sampler [31]. The most significant polyatomic ions from the sample are oxides (MO^+) of the atomic ions; however, argides (MAr^+), nitrides (MN^+), chlorides (MCl^+), and others can be significant as well [32]. Metal monohydride ions (MH^+) are discussed in detail in Chapter 4. Present-day instruments cannot resolve MH^+ ions from M^+ ions at the same nominal m/z value (e.g. $^{238}\text{UH}^+$ from $^{239}\text{Pu}^+$ [33]) for $M > 100$ g/mole, including high resolution instrumentation.

The abundance of polyatomic ions in the plasma can vary with instrumental parameters and the amount of background atoms introduced by entrained air and the matrix solution. Many studies have been performed relating the abundance of polyatomic ions to plasma potential, plasma gas make-up, sample gas flow, and mass spectrometer settings [34, 35].

Polyatomic Ion Mitigation Techniques

Removal or reduction of polyatomic ions as interferences in ICP-MS has become a priority for accurate analyses, especially for problematic elements like Cr ($^{52}\text{Cr}^+$ from $^{40}\text{Ar}^{12}\text{C}^+$), Fe ($^{56}\text{Fe}^+$ from $^{40}\text{Ar}^{16}\text{O}^+$), As ($^{75}\text{As}^+$ from $^{40}\text{Ar}^{35}\text{Cl}^+$) and Se ($^{80}\text{Se}^+$ from $^{40}\text{Ar}_2^+$). High resolution instrumentation is capable of separating most polyatomic ions and analyte ions with resolution capabilities of $m/\Delta m$ equal to 10000 or more [36]. However, the cost and complexity of this instrumentation is high. Also, some polyatomic ions require much higher resolution for separation, i.e. SrO^+ from Ru^+ requires a resolution of ~ 24000 , which is not feasible with commercially available ICP-MS instruments.

Low resolution quadrupole mass spectrometers generally cannot separate polyatomic and analyte ions via the mass analyzer alone. These instruments are operated with unit mass resolution. As a result, low resolution instruments requires additional internal components to remove polyatomic ion interferences prior to ion detection.

Collision methods are the most common interference mitigation technique of choice in low resolution quadrupole instrumentation. Various collision technologies are available for this purpose; the most common is the multipole collision cell. A collision cell is an enclosed set of quadrupole, hexapole, or octopole rods placed between the skimmer and the mass analyzer. Within the enclosed region of the collision cell, a desired gas can be introduced to induce collisions between the generated ions from the plasma and the collision gas. Collisions lead to either chemical reactions that remove the undesired polyatomic ion, or reduction of the kinetic energies of the unwanted polyatomic ions much more than those of the desired atomic analyte ions at the same nominal m/z value. The latter concept is known as kinetic energy discrimination [37].

Kinetic energy discrimination (KED) uses collisions to dampen the ion energies of the larger polyatomic ions, which prevents the ions from being efficiently transmitted by the subsequent mass analyzer [38]. KED has been efficiently used to remove interferences for accurate quantification of many elements, including titanium, chromium, arsenic, potassium, and iron, which can often be difficult to measure using low resolution ICP-MS instrumentation [39, 40, 41, 42, 43]. Helium is often used for the removal of polyatomic ions in this manner [44]. Reactive gases, on the other hand, convert troublesome polyatomic ions to species at a different m/z value. A variety of reactive gases are available. Hydrogen (H_2) is commonly used on various instruments for the removal of argon adducts, such as ArO^+ , ArN^+ , Ar_2^+ and $ArCl^+$,

which are often present in abundance due to the argon plasma gas [45]. H_2 is preferred as a reaction gas because it is highly reactive and has a low mass which leads to small losses due to collisional scattering.

Another collision technology available, but less widely implemented, is the collision reaction interface (CRI). The premise behind CRI technology is very similar to that of the collision cell. Interference ions are still removed via either KED with He or reactions via a reactive gas, usually H_2 . However, the CRI introduces the collision gas directly into the plasma expansion either at the tip of the sampler and/or skimmer cones [46]. Implementation of a collision or reaction gas directly in the plasma expansion region is advantageous because the region is very small with a high gas density, which increases the likelihood of many collisions [46].

Characteristics of Collision Technology

The characteristics of the collision region within collision cells have been studied quite extensively [39]. The gas density within the collision cell can be determined based on the incoming gas pressure or flow rate, the internal flow regime, and the conductances of the collision cell openings [47]. The dimensions of the collision cell can be determined by physical measurements of the collision cell components. These known characteristics are discussed further in Chapter 3 and are used to determine the collision cross sections of monatomic and polyatomic ions.

Unlike the collision cell, the characteristics of the CRI collision region are not as well known. The collisions occur within a small region at the tip of the sampler and/or skimmer cones. However, the density of gas within that region and the length are not identified in the

literature. In Chapter 3, collision cross sections are measured and used to estimate the dimensions of the CRI collision region and characterize the density of the collision gas with varying gas flow rates.

Dissertation Organization

This dissertation is organized into five chapters and two appendices. The first chapter is a general introduction to ICP-MS, more specifically the ICP, the ion beam, and polyatomic ion interferences. Chapters 2, 3, and 4 are manuscripts prepared to be submitted for publication. Chapter 2 discusses updated calculations for the degree of ionization within an inductively coupled plasma at ionization temperatures of 6500 K and 7000 K. These updated calculations are an improvement upon original published values by R. S. Houk [48]. Chapter 3 examines the measurement of collision cross sections of monatomic ions. These values are then, in turn, used to characterize the collision reaction interface (CRI). The CRI is a relatively new collision technology in ICP-MS about which very little information is known. Chapter 4 discusses the formation of metal monohydride (MH^+) ion via reactions of H_2 with ions from the plasma in the CRI. Chapter 5 summarizes the conclusions from the above studies and presents further implications of this work. Appendix A is a paper published in Nature Communications for which I contributed chemical analysis for the characterization of magnetic $Li_2(Li_{1-x}Fe_x)N$ compounds. Appendix B is a paper published in Physical Review B for which I contributed chemical analysis for the characterization of magnetic $Li_2(Li_{1-x}T_x)N$ compounds with $T = Mn, Fe, Co, \text{ and } Ni$.

References

- [1] K. E. Jarvis, A. L. Gray, R. S. Houk, Handbook of Inductively Coupled Plasma Mass Spectrometry, New York: Blackie & Son Ltd, 1992.
- [2] A. Montaser, Inductively Coupled Plasma Mass Spectrometry, New York: Wiley-VCH, Inc., 1998.
- [3] M. Pettine, T. J. McDonald, M. Sohn, G. A. K. Anquandah, R. Zboril, V. K. Sharma, A critical review of selenium analysis in natural water samples, Trends Environ. Anal. Chem. 5 (2015) 1-7.
- [4] W. Guo, S. Hu, J. Zhang, L. Jin, X. Wang, Z. Zhu, H. Zhang, Soil monitoring of arsenic by methanol addition DRC ICP-MS after boiling aqua regia extraction, J. Anal. At. Spectrom.. 26 (2011) 2076-2080.
- [5] Q. Li, R. R. Parrish, M. S. Horstwood, J. M. McArthur, U-Pb dating of cement in Mesozoic ammonites, Chemical Geol. 376 (2014) 76-83.
- [6] J. S. Becker, K. Fuellner, U. D. Seeling, G. Fornalczyk, A. J. Kuhn, Measuring magnesium, calcium, and potassium isotope ratios using ICP-QMS with an octopole collision cell in tracer studies of nutrient uptake and translocation in plants, Anal. Bioanal. Chem. 390 (2008) 571-578.
- [7] C. M. Moreira, F. A. Duarte, J. Leberherz, D. Pozebon, E. M. M. Flores, V. L. Dressler, Arsenic speciation in white wine by LC-ICP-MS, Food Chem. 126 (2011) 1406-1411.
- [8] Y. Koyama, Y. Matsui, Y. Shimada, M. Yoneda, Biodistribution of gold nanoparticles in mice and investigation of their possible translocation by nerve uptake around the alveolus, J. Toxicol. Sci. 40 (2015) 243-249.
- [9] A. Sussulini, J. S. Becker, Application of laser microdissection ICP-MS for high resolution elemental mapping in mouse brain tissue: A comparative study with laser ablation ICP-MS, Talanta 135 (2015) 579-582.
- [10] J. P. Leitao, N. M. Santos, P. A. Fernandes, P. M. P. Salome, A. F. da Cunha, J. C. Gonzales, F. M. Matinaga, Study of optical structural properties of Cu₂ZnSnS₄ thin films, Thin Solid Films 519 (2011) 7390-7393.
- [11] S. Boulyga, S. Konegger-Kappel, S. Richter, L. Sangely, Mass spectrometric analysis for nuclear safeguards, J. Anal. At. Spectrom. Accepted Manuscript (2015).

- [12] A.-C. Lindstrom, J. Hoogewerff, J. Athens, Z. Obertova, W. Duncan, N. Waddell, J. Kieser, Gunshot residue preservation in seawater, *Forens. Sci. Int.* Accepted Manuscript (2015).
- [13] R. Lohmayer, G. M. S. Reithmaier, E. Bura-Nakic, B. Planer-Fredrich, Ion-pair chromatography coupled to inductively coupled plasma-mass spectrometry (IPC-ICP-MS) as a method of thiomolybdate speciation in natural waters, *Anal. Chem.* 87 (2015) 3388-3395.
- [14] Y. L. Sommer, C. P. Verdon, M. R. Fresquez, C. D. Ward, E. B. Wood, Y. Pan, K. L. Caldwell, R. L. Jones, Measurement of mercury species in human blood using triple spike isotope dilution with SPME-GC-ICP-DRC-MS, *Anal. Bioanal. Chem.* 406 (2014) 5039-5047.
- [15] J. Sancar, B. Berlinger, Y. Thomassen, R. Milacic, Simultaneous speciation analysis of chromate, molybdate, tungstate and vandate in welding fume alkaline extracts by HPLC-ICP-MS, *Talanta* 142 (2015) 164-169.
- [16] A. Bengtson, M. Gransfors, I. Gustavsson, M. Sedlakova, P. I. Gomez, H. Dillen, K. Van den Bergh, D. Gunther, C. Latkoczy, High spatial resolution analysis of steel samples using laser ablation ICP-MS, *Eur. Commission* (2006) 1-154.
- [17] S. R. Koirtyohann, J. S. Jones, D. A. Yates, Nomenclature system for the low-power argon inductively coupled plasma, *Anal. Chem.* 52 (1980) 1966-1968.
- [18] H. Niu, R. Houk, Fundamental aspects of ion extraction in inductively coupled plasma mass spectrometry, *Spectrochim. Acta Part B* (1996) 779-815.
- [19] R. S. Houk, Y. Zhai, Comparison of mass spectrometric and optical measurements of temperature and electron density in the inductively coupled plasma during mass spectrometric sampling, *Spectrochim. Acta Part B* 56 (2001) 1055-1067.
- [20] M. Aghaei, H. Lindner, A. Bogaerts, Optimization of operating parameters for inductively coupled plasma mass spectrometry: a computational study, *Spectrochim. Acta Part B* 76 (2012) 56-64.
- [21] P. Serapinas, J. Salkauskas, Z. Ezerinskis, A. Acus, Local thermodynamic equilibrium modeling of ionization of impurities in argon inductively coupled plasma, *Spectrochim. Acta Part B* 65 (2010) 15-23.
- [22] T. Hasegawa, H. Haraguchi, A. Montaser, D. W. Golightly, Fundamental Properties of Inductively Coupled Plasmas, in: A. Montaser, D.W. Golightly, *Inductively Coupled Plasmas in Analytical Atomic Spectroscopy*, New York, VCH, 1987, pp. 267-321.

- [23] R. S. Houk, H. J. Svec, V. A. Fassel, Mass Spectrometric Evidence for Spurathermal Ionization in an Inductively Coupled Argon Plasma, *Appl.Spectrosc.* 35 (1981) 380-384.
- [24] H. Niu, R. S. Houk, Langmuir probe measurements of the ion extraction process in inductively coupled plasma mass spectrometry - I. Spatially resolved determination of electron density and electron temperature, *Spectrochim. Acta* 49B (1994) 1283-1303.
- [25] S. A. Lehn, K. A. Warner, M. Huang, G. M. Heiftje, Effect of an inductively coupled plasma mass spectrometry sampler interface on electron temperature, electron number density, and gas-kinetic temperature and analyte emission intensity upstream in the plasma, *Spectrochim. Acta Part B* 57 (2002) 1739-1751.
- [26] G. Gamez, S. A. Lehn, M. Huang, G. M. Heiftje, Effect of mass spectrometric sampling interface on the fundamental parameters of an inductively coupled plasma as a function of its operating conditions: Part II. Central-gas flow rate and sampling depth, *Spectrochim. Acta Part B* 62 (2007) 370-377.
- [27] A. Thorne, U. Litzen, S. Johansson, *Spectrophysics: Principles and Applications*, New York: Springer, 1999.
- [28] A. P. Thorne, *Spectrophysics*, New York: Chapman and Hall, 1974.
- [29] D. J. Douglas, J. B. French, Gas dynamics of the inductively coupled plasma mass spectrometry interface, *J. Anal. At. Spec.* 3 (1988) 743-747.
- [30] R. S. Houk, V. A. Fassel, G. D. Flesch, H. J. Svec, A. L. Gray, C. E. Taylor, Inductively couple argon plasma as an ion source for mass spectrometric determination of trace elements, *Anal. Chem.* 52 (1980) 2283-2289.
- [31] R. S. Houk, N. Praphairaksit, Dissociation of polyatomic ions in the inductively coupled plasma, *Spectrochim. Acta Part B* 56 (2001) 1069-1096.
- [32] D. J. Douglas, S. D. Tanner, Fundamental considerations in ICPMS, in: A. Montaser, *Inductively coupled plasma mass spectrometry*, New York, Wiley-VCH, Inc., 1998, pp. 615-679.
- [33] R. N. Taylor, T. Warneke, J. A. Milton, I. W. Croudace, P. E. Warwick, R. W. Nexbitt, Plutonium isotope ratio analysis in femtogram to nanogram levels by multicollector ICP-MS, *J. Anal. At. Spectrom.* 16 (2001) 279-284.
- [34] C. H. Ebert, T. M. Witte, R. S. Houk, Investigation into the behavior of metal-argon polyatomic ion ($M\text{Ar}^+$) in the extraction region of inductively coupled plasma-mass spectrometry, *Spectrochim. Acta Part B* 76 (2012) 119-125.

- [35] T. M. Witte, R. S. Houk, Origins of polyatomic ions in laser ablation-inductively coupled plasma-mass spectrometry: An examination of metal oxide ions and effects of nitrogen and helium in the herosol gas flow, *Spectrochim. Acta Part B* 69 (2012) 9-19.
- [36] N. Bradshaw, E. F. H. Hall, N. E. Sanderson, Inductively coupled plasma as an ion source for high-resolution mass spectrometry, *J. Anal. At. Spectrom.* 4 (1989) 801-803.
- [37] N. Yamada, J. Takahashi, K. Sakata, The effects of cell-gas impurities and kinetic energy discrimination in an octopole collision cell ICP-MS under non-thermalized conditions, *J. Anal. At. spectrom.* 17 (2002) 1213-1222.
- [38] D. J. Douglas, J. B. French, Collisional focusing effects in radio frequency quadrupoles, *J. Am. Soc. Mass Spectrom.* 3 (1992) 398-408.
- [39] S. D. Tanner, V. I. Baranov, D. R. Bandura, Reaction cells and collision cells for ICP-MS: a tutorial review, *Spectrochim. Acta Part B* 57 (2002) 1361-1452.
- [40] S. Zhang, W.-h. Zhang, Z.-r. Li, Z.-g. Jiang, J.-t. Wang, F.-l. Liang, New dry ashing-wet digestion method and ICP-MS determine the content of titanium dioxide in foods, *Shipin Yanjiu Yu Kaifa* 34 (2013) 77-80.
- [41] W. Cieslak, K. Pap, D. R. Bunch, E. Reineks, R. Jackson, R. Steinle, S. Wang, Highly sensitive measurement of whole blood chromium by inductively coupled plasma mass spectrometry, *Clin. Biochem.* 46 (2013) 266-270.
- [42] A. Liba, Transforming ICP-MS technology: advances in interference removal for accurate arsenic analysis in food and beverages, in *Abstract of Paper, 245th ACS National Meeting & Exposition, New Orleans, LA, 2013.*
- [43] N. I. Rousis, I. N. Pasiadis, N. S. Thomaidis, Attenuation of interference in collision/reaction cell inductively coupled plasma mass spectrometry, using helium and hydrogen as cell-gases - application in multi-element analysis of mastic gum, *Anal. Methods* 6 (2014) 5899-5908.
- [44] X. Wang, I. Kalinitchenko, *Fundamental and Practical Aspects of the CRI Technology for ICP-MS*, (2007).
- [45] J. T. Larsen, I. Kalinitchenko, Eliminating ICP-MS Interferences with Kinetic Energy Discrimination CRI and 3D Ion Mirror, 22 January 2014. [Online]. Available: https://www.bruker.com/fileadmin/user_upload/8-PDF-Docs/Separations_MassSpectrometry/Literature/literature/Presentations/PWC14_JoernLarsenCRI.pdf. [Accessed 9 April 2015].

- [46] C. D. Pereira, E. E. Garcia, F. V. Silva, A. A. Nogueira, J. A. Nobrega, Behaviour of Arsenic and Selenium in an ICP-QMS with Collision and Reaction Interface, *J. Anal. At. Spectrom.* 25 (2010) 1763-1768.
- [47] Leybold-Heraeus Vacuum Products Inc., *Vacuum Technology, Its Foundations, Formulae and Tables*, 2001.
- [48] R. S. Houk, Mass Spectrometry of Inductively Coupled Plasmas, *Anal.Chem.* 58 (1986) 97A-105A.

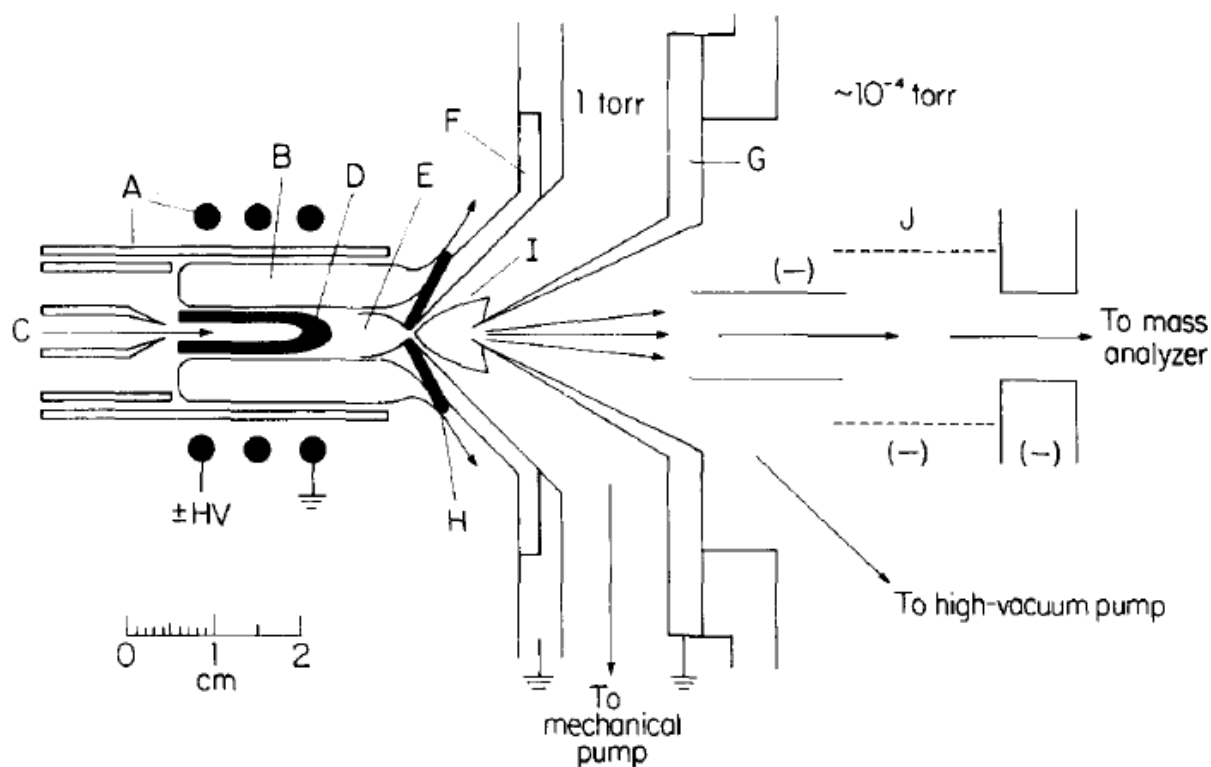


Figure 1: A schematic of the plasma torch, plasma, and ion extraction process. A – Plasma Torch and RF Load Coil, B – Outer Gas Region, C – Central Plasma Gas Flow, D – IRZ, E – NAZ, F – Sampler Cone, G – Skimmer Cone, H – Boundary Layer from Gases, I – Supersonic Expansion, J – Ion Lenses. Reproduced from reference [18] with permission.

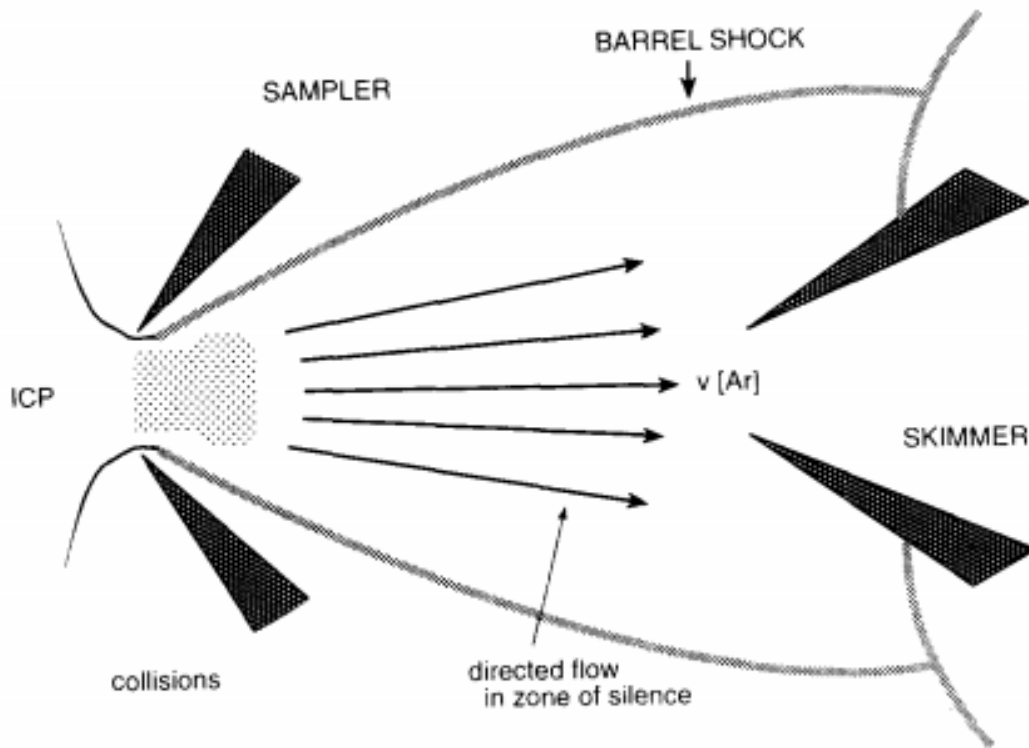


Figure 2: The supersonic expansion of the plasma between the sampler and skimmer. The free jet is surrounded by a barrel shock that results in a shockwave as the supersonic expansion meets the skimmer face. (From Reference [18] with Permission)

CHAPTER 2. UPDATED IONIZATION EFFICIENCY CALCULATIONS FOR INDUCTIVELY COUPLED PLASMA MASS SPECTROMETRY

Jeneé L. Jacobs and R.S. Houk

Abstract

The ability to use inductively coupled plasma mass spectrometry (ICP-MS) for measurements of trace elements in samples requires the analyte elements to be efficiently ionized at the sampling position in the ICP. Tables containing the ionization efficiencies for many of the element on the periodic table at an ionization temperature (T_{ion}) of 7500 K and an electron density (n_e) of $1 \times 10^{15} \text{ cm}^{-3}$ were published in the mid-1980s. The normal operating parameters of ICP-MS instruments have changed to some extent since, and plasma temperatures have changed as well. Updated ionization efficiency tables are discussed in this work for ionization temperatures of 6500 K and 7000 K with an electron density of $1 \times 10^{15} \text{ cm}^{-3}$. Calculations are also discussed for doubly charged (M^{2+}) ion formation, neutral metal oxide (MO) ionization, and metal oxide (MO^+) ion dissociation for similar plasma temperature values. Ionization efficiency results for neutral MO molecules in the ICP have not been reported previously.

Introduction

The ICP has become an invaluable ion source for multielement analysis. When coupled to mass spectrometry (MS), ultra-trace detection limits are often obtainable and quantification abilities often span a very wide linear dynamic range [1]. Many elements can also be analyzed within a single sample under one set of plasma conditions with only slight compromise.

In ICP-MS, the plasma plays a key role in the achievable analysis results. Without adequate atomization and ionization of the analytes of interest, the efficiency and applicability of ICP-MS would be greatly reduced. The extent of ionization is also important in ICP emission instruments. For most elements, the best emission lines are from M^+ ions rather than neutral atoms.

The plasma is generated from an argon gas flow and an applied radio-frequency (RF) power (Figure 1). The outer portion of the plasma is cooled by the outer gas flow to prevent the torch from melting. The upstream part of the induction region is thought to reach temperatures as high as 10000 K [2, 3]. The inner-most region of the plasma, also known as the axial channel, is comprised of four distinct zones: the preheating zone (PHZ), the initial radiation zone (IRZ), the normal analytical zone (NAZ), and the plasma tail [3]. The sample is generally introduced into the axial region as an aerosol of solution. The aerosol is vaporized in the PHZ, atomized in the IRZ, ionized in the NAZ, and then further reacted to form additional neutral atoms and oxides in the plasma tail [2, 3]. The region of the NAZ a few mm downstream from the tip of the IRZ is generally the optimum sampling position within the plasma for analyte ion (M^+) signal in ICP-MS. The plasma conditions (i.e., composition and temperature) within the NAZ are responsible for the efficiency of analyte ionization.

The NAZ of the plasma is comprised of several major constituents, mainly neutral atoms of Ar, H, O and possibly N [1]. These constituents are ionized generating a population of ions and electrons within the plasma region. The total particle density of these components (n_0 , atoms cm^{-3}) can be estimated from the ideal gas law.

$$n_0 = \frac{P}{RT_{gas}} \quad (1)$$

Typically, the plasma has a gas kinetic temperature (T_{gas}) ranging from 5000 K to 6000 K at a pressure (P) of 1 bar [2, 4, 5, 6]. These conditions lead to an approximate total particle density of $1.5 \times 10^{18} \text{ cm}^{-3}$ [1]. The fraction of this gas density contributed by electrons (n_e) in the plasma has been measured by several techniques, including Stark broadening of the H_{β} emission line, Thomson scattering, and Saha calculations [6, 7, 8, 9, 10, 11]. Electron density generally ranges from $1 \times 10^{15} \text{ cm}^{-3}$ to $2 \times 10^{15} \text{ cm}^{-3}$ at the sampling position used in ICP-MS [6, 7, 8, 9, 10, 11].

The ionization temperature (T_{ion}) of the plasma is generally a few hundred degrees above T_{gas} . T_{ion} ranges from 6500 K to 7500 K under hot plasma conditions and is dependent on the sampling position, the RF power, the argon gas flow, the solvent, and other instrumental settings [7, 12, 13]. Like all temperatures, T_{ion} corresponds to a particular ionization constant $K_{\text{ion}} = f(T_{\text{ion}})$, which can be determined from measured ion signal ratios and n_e [2]. Based on mass spectrometric measurements of T_{ion} , similar to those of Crain *et al.* [12], we have found the instruments in our laboratory to operate at an ionization temperature ranging from 6500 K to 7000 K.

Houk first published a table of ionization efficiencies in 1986 (Figure 2) [14]. Niu and Houk later republished this same table with greater explanation of the mathematical concepts involved in the calculation of ionization efficiency [2]. The ionization efficiencies in this table were calculated based on early measurements of T_{ion} for a T_{ion} of 7500 K and n_e of $1 \times 10^{15} \text{ cm}^{-3}$. Since these publications, many authors have cited these ionization efficiency values, as well as the mentioned plasma temperature and electron density, for research or calculation purposes (cited by references [15, 16, 17, 18, 19] and many others). For example, in the early days before 20 or 30 element standard solutions were available, the ionization efficiency values from

reference [14] were often used as provided for inter-element calibration in semi-quantitative analysis procedures, or for derivation of mass bias curves [1].

Updated ionization efficiencies are necessary because instrumentation and common optimization conditions have changed since 1986. For example, several studies have been performed to improve the robustness of plasmas for the measurement of elements in a variety of matrices [20]. These improvements lead to significant changes in the ionization temperature of the plasma which, in-turn, causes significant changes in the degree of ionization and the formation of other ionic species, such as doubly charged (M^{2+}) ions and metal oxide (MO^+) ions. M^{2+} ions are discussed in detail by Pupyshev and Semanova [21]; dissociation of MO^+ ions are discussed in detail by Houk and Praphairaksit [22].

This paper discusses the calculation of updated ionization efficiencies, including those for many elements not reported at the time of Niu and Houk's publication, at two plasma ionization temperature of 6500 K and 7000 K. The formation of M^{2+} ions, the degree of ionization of neutral MO molecules, and the degree of dissociation of MO^+ ions are also discussed for these updated normal "hot" plasma conditions.

Theory

A simple way to describe atomization and ionization conditions within the plasma is to use calculations based on plasma temperature. The main constituents of the injected sample elements most commonly exist as M^+ atomic cations; however, many may exist as neutral atoms (M), polyatomic MO^+ ions, or M^{2+} ions as well. The population of neutral M atoms is higher for injected sample elements with high ionization energies, i.e. As, Se, I, Hg, etc., at the usual

sampling position. In the NAZ, the population of the MO^+ and M^{2+} ions are small in comparison to the population of M^+ ions.

The most common ionization reactions maintained within the plasma are as follows:



These reactions (equations 2-7) and all other reactions present in the plasma, generally represented by $A \rightleftharpoons B + C$, can be described using statistical thermodynamics and related via the partition functions of the species present:

$$\frac{N_B N_C}{N_A} = \frac{Z_B^0 Z_C^0}{Z_A^0} \quad (8)$$

where N is the number the each specific species present and Z^0 is the total partition function for each of those species [23]. Equation 8 can be reduced further to eliminate the translational partition functions and incorporate the number densities (n_X) of each species present in a plasma [23].

$$\frac{n_B n_C}{n_A} = \left(\frac{2\pi\mu kT}{h^2} \right)^{3/2} \frac{Z_B Z_C}{Z_A} e^{(-\Delta E/kT)} \quad (9)$$

In equation 9, μ is the reduced mass (calculated $\mu = M_B M_C / M_A$), k is the Boltzmann constant, h is Planck's constant, ΔE is the energy of the reaction, and Z is the internal partition function of

each species [23]. From this equation, Saha derived the Saha equation for ionization equilibrium.

Saha Equation for Singly Charged Ions

The Saha equation can be used to determine the degree of ionization for any species present in the plasma at a specific temperature. As mentioned previously, the most common or most abundant ions formed in an ICP are singly charged ions. For the reaction between singly charged ions and their corresponding neutral atoms, the Saha equation is as follows:



$$K_{ion}(T_{ion}) = \left(\frac{n_{M^+} n_e}{n_M} \right) = 2 \left(\frac{2\pi m_e k T_{ion}}{h^2} \right)^{3/2} \left(\frac{Z_{M^+}}{Z_M} \right) e^{(-IE(M)/kT_{ion})} \quad (11)$$

where n_{M^+} and n_M are the densities (cm^{-3}) of ions and atoms, respectively, m_e is the mass of an electron, Z_{M^+} and Z_M are the partition functions of the ion and atom, respectively, $IE(M)$ is the ionization energy (eV) for element M, T_{ion} is the ionization temperature (K) at this position within the plasma [23], and K_{ion} is the corresponding ionization constant (cm^{-3}). Equation 11 neglects the depression of ionization energy [23].

This version of the Saha equation can further be reduced to eliminate constants, resulting in the equations implemented by Niu and Houk [2].

$$\alpha_{M^+} = \frac{n_{M^+}}{n_M + n_{M^+}} \quad (12)$$

$$K_{ion,M} = \frac{(\alpha_{M^+})(n_e)}{(1 - \alpha_{M^+})} \quad (13)$$

$$\log(K_{ion,M}) = 1.5 \log(T_{ion}) - \frac{5040 (IE(M))}{T_{ion}} + \log\left(\frac{Z_{M^+}}{Z_M}\right) + 15.684 \quad (14)$$

In equation 14, T_{ion} refers to the ionization temperature at which the ionization constant ($K_{ion,M}$) is measured to be a particular value [2].

Saha Equation for Doubly Charged Ions

A similar relationship to that discussed for singly charged ion formation can be derived for doubly charged ion formation in an ICP:



$$K'_{ion,M} = \frac{(n_{M^{2+}})(n_e)}{(n_{M^+})} \quad (16)$$

$$\log(K'_{ion,M}) = 1.5 \log(T_{ion}) - \frac{5040 (IE(M^+))}{T_{ion}} + \log\left(\frac{Z_{M^{2+}}}{Z_{M^+}}\right) + 15.684 \quad (17)$$

Here $IE(M^+)$ is the second ionization energy of M (eV), $Z_{M^{2+}}$ is the electronic partition function of M^{2+} , and $n_{M^{2+}}$ is the density of M^{2+} in the plasma (cm^{-3}). Most elements have a very high second ionization energy, so M^{2+} ions are not highly abundant within the plasma, very few elements higher than 2%.

Some of the values for α_{M^+} (%) displayed in Houk's original ionization efficiency table included the density of doubly charged ions in the plasma [14]:

$$\alpha_{M^+} = \frac{n_{M^+}}{n_M + n_{M^+} + n_{M^{2+}}} \quad (18)$$

The updated ionization efficiency tables, discussed below, includes $n_{M^{2+}}$ as well.

Ionization of Metal Oxide Molecules

Metal oxide ions are common in ICP-MS. Similar to the ionization of atoms and singly charged ions, it is assumed that metal oxide molecules are ionized based on their ionization energy ($IE(MO)$) and T_{ion} as well.



$$\alpha_{MO^+} = \frac{n_{MO^+}}{n_{MO} + n_{MO^+}} \quad (20)$$

$$K_{ion,M} = \frac{(\alpha_{MO^+})(n_e)}{(1 - \alpha_{MO^+})} \quad (21)$$

$$\begin{aligned} \log(K_{ion,MO}) = & 1.5 \log(T_{ion}) - \frac{5040(IE(MO))}{T_{ion}} - \log\left(1 - 10^{\frac{-0.625\omega_{MO^+}}{T_{ion}}}\right) \\ & - \log\left(\frac{B_{MO^+}}{g_{MO^+}}\right) + \log\left(1 - 10^{\frac{-0.625\omega_{MO}}{T_{ion}}}\right) + \log\left(\frac{B_{MO}}{g_{MO}}\right) + 15.684 \end{aligned} \quad (22)$$

The partition functions of molecules are much more complex than those of neutral atoms and atomic ions. The overall partition function of a molecule is the product of the electronic, translational, vibrational, and rotational partition functions. In the equation above (Equation 22), ω is the vibrational constant (cm^{-1}), B is the rotational constant (cm^{-1}), and g is the statistical weight of the ground electronic state of either MO^+ or MO . Equation 22 is a simplified equation; therefore, the translational partition function is already accounted for. The reduced versions of the electronic, vibrational, and rotational partitions functions are further discussed in reference [22].

Dissociation of Metal Oxide Ions

The precursor to the Saha equation (Equation 8) can be used to further derive an equation to calculate the dissociation of polyatomic oxide ions in the plasma [22]. Because MO^+ ions are formed, they are, in turn, dissociated to an extent to produce M^+ ions. MO^+ ion dissociation is also at an equilibrium based on temperature, but as the temperature of the plasma is increased,

the oxide ions are dissociated to a greater extent. The degree of MO^+ dissociation is dependent on T_{gas} rather than T_{ion} . T_{gas} , as mentioned previously, is often lower than T_{ion} .



$$K_d = \frac{n_{M^+}n_O}{n_{MO^+}} \quad (24)$$

$$\begin{aligned} \log K_d(MO^+) = & 0.5 \log(T_{gas}) - \frac{5040 (D_0)}{T_{gas}} + \log\left(\frac{M_{M^+}M_O}{M_{MO^+}}\right) + \log(z_{M^+}z_O) \\ & + \log\left(1 - 10^{\frac{-0.625\omega}{T_{gas}}}\right) + \log\left(\frac{B}{g}\right) + 20.432 \end{aligned} \quad (25)$$

In Equation 25, K_d is the dissociation equilibrium constant and D_0 is the dissociation energy (eV) of MO^+ . Like the ionization of MO , the partition function of MO^+ is defined by the electronic, vibrational, and rotational constants. Equation 25 is described in more detail by Houk and Praphairaksit [22]. Note that Equation 25 is only valid if M is not O ; the numerical constant of 20.432 is only valid for heteronuclear diatomic molecules [24].

Updated Ionization Efficiency Tables for Singly Charged Ions

The efficiencies of ionization approximated using the Saha equation for singly charged ions for most elements on the periodic table are shown in Figure 3 for temperatures of 6500 K and 7000 K. The electron density for the calculations displayed was assumed to be that used by Houk of $1 \times 10^{15} \text{ cm}^{-3}$. With only a small 500 K temperature shift, large differences in ionization can be seen. Many of the elements with an ionization efficiency of less than 30% at 6500 K, are ionized almost twice as extensively at 7000 K.

In comparison to the original values published by Houk (Figure 2), the ionization efficiency values at 6500K and 7000K are lower; even for metals like Ni, Cu, Zn, etc. Values for

elements that were not published by Houk are also shown in the new figure. These values were not originally published due to a lack of available partition functions. Polynomial coefficients for the electronic partition functions used for ionization calculations were published by de Galan et al. for temperatures ranging from 1500 K to 7000 K and Tamaki and Kuroda for temperatures ranging from 7000 K to 12000 K [25, 26]. The partition function coefficients for the rare earth elements were published by Faggetter et al. for temperatures ranging from 1500 K to 8000 K as well [27]. These published values were used to calculate the ionization efficiencies for all elements for which they were available. For those elements that electronic partition function polynomial coefficients were not available, a generalized partition function was calculated based on the population of the sublevels of the ground state at temperatures from 4000 K to 7500 K using a 3rd order polynomial fit [28, 29, 30].

Figure 4 shows a plot of the degree of ionization versus ionization energy for singly charged ions. The individual points include the partition functions for the corresponding element. This plot shows that elements with a required ionization energy up to 6 eV, are ionized nearly 100% at 6500 K (Figure 4A). At 7000 K, elements with ionization energy of 7.5 eV or less are nearly 100% ionized (Figure 4B).

Ionization Efficiency Tables for Doubly Charged Ion Formation

Doubly charged ions are also formed in the ICP, as shown by Equation 17. As T_{ion} increases, the population of doubly charged ions increases as well. The degree of doubly charged ion formation is shown for each element of the periodic table in Figure 5 for temperatures of 6500 K and 7000 K. Again, the electron density was assumed to be $1 \times 10^{15} \text{ cm}^{-3}$.

Only a select number of elements, mostly alkaline earth and rare earth elements, form appreciable amounts ($M^{2+}/M^+ \geq 0.01\%$) of doubly charged ions at 6500 K. However, a small increase in temperature of only 500 K increases M^{2+} abundance, as much as 4 to 5 fold for those elements, like Ra, Ce, and Pr, that form a significant amount of doubly charged ions.

In comparison to the calculated values for the degree of doubly charged ion formation published by Houk, doubly charged ions are much less abundant at temperatures of 6500 K and 7000 K than at 7500 K. Houk's original ionization efficiency table (Figure 2) only showed the degree of doubly charged ion formation for a select few elements. At the time, very few partition function coefficients were available for doubly charged ions. More recently, Pupyshev and Semenova published electronic partition function coefficients for doubly charged atomic ions for a temperature range from 2500 K to 12000 K for many atomic ions [21]. These electronic partition function coefficients, as well as calculated electronic partition function coefficients from ground state energy sublevels, were used to complete the calculations for Figure 5.

Pupyshev and Semenova also calculated the degree of doubly charged ion formation for various elements on the periodic table at $T_{\text{ion}} = 7500$ K and $n_e = 1 \times 10^{15} \text{ cm}^{-3}$ [21]. In comparison to their calculated values, our updated calculations (Figure 5) again show that doubly charged ions are less abundant at temperatures of 6500 K and 7000 K. The updated calculations are in agreement with Pupyshev and Semenova in showing that alkaline earth elements, all rare earth elements, and light actinides have the highest potential of forming M^{2+} ions in ICP-MS [21].

Metal Oxide Ionization and Dissociation

For MO^+ ions, calculations of both the degree of ionization and the degree of dissociation, are more difficult. For the degree of ionization, vibrational, rotational, and electronic partition functions are required for both MO neutral molecules and MO^+ ions. Because of this, values could not be calculated for the degree of MO ionization or MO^+ dissociation for all elements on the periodic table, like the calculations for atomic ions discussed previously. Table 1 shows the fundamental constants and the calculated degrees of ionization and dissociation for a select few MO molecules at T_{ion} of 6500 K and T_{gas} of 6000 K, and T_{ion} of 7000 K and T_{gas} of 6000 K [31, 32, 33, 34, 35, 36, 37, 38, 39, 40].

In terms of MO ionization, the calculations in Table 1 show that MO molecules with $\text{IE}(\text{MO})$ less than or equal to 5.5 eV are nearly 100% ionized. This is comparable to the IE values for atoms that are shown to be nearly 100% ionized in Figure 4. To determine if the partition functions are absolutely necessary in the calculations of MO ionization efficiency, $\alpha(\text{MO}^+)$ percentage values were calculated considering the partition functions as negligible. The values for these calculated ionization efficiencies are shown in parenthesis in Table 1. For MO molecules with $\text{IE}(\text{MO})$ less than or equal to 5.5 eV, the partition functions make very little difference in the degree of ionization, neutral MO is ionized to MO^+ almost completely. However, MO molecules with $\text{IE}(\text{MO})$ greater than 5.5 eV show a much larger difference in the degree of ionization when the partition functions are neglected. Therefore, the partition functions are necessary for accurate calculation of the degree of MO ionization for those MO molecules with $\text{IE}(\text{MO}) \geq 5.5$ eV.

It is possible that some MO^+ ions form doubly charged metal oxide ions (MO^{2+}) in the plasma dependent on the second ionization energy of MO. In the calculations discussed in this

paper, MO^{2+} is considered negligible. Hattendorf and Günther found that MO^{2+} ions are present in several types of ICP-MS instruments at signal ratios of 10^{-4} relative to M^+ ions and 10^{-2} relative to M^{2+} ions for Th [41]. Hattendorf and Günther also propose that the extent of MO^{2+} ion formation is dependent on the degree of M^{2+} ion formation of an element and its M-O bond energy, both of which are generally high for the rare earth elements [41].

In terms of MO^+ dissociation, the ions with lower dissociation energies, including YO^+ with D_0 equal to 7.24 eV, are nearly 100% dissociated at a gas kinetic temperature of 6000 K with an oxygen density (n_{O}) of $\sim 7 \times 10^{16} \text{ cm}^{-3}$. As T_{gas} increases, this maximum value of dissociation energy at which the degree of dissociation is nearly 100% will increase as well, similar to the trend shown in Figure 4. This, in turn, shows that hotter gas kinetic temperatures reduce the amount of MO^+ ion present in the plasma as polyatomic interference ions.

Conclusion

This work shows that small changes in plasma temperature can make a large difference in the efficiency of ionization for some elements in an ICP. Most often, it is not necessary to account for ionization efficiency in everyday ICP analyses. In those scenarios where it is necessary to account for the ionization of a specific analyte, knowledge of the plasma temperature is important to account for the correct degree of ionization.

In terms of M^{2+} ion formation and MO^+ dissociations, it is important to keep the plasma parameters in mind for a plasma temperature to produce a minimum amount of MO^+ and M^{2+} ions. These ions can cause interferences at the same mass-to-charge (m/z) values as analyte ions due to the MO^+ and M^{2+} ions having the same nominal mass. Most ICP-MS instrumentation is

optimized for maximum M^+ analyte ion signals and acceptable metal oxide ion (MO^+/M^+) and doubly charged ion (M^{2+}/M^+) signal ratios.

Future work on cool plasma conditions would provide insight into ionization at colder plasma temperatures and lower electron densities. Cool plasmas are often implemented to measure low levels of elements with low ionization energies at m/z values that often exhibit high levels of interference ions, i.e. K, Ca, and Fe [42].

References

- [1] K. E. Jarvis, A. L. Gray, R. S. Houk, Handbook of Inductively Coupled Plasma Mass Spectrometry, New York: Blackie & Son Ltd, 1992.
- [2] H. Niu, R.S. Houk, Fundamental aspects of ion extraction in inductively coupled plasma mass spectrometry *Spectrochimica Acta Part B* (1996) 779-815.
- [3] S. R. Koirtiyohann, J. S. Jones, D. A. Yates, Nomenclature System for the Low-Power Argon Inductively Coupled Plasma, *Anal. Chem.* 52 (1980) 1966-1968.
- [4] S. D. Tanner, Plasma Temperature from Ion Kinetic Energies and Implications for the Source of Diatomic Oxide Ions in Inductively Coupled Plasma Mass Spectrometry, *J. Anal. At. Spec.* 8 (1993) 891-897.
- [5] D. S. Hanselman, N. N. Sesi, M. Huang, G. M. Hieftje, The Effect of Sample Matrix on Electron Density, Electron Temperature and Gas Temperature in the Argon Inductively Coupled Plasma Examined by Thomson and Rayleigh Scattering, *Spectrochim. Acta* 49B (1994) 495-526.
- [6] T. Hasegawa, H. Haraguchi, A. Montaser, D. W. Golightly, Fundamental Properties of Inductively Coupled Plasmas, in: A. Montaser, D.W. Golightly, *Inductively Coupled Plasmas in Analytical Atomic Spectroscopy*, New York, VCH, 1987, pp. 267-321.
- [7] R. S. Houk, Y. Zhai, Comparison of Mass Spectrometric and Optical Measurements of Temperature and Electron Density in the Inductively Coupled Plasma During mass Spectrometric Sampling, *Spectrochim. Acta Part B* 56 (2001) 1055-1067.
- [8] R. S. Houk, H. J. Svec, V. A. Fassel, Mass Spectrometric Evidence for Spurrathermal Ionization in an Inductively Coupled Argon Plasma, *Appl.Spectrosc.* 35 (1981) 380-384.

- [9] H. Niu, R. S. Houk, Langmuir probe measurements of the ion extraction process in inductively coupled plasma mass spectrometry - I. Spatially resolved determination of electron density and electron temperature, *Spectrochim. Acta* 49B (1994) 1283-1303.
- [10] S. A. Lehn, K. A. Warner, M. Huang, G. M. Heiftje, Effect of an inductively coupled plasma mass spectrometry sampler interface on electron temperature, electron number density, and gas-kinetic temperature and analyte emission intensity upstream in the plasma, *Spectrochim. Acta Part B* 57 (2002) 1739-1751.
- [11] G. Gamez, S. A. Lehn, M. Huang, G. M. Heiftje, Effect of mass spectrometric sampling interface on the fundamental parameters of an inductively coupled plasma as a function of its operating conditions: Part II. Central-gas flow rate and sampling depth, *Spectrochim. Acta Part B* 62 (2007) 370-377.
- [12] J. S. Crain, F. G. Smith, R. S. Houk, Mass spectrometric measurement of ionization temperature in an inductively coupled plasma, *Spectrochim. Acta* 45B (1990) 249-259.
- [13] D. A. Wilson, G. H. Vickers, G. M. Heiftje, Ionization Temperature in the ICP determined by MS, *Appl. Spectrosc.* 41 (1987) 875-880.
- [14] R. S. Houk, Mass Spectrometry of Inductively Coupled Plasmas, *Anal. Chem.* 58 (1986) 97A-105A.
- [15] C. Mariet, F. Carrot, M. Moskura, Effects of sample matrix on radial and axial profiles of ion abundance in inductively coupled plasma mass spectrometry, *Am. J. Anal. Chem.* 2 (2011) 739-751.
- [16] N. Shirai, M. Humayun, Mass independent bias in W isotopes in MC-ICP-MS instruments, *J. Anal. At. Spectrom.* 26 (2011) 1414-1420.
- [17] I. Rodushkin, M. D. Axelsson, D. Malinovsky, D. C. Baxter, Analyte- and matrix-dependent elemental response variations in laser ablation inductively coupled plasma mass spectrometry, *J. Anal. At. Spectrom.* 17 (2002) 1231-1239.
- [18] B. P. Jackson, W. P. Miller, Arsenic and selenium speciation in coal fly ash extracts by ion chromatography-inductively coupled plasma mass spectrometry, *J. Anal. At. Spectrom.* 13 (1998) 1107-1112.
- [19] M. Patriarca, N. A. Kratochwil, P. J. Sadler, Simultaneous determination of Pt and I by ICP-MS for studies of the mechanism of reaction of diiodoplatinum anticancer complexes, *J. Anal. At. Spectrom.* 14 (1999) 633-637.
- [20] Y. Manonnen and D. Beauchemin, Investigation of a Measure of Robustness in Inductively Coupled Plasma Mass Spectrometry, *Spectrochim. Acta Part B*, 103-104 (2014) 57-62.

- [21] A. A. Pupyshev, E. V. Semenova, Formation of doubly charged atomic ions in the inductively coupled plasma, *Spectrochim. Acta Part B* 56 (2001) 2397-2418.
- [22] R. S. Houk, N. Praphairaksit, Dissociation of polyatomic ions in the inductively coupled plasma, *Spectrochim. Acta Part B* 56 (2001) 1069-1096.
- [23] A. Thorne, U. Litzen, S. Johansson, *Spectrophysics: Principles and Applications*, New York: Springer, 1999, pp. 209-229, 231-254.
- [24] R. S. Houk, Erratum to "Dissociation of polyatomic ions in inductively coupled plasma - mass spectrometry" [*Spectrochimica Acta Part B* 56 (2001) 1096 - 1096], *Spectrochim. Acta Part B* 61 (2006) 235-236.
- [25] L. De Galan, R. Smith, J. D. Winefordner, The electronic partition functions of atoms and ions between 1500K and 7000K, *Spectrochim. Acta* 23B (1968) 521-525.
- [26] S. Tamaki, T. Kuroda, The electronic partition functions of atoms and ions between 7000 and 12000 K, *Spectrochim. Acta* 42B (1987) 1105-1111.
- [27] B. Faggetter, G. Heiz, M. W. Blades, The electronic partition function functions of lanthanide atoms and ions between 1500 and 8000 K, *Spectrochim. Acta* 42B (1987) 1235-1236.
- [28] C. E. Moore, *Atomic Energy Levels, Volume 1*, Washington, D.C.: National Bureau of Standards 467, 1949.
- [29] C. E. Moore, *Atomic energy Levels, Volume 2*, Washington, D.C.: National Bureau of Standards, 1952.
- [30] C. E. Moore, *Atomic Energy Levels, Volume 3*, Washington, D.C.: National Bureau of Standards, 1958.
- [31] N. S. Nonose, N. Matsuda, N. Fudagawa, M. Kubota, Some characteristics of polyatomic ion spectra in inductively coupled plasma mass spectrometry, *Spectrochim. Acta* 49B (1994) 955-974.
- [32] K. P. Huber, G. Herzberg, *Molecular Spectra and Molecular Structure*, New York: Van Nostrand Reinhold Company, 1979.
- [33] J. Husband, F. Aguirre, P. Ferguson, R. B. Metz, Vibrationally resolved photofragment spectroscopy of FeO^+ , *J. Chem. Phys.* 111 (1999) 1433-1437.

- [34] E. R. Fisher, J. L. Elkind, D. E. Clemmer, R. Georgiadis, S. K. Loh, N. Aristov, L. S. Sunderlin, P. B. Armentrout, Reactions of fourth-period metal ions (Ca^+ - Zn^+) with O_2 : metal-oxide ion bond energies, *J. Chem. Phys.* 93 (1990) 2676-2691.
- [35] C. Linton, B. Simard, H. P. Loock, S. Wallin, G. K. Rothschof, R. F. Gunion, M. D. Morse, P. B. Armentrout, Rydberg and pulsed field ionization-zero electron kinetic energy spectra of YO, *J. Chem. Phys.* 111 (1999) 5017-5026.
- [36] M. R. Sievers, P. B. Armentrout, Activation of carbon dioxide: gas-phase reactions of Y^+ , YO^+ , and YO_2^+ with CO and CO_2 , *Inorg. Chem.* 38 (1999) 397-402.
- [37] M. R. Sievers, Y.-M. Chen, P. B. Armentrout, Metal oxide and carbide thermochemistry of Y^+ , Zr^+ , Nb^+ , and Mo^+ , *J. Chem. Phys.* 105 (1996) 6322-6333.
- [38] C. J. Thompson, K. L. Stringer, M. McWilliams, R. B. Metz, Electronic spectroscopy of predissociative states of platinum oxide cation, *Chem. Phys. Lett.* 376 (2003) 588-594.
- [39] M. Bronstrup, D. Schroder, I. Kretzschmar, H. Schwarz, J. N. Harvey, Platinum dioxide cation: easy to generate experimentally but difficult to describe theoretically, *J. Am. Chem. Soc.* 123 (2001) 142-147.
- [40] X.-G. Zhang, P. B. Armentrout, Activation of O_2 and CO_2 by PtO^+ : the thermochemistry of PtO_2^+ , *J. Phys. Chem. A* 107 (2003) 8915-8922.
- [41] B. Hattendorf, D. Gunther, Experimental evidence for the formation of doubly charged oxide and hydroxide ions in inductively coupled plasma mass spectrometry, *Fresen. J. Anal. Chem.* 370 (2001) 483-487.
- [42] S. D. Tanner, Characterization of ionization and matrix suppression in inductively coupled 'cold' plasma mass spectrometry, *J. Anal. At. Spectrom.* 10 (1995) 905-921.

Table 1: Calculated degree (%) of MO ionization and MO⁺ dissociation at T_{ion} = 6500 K and T_{gas} = 6000K, and T_{ion}=7000K and T_{gas} = 6000K with n_O = 7×10¹⁶ cm⁻³. The corresponding constants for the partitions functions ω, B, and g, are listed as well. The necessity of these constants are determined my comparing calculations considering the partition functions as negligible.

MO	IE(MO) (eV)	D ₀ (MO ⁺) (eV)		ω (cm ⁻¹)	B (cm ⁻¹)	g		α (%) T _{ion} = 6500 K (Z neg.)	α (%) T _{ion} = 7000 K (Z neg.)	Reference
NO	9.26	10.85	NO	1904.2	1.67195	2	NO ⁺ /(NO+NO ⁺)	5.5 (14)	18 (38)	[31, 32]
			NO ⁺	2376.42	1.99727	1	NO ⁺ /N ⁺	>100		
FeO	8	3.53	FeO	965	0.5127	5	FeO ⁺ /(FeO+FeO ⁺)	67 (61)	86 (83)	[32, 33, 34]
			FeO ⁺	915.2	0.5012	6	FeO ⁺ /Fe ⁺	3.7E-3		
YO	5.5	7.24	YO	861	0.3881	2	YO ⁺ /(YO+YO ⁺)	98 (99)	99 (100)	[32, 35, 36, 37]
			YO ⁺	1076	0.4078	1	YO ⁺ /Y ⁺	2.1		
PtO	10.1	3.26	PtO	851.11	0.38224	1	PtO ⁺ /(PtO+PtO ⁺)	16 (3.6)	44 (13)	[32, 38, 39, 40]
			PtO ⁺	799	0.306	4	PtO ⁺ /Pt ⁺	9.7E-3		

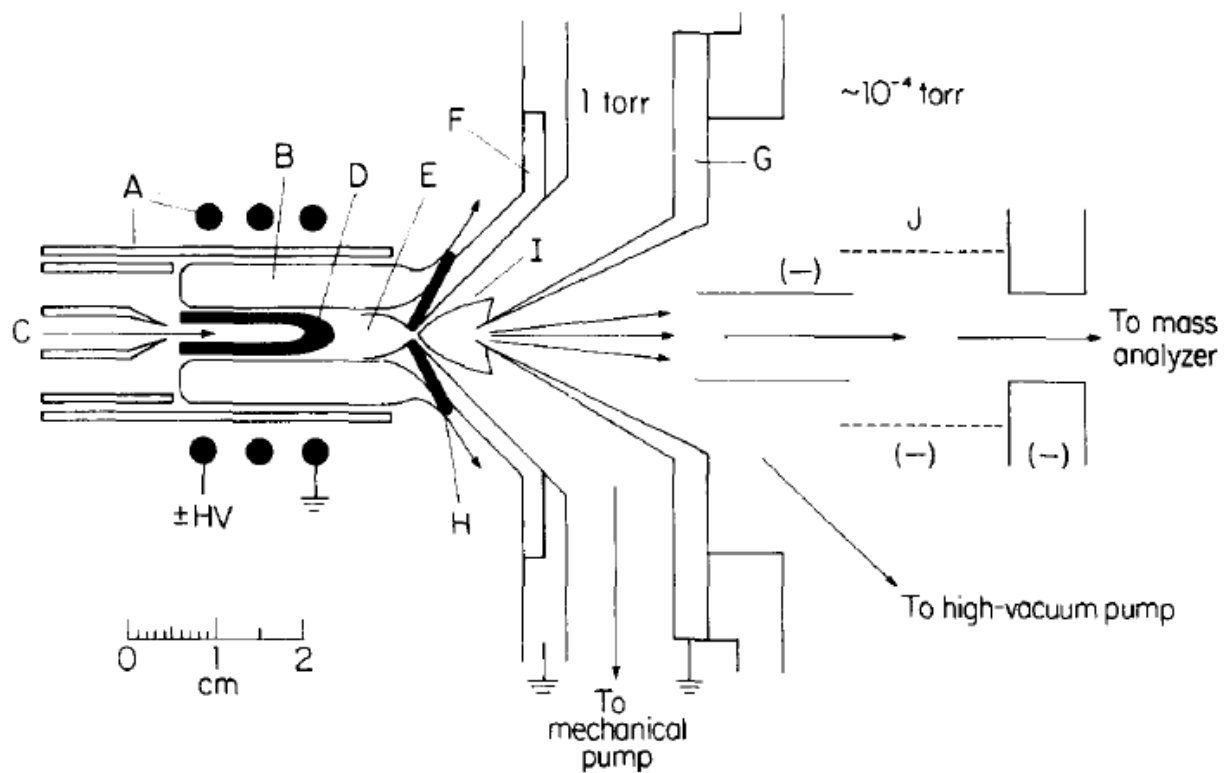


Figure 1: A schematic of the plasma torch, plasma, and ion extraction process. A – Plasma Torch and RF Load Coil, B – Outer Gas Region, C – Central Plasma Gas Flow, D – IRZ, E – NAZ, F – Sampler Cone, G – Skimmer Cone, H – Boundary Layer from Gases, I – Supersonic Expansion, J – Ion Lenses. Reproduced from reference [2] with permission.

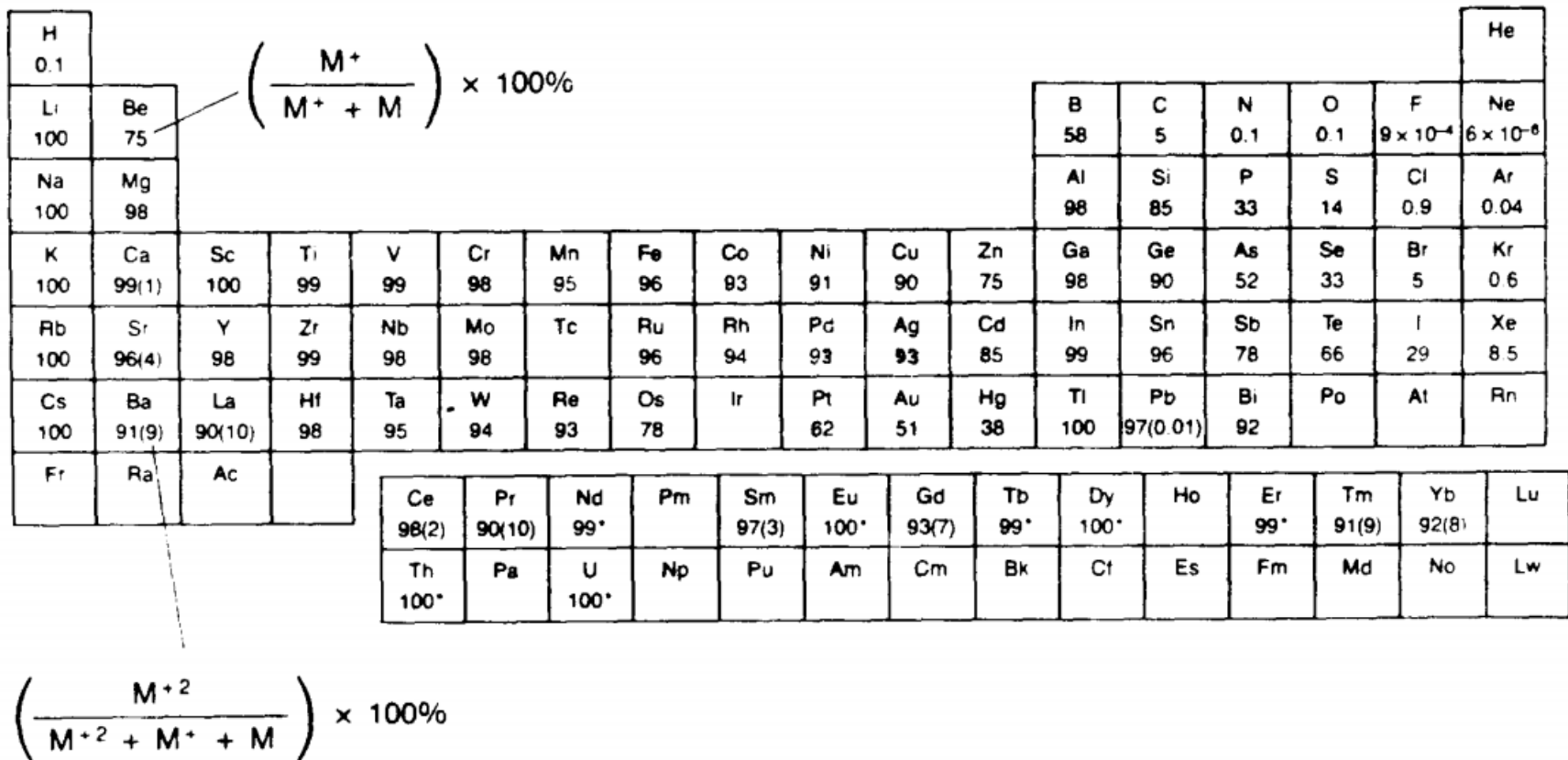


Figure 2: The calculated degree of ionization in percent for each element in a normal “hot” plasma with $T_{ion} = 7500$ K and $n_e = 1 \times 10^{15} \text{ cm}^{-3}$. Reproduced from references [2] and [14] with permission.

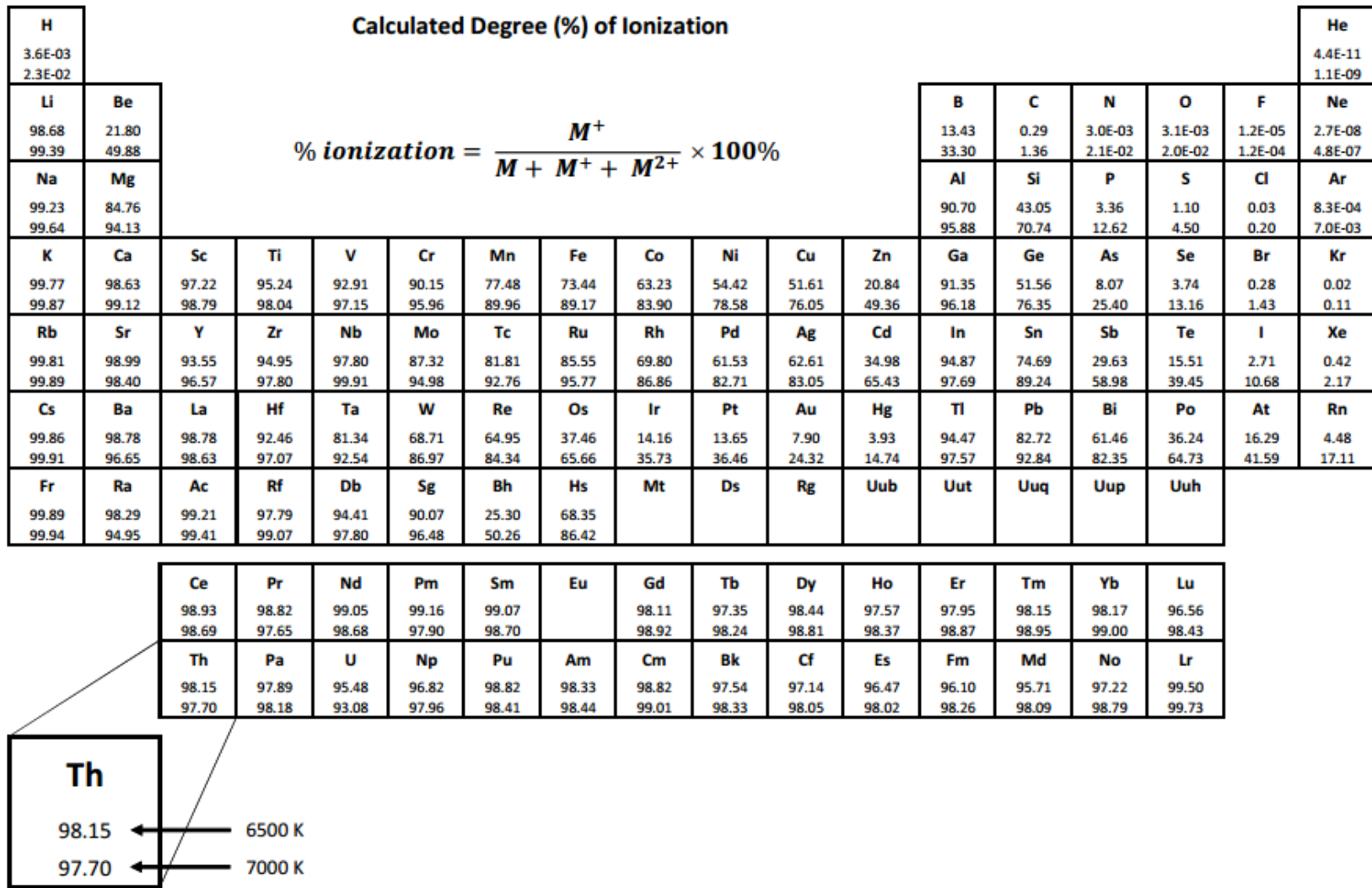


Figure 3: The calculated degree of ionization in percent for each element in a normal “hot” plasma with conditions conducive to an ionization temperature of 6500 K or 7000 K with an electron density of $1 \times 10^{15} \text{ cm}^{-3}$.

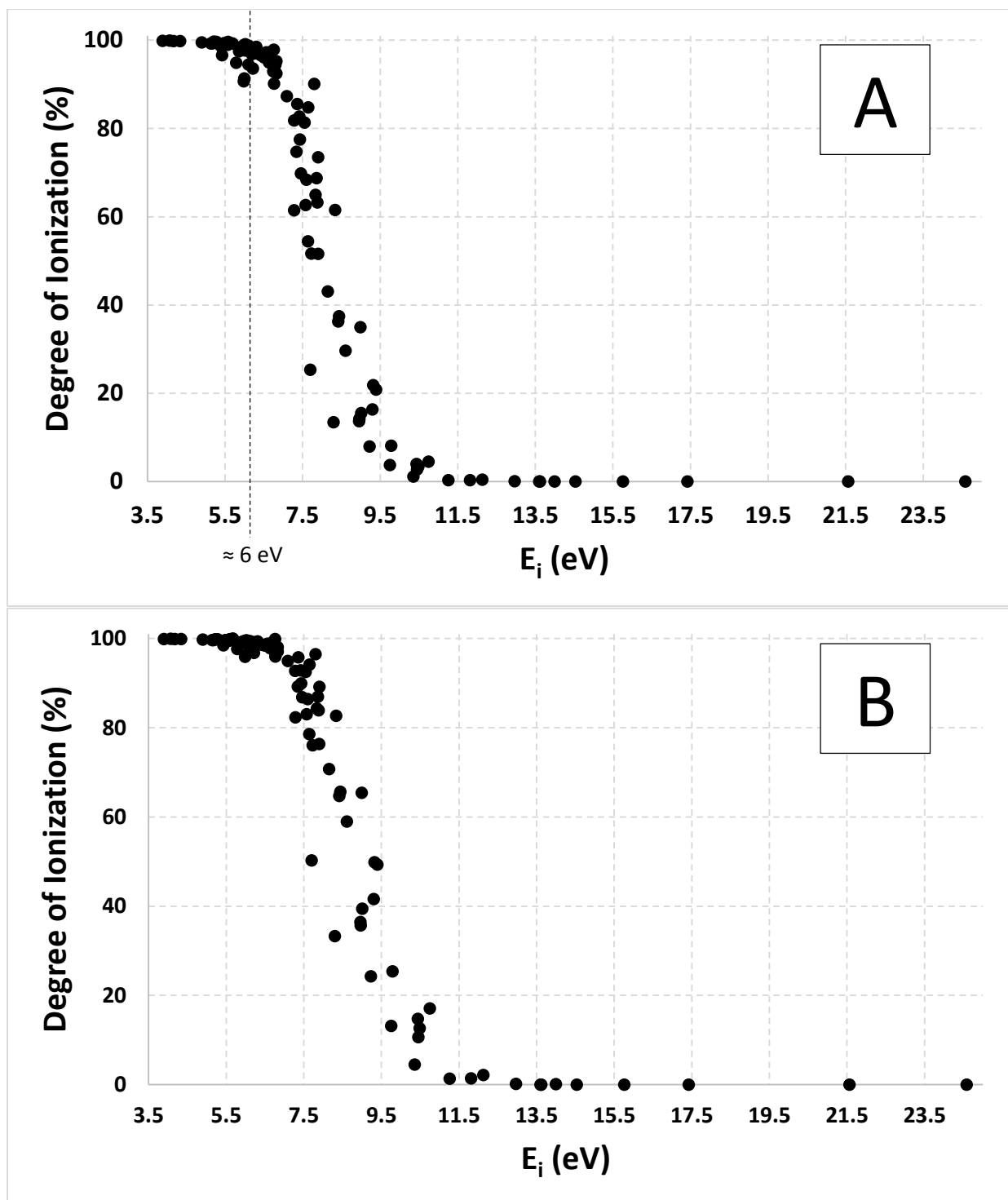


Figure 4: A plot of the degree of ionization with increasing ionization energy for singly charged ion formation at (A) 6500 K and (B) 7000K. As the temperature of the plasma increases, the number of elements ionized near 100% are increased significantly.

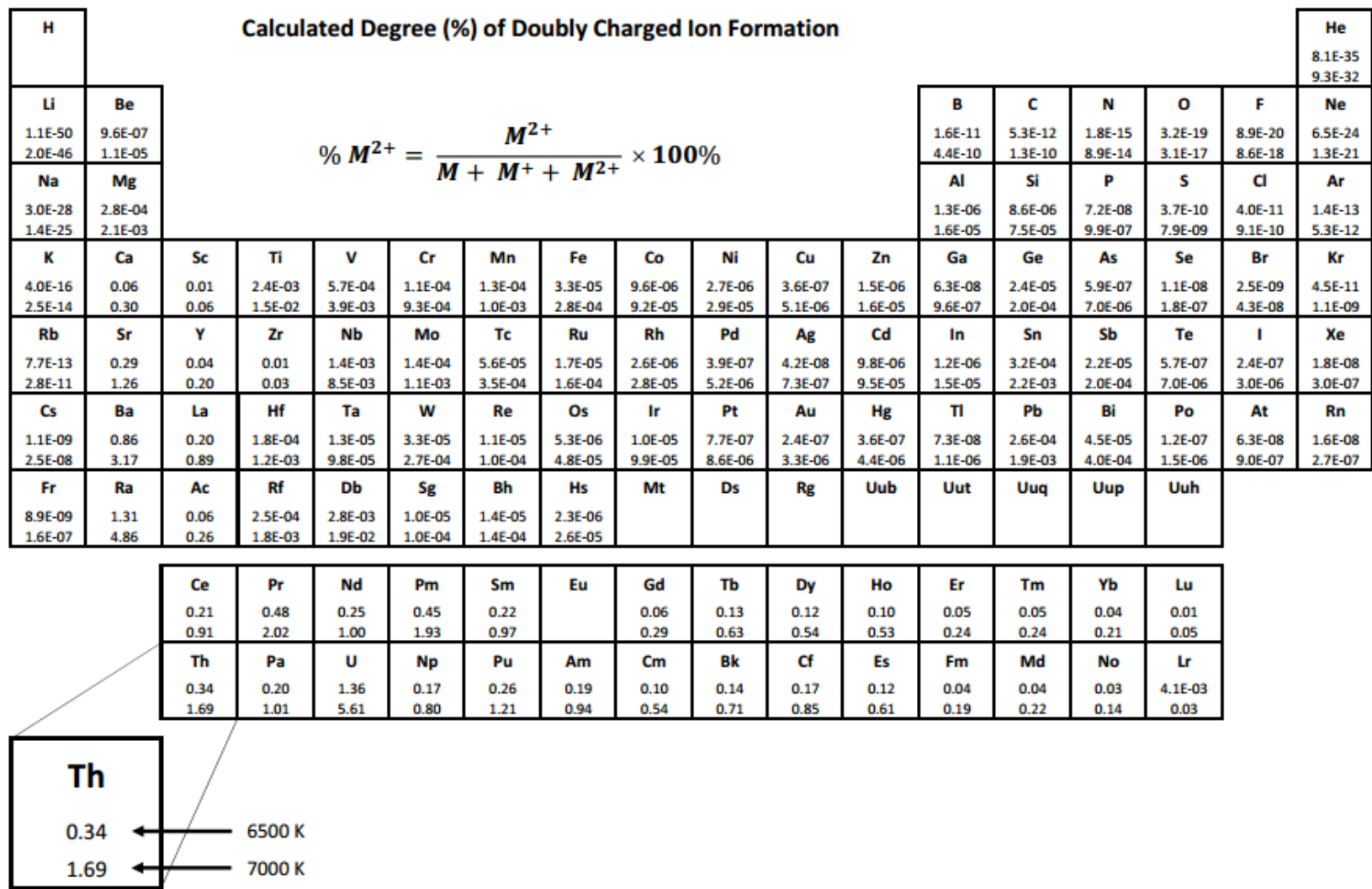


Figure 5: The calculated degree of doubly charged ion formation in percent for each element in a normal “hot” plasma with conditions conducive to an ionization temperature of 6500 K.

**CHAPTER 3. FUNDAMENTALS OF THE COLLISION REACTION INTERFACE
IN INDUCTIVELY COUPLED PLASMA MASS SPECTROMETRY:
USING ION KINETIC ENERGIES TO
CHARACTERIZE THE CRI COLLISION REGION**

J. L. Jacobs and R. S. Houk

Abstract

The collision reaction interface (CRI) removes polyatomic ions in inductively coupled plasma mass spectrometry (ICP-MS) by introducing a collision gas directly into the plasma expansion as ions are extracted into the mass spectrometer. Many collisions and reactions occur in a relatively short region, much shorter than with other instruments that use multipole collision cells. In this paper, experiments are first described for the determination of the collision cross sections of singly charged cations employing the use of a collision cell. Based on those determined cross sections, general characteristics of the collision region in CRI are determined and discussed.

Introduction

The introduction of a collision gas in ICP-MS for kinetic energy discrimination (KED) of polyatomic ions has been implemented for decades. Douglas and French first noted collisional dampening of ion energies in the early 1990's while studying collisional focusing of protein ions in quadrupoles [1]. This observation was first used to remove polyatomic ions in ICP-MS by Yamada, Takahashi, and Sakata [2]. Since then, KED has been used to remove interferences for

accurate quantification of many elements, including titanium, chromium, arsenic, potassium, and iron, which can often be difficult to measure using low resolution ICP-MS instrumentation [3, 4, 5, 6, 7]. A single collision gas, usually He, serves to remove many different polyatomic ions by this method.

The collision cell, which is most commonly employed to implement KED, was first applied in ICP-MS for the removal of polyatomic ion interferences by collision induced dissociation or chemical reactions [8, 9]. A collision cell is a set of quadrupole, hexapole, or octopole rods, generally in an enclosed cylinder, located between the skimmer and the mass analyzer. Within the enclosed region of the collision cell, a desired collision gas can be applied to induce collisions between the generated ions from the plasma and gas phase atoms or molecules of the collision gas. Either chemical reactions result in the formation of new ions or atoms, or the kinetic energies of the unwanted polyatomic ions are reduced more than those of the desired atomic analyte ions at the same nominal m/z value.

More recently (within the past 10 years), the collision reaction interface (CRI) was introduced for these purposes. The main function of the CRI is to induce collisions between the plasma generated ions and gas phase atoms or molecules, like the collision cell. However, the CRI introduces the collision gas directly into the beam extracted from the plasma, via either a two-edged sampler or skimmer cone. Most commonly, a conventional sampler is used, and helium and/or hydrogen are added through the CRI skimmer. The main benefit of introducing a collision or reaction gas directly into the plasma expansion is many collisions or reactions occur in a relatively small, dense area prior to extraction into the mass spectrometer [10]. This small collision region ultimately requires very little time to reach a steady-state density of the collision gas, so the collision gas can be changed or removed very rapidly, i.e., in only a few seconds.

The characteristics of the collision region within collision cells have been studied quite extensively [3]. In a collision cell, the applied voltages on the quadrupole rods guide the ions toward the detector. The gas density within the collision cell can be determined based on the incoming gas pressure or flow rate, the internal flow regime, and the conductances of the collision cell openings [11]. The dimensions of the collision cell can be determined by physical measurements of the collision cell components.

Knowing the dynamics within and dimensions of a collision cell, it is possible to determine approximately how many collisions are undergone by an ion as it travels through the collision region. This number, N , is directly related to the collision cross section of that ion (Ω , cm^2), the gas density within the collision cell (n , cm^{-3}), and the length of the collision region (L , cm) [12].

$$N = L \cdot n \cdot \Omega \quad (1)$$

In this work, we assume L is the length of collision cell, i.e., the ions are not deflected radially much by the RF voltage on the collision cell rods.

Unfortunately, the collision cross sections of small monatomic ions have not been thoroughly studied; values for only a few elements are available in the literature [13, 14, 15]. We contend that the collision cross sections for atomic ions can be determined approximately based on the known characteristics of the collision cell and the degree of kinetic energy loss caused by kinetic energy discrimination, as demonstrated for protein ions by Covey and Douglas [12]. They determined that the collision cross section of an ion based on the loss of kinetic energy as the gas phase ion travels through a collision cell is directly related to the masses of the ions and neutral atoms or molecules involved in the collisions [12]. The ratio of energy remaining after one elastic collision is:

$$\frac{KE_1}{KE_{initial}} = \frac{(m_{coll\ gas})^2 + (m_{ion})^2}{(m_{coll\ gas} + m_{ion})^2} \quad (2)$$

where KE_1 is the measured kinetic energy after one collision, $KE_{initial}$ is the measured kinetic energy when no collisions occur, $m_{coll\ gas}$ is the mass of the collision gas and m_{ion} is the mass of the ion. This equation can be applied sequentially to determine the number of collisions (N) that one ion undergoes based on the kinetic energy remaining after N collisions (KE_N). After two collisions the fraction of kinetic energy remaining is $KE_2 = (KE_1/KE_{initial})^2$, etc. The value of N can be determined from

$$\left(\frac{KE_1}{KE_{initial}}\right)^N = \left(\frac{KE_N}{KE_{initial}}\right) \quad (3)$$

In this report, experiments are first described using these relationships to determine the collision cross sections of singly charged cations employing the use of a collision cell instrument, a Thermo X Series II with a hexapole collision cell. These collision cross sections are then used to characterize the collision region in a different instrument with a CRI, a Bruker Aurora Elite (now PlasmaQuant, Analytik Jena). It is known that atomic ions in electronically excited states can have very different cross sections from those in the ground state [16]. The present work assumes one of two situations: a) the abundances of ions in electronically excited states in the extracted plasma and beam are negligible [17], or b) if excited state ions are present, their populations are similar from the two instruments, since the plasma and ion extraction conditions are selected by the same criteria.

Experimental

Solutions and Materials

All solutions containing Y, Mo, and Ag were prepared by serial dilution of commercially available 1000 ppm single element Y, Mo, and Ag solutions (Spex CertiPrep, High Purity Standards, Plasmachem Associates Inc.) in clean plastic Nalgene bottles. All dilutions were completed with prepared 1% nitric acid (HNO₃). Prior to preparation, concentrated nitric acid (~70%, Fisher Scientific) was cleaned of elemental impurities by sub-boiling distillation in a Teflon still (Savillex). All water used had a resistivity of 18 MΩ cm (Barnsted Nanopure).

Industrial grade argon (99.995 % purity, Matheson) was used for plasma generation. Zero grade helium (99.999 % purity, Matheson) was used as a collision gas.

Determination of Ion Collision Cross-Sections Using Hexapole Collision Cell

The collision cross-sections for the ions of interest (⁸⁹Y⁺, ⁹⁵Mo⁺, ⁹⁸Mo⁺, ⁸⁹Y¹⁶O⁺, ¹⁰⁷Ag⁺ and ¹⁰⁹Ag⁺) were determined by measuring the change in kinetic energy due to collisions by making the quadrupole bias voltage more positive. The instrument used was a Thermo X Series II ICP-MS with a shielded load coil and a grounded shield. The signals for these ions were measured at quadrupole pole bias settings ranging from -7 V to +7 V using a quadrupole pole bias pattern of -7.0 V, -6.7 V, -6.3 V, -6.0 V, -5.7 V, etc. until all signals were completely lost (<1% of the maximum signal remained). A full range of pole bias versus ion signal measurements, also known as stopping curves, were taken at helium flow rates of 0, 0.5, 1, 2.5 and 5 mL/min. Prior to the measurements, the collision gas density was allowed to reach equilibrium within the collision cell. This equilibrium was determined by watching for

consistent ion signals at a quadrupole pole bias setting of -6 V. At least 30 minutes were allowed for this equilibration step.

The elemental standards were introduced into the plasma via a self-aspirating nebulizer (Elemental Scientific, Inc., 400 $\mu\text{L}/\text{min}$) and a cyclonic spray chamber at room temperature. To maintain similar initial pulse counting signal levels for each measured stopping curve, the elemental solution concentrations and counting detector voltage were adjusted for each helium flow rate. Besides the instrumental parameters previously mentioned, all other instrumental parameters were held constant (Table 1), particularly the ICP operating conditions and sampling position. These instrumental parameters were chosen to maximize instrument sensitivity while minimizing metal oxide ($\text{CeO}^+/\text{Ce}^+ \leq 2\%$) and doubly charged ($\text{Ba}^{2+}/\text{Ba}^+ \leq 3\%$) ion ratios. These signal ratios are common optimization values for various instruments. It is also our experience that reproducing operating conditions based on these measured ion signal ratios yields very consistent ionization temperatures (6500 to 7000 K) [18] and gas temperatures (5500 to 6000 K) [19, 20, 21] for various ICP-MS instruments, both quadrupoles and magnetic sectors.

Determination of CRI Dimensions and Conditions

The degree of kinetic energy loss caused by the helium CRI gas added to the skimmer was determined using stopping curves in a similar manner to the determination of the collision cross sections. These measurements were performed on a Bruker Aurora Elite ICP-MS. The signals for $^{89}\text{Y}^+$, $^{95}\text{Mo}^+$, $^{98}\text{Mo}^+$, $^{89}\text{Y}^{16}\text{O}^+$, $^{107}\text{Ag}^+$ and $^{109}\text{Ag}^+$ were measured at pole bias settings ranging from -6 V to +6 V at ~ 0.3 V intervals. A full range of stopping curve measurements were taken at CRI helium flow rates of 0, 30, 70, and 100 mL/min. The CRI required only a short time to reach equilibrium at each new gas flow rate and was ready for measurement within 60 seconds of setting the CRI gas flow, even going from a high CRI flow rate back to zero.

The elemental standards were introduced into the plasma via a peristaltically pumped nebulizer (Micro Mist) at an uptake rate of $\sim 220 \mu\text{L}/\text{min}$. The Scott type spray chamber was water cooled to $3 \text{ }^\circ\text{C}$. The instrument interface was equipped with grounded nickel cones, a non-CRI sampler (i.e., one with a single wall) and a double walled CRI skimmer. The concentrations of the elemental standards were increased as the helium flow rate was increased to compensate for signal loss caused by helium collisions. No attenuation coefficients were implemented during CRI mode. All other instrumental parameters were maintained constant for all helium CRI flow rates (Table 2). These instrumental parameters were chosen for two reasons: a) to maximize instrument sensitivity while minimizing metal oxide ($\text{CeO}^+/\text{Ce}^+ \leq 2\%$) and doubly charged ($\text{Ba}^{2+}/\text{Ba}^+ \leq 3\%$) ion ratios, and b) to ensure sampling from a similar region of the plasma as in the collision cross section measurements with the Thermo X Series II.

Results and Discussion

Determination of Ion Collision Cross-Sections Using Hexapole Collision Cell

As previously mentioned, helium is the most common collision gas for KED. The basis of KED is that ions of larger size, such as polyatomic ions, undergo more collisions and lose more kinetic energy than smaller atomic ions at the same nominal m/z value. Thus, signals from larger ions are diminished completely at a lower helium flow rate than the flow rate required to diminish monatomic ion signals of similar m/z values. We use this effect to determine the collision cross-sections of the ions coming from the plasma based on the dimensions of the collision cell and the flow rate of the collision gas applied.

The maximum kinetic energy of an ion is approximated based on the degree of ion signal lost as the pole bias of the quadrupole is made more positive. The maximum kinetic energy is

determined to be the quadrupole pole bias voltage at which the ion signal is attenuated to approximately 1% of the maximum ion signal. Tanner originally measured ion kinetic energies using modified instrumentation with a triple grid energy analyzer [22]. Some may disagree with using the quadrupole bias for measuring the maximum ion kinetic energies; however, we have measured many maximum ion kinetic energies using this technique and those kinetic energies are comparable to those measured by Tanner and by us using various instruments [22, 23, 24].

Another traditional objection to measuring kinetic energies with conventional ICP-MS instruments is the possibility that the ion lenses filter out ions of a particular kinetic energy, especially if the ions are deflected. Despite these objections, reasonable ion energies were measurable with various old instruments with photon stops in the center. Measured kinetic energies were not appreciably different with or without the photon stop [22, 24, 25, 26]. The ions in the Thermo X Series II used in the present work undergo four 90° deflections: after the skimmer the ions are bent down and then back onto the axis through the collision cell, and then up and back to the quadrupole axis after the collision cell [27]. If this ion energy filtering effect were severe, it would be difficult to transmit ions of a wide m/z range, and there would be little systematic variation of ion energy with m/z. The fact that the measured stopping curves and collision cross sections are reasonable indicates that ion energy filtering is not extreme on this instrument. Modern ICP-MS instruments are designed to transmit the most ions possible, which is not consistent with extensive ion loss due to energy filtering in the ion optics.

The maximum kinetic energies of a set of ions of similar m/z values ($^{89}\text{Y}^+$, $^{95}\text{Mo}^+$, $^{98}\text{Mo}^+$, $^{89}\text{Y}^{16}\text{O}^+$, $^{107}\text{Ag}^+$ and $^{109}\text{Ag}^+$) were determined using the quadrupole stopping curve method (Figure 1). Maximum kinetic energies were determined rather than average kinetic energies

because average kinetic energies require polynomial fits or smooth-interpolations of the stopping curves [22]. In our experience, this can be difficult due to variability in curve fitting.

As the helium flow rate in the collision cell is increased, the maximum kinetic energy of each ion decreases. The measured maximum kinetic energies of each ion at each helium flow rate are shown in Table 3. YO^+ ions have slightly lower kinetic energies than the other atomic ions, even without He in the hexapole. Tanner saw the same effect using a triple grid energy analyzer [22]. He attributed the lower kinetic energies of oxide ions to local cooling around intact wet droplets or solid particles, whose presence has been studied extensively by Olesik [28]. The fact that we also see this small effect lends credence to our contention that useful kinetic energies can be measured using the maximum stopping voltage on a quadrupole. In other words, a special instrument is not required for at least some such work.

The difference between the kinetic energies of YO^+ and M^+ is magnified when He is added. Note that the measured maximum kinetic energies are apparently negative at high flow rates, 5 mL/min He for all ions and 2.5 mL/min for YO^+ , which is not realistic physically. At these flow rates, the ions undergo so many collisions that they do not have enough kinetic energy remaining to leave the collision cell. The actual kinetic energy values are really zero in this flow rate regime. Such values are not used further in subsequent calculations.

Based on the approximate kinetic energies at each flow rate, the number of collisions undergone by each ion were determined using equation 3. These values are shown in Table 4. Two decimal places are kept for subsequent calculations even though a fraction of a collision is not physically possible.

The relationship between the collision cell gas density and the number of collisions that are undergone by an ion can be used to determine the collision cross section of that ion (Equation 1). The approximate gas density within the collision cell was calculated assuming a molecular flow regime is maintained within the collision cell at all flow rates. The calculated approximate gas densities are shown in Table 5. The number of collisions undergone by each ion were plotted versus the approximate collision cell gas densities, and the collision cross sections (Figure 2) were determined for each ion using the slope of the line and the length of the collision cell. In this case, the collision cell had a length of 13.58 cm, with one entrance and one exit aperture, both 2 mm in diameter.

An interesting scenario was found when the number of ion collisions were plotted against the collision cell gas densities. The initial plot (Figure 2), including all the points for the gas flows of 0, 0.5, 1, and 2.5 mL/min, curves upward, rather than the expected linear trend based on Equation 1. This shows that our assumption of a molecular flow regime is not valid at the higher flow rates used. Only the leftmost linear portion of the plot consisting of the 0, 0.5, and 1 mL/min helium flow rates are used to calculate the ion collision cross sections; these three points do lie close to the same straight line.

The Knudsen number (Kn) is a straightforward way to evaluate the gas flow characteristics in the collision cell:

$$Kn = \frac{\lambda}{d} \quad (4)$$

where λ is the mean free path of He (calculated $\lambda = c/p$ where c is $18.00E-3$ cm mbar for He and p is the pressure in mbar [11]) and d is a characteristic length parameter, here assumed to be the diameters of the entrance and exit apertures of the collision cell. The calculated Kn values and

corresponding He flow rates are $Kn = 22$ at 0.5 mL/min, $Kn = 11$ at 1 mL/min, and $Kn = 4.2$ at 2.5 mL/min. Kn values of 10 or higher indicate the gas flow is in the molecular flow regime [29], so curves like Figure 2 are expected to be linear only up to approximately 1 mL/min or $2E+14 \text{ cm}^{-3}$. This means that the ions and atoms traverse the openings of the collision cell without undergoing excessive collisions due to turbulent flow in the region.

The measured collision cross sections for $^{89}\text{Y}^+$, $^{95}\text{Mo}^+$, $^{98}\text{Mo}^+$, $^{89}\text{Y}^{16}\text{O}^+$, $^{107}\text{Ag}^+$ and $^{109}\text{Ag}^+$ are listed in Table 6. Very few measurements have been reported in the literature to determine the cross section of these singly charged cations; however, these values are reasonable in comparison to those measured elsewhere for monatomic cations of other elements, e.g., Rb^+ , falling within the same order of magnitude [13, 14, 15]. Armentrout's group [16] measured reduced ion mobilities ($\text{cm}^2 \text{ V}^{-1} \text{ s}^{-1}$) for Mo^+ ions using ion mobility spectrometry. Ground state Mo^+ was found to have a reduced mobility of $18.5 \pm 1.9 \text{ cm}^2 \text{ V}^{-1} \text{ s}^{-1}$ [16], which corresponds to a collision cross section of approximately $4.66E-15 \text{ cm}^2$ based on the drift cell conditions [30]. The collision cross section determined from Armentrout's measurements is approximately a factor of 3.21 larger than the measured cross section for Mo^+ shown in Table 6. Because Armentrout's instrumentation was designed specifically for the measurement of reduced ion mobility correlating to collision cross section, corrected collision cross sections were determined for $^{89}\text{Y}^+$, $^{95}\text{Mo}^+$, $^{98}\text{Mo}^+$, $^{89}\text{Y}^{16}\text{O}^+$, $^{107}\text{Ag}^+$ and $^{109}\text{Ag}^+$ assuming the difference factor of 3.21 is consistent for all of the ions (Table 6). These corrected collision cross sections were implemented for further calculations.

The difference factor of 3.21 may be accounted for in the gas density in the collision cell region. The gas density within the collision cell is estimated as described above, but the pressure in the collision cell used for this estimation is not measured directly. A gauge to do so is not

present in the collision cell of the Thermo X Series II. A more accurate gas density would require a direct measurement of the incoming pressure into the collision cell.

The collision cross sections measured for the two Mo^+ isotopes are almost the same, as are those for the two Ag^+ isotopes. It is interesting to note that Y^+ has a larger collision cross section than Mo^+ , but the collision cross section value for Ag^+ is between that for these other two elements. For neutral atoms, the atomic radii (not exactly the same thing as collision cross section) decrease smoothly going from Y through Mo to Ag. This decrease is usually attributed to more extensive shielding of the nuclear charge as more valence electrons are added [31]. In the present work, the Ag^+ ion has a measurably larger collision cross section than Mo^+ , in apparent disagreement with this trend. The electronic configuration of Ag^+ is $s^0 d^{10}$, a closed shell. In ion mobility experiments using He ($1s^2$) drift gas, atomic ions with closed shells often exhibit collision cross section values that are higher than expected due to a moderate extra interaction with He, i.e., collisions with He are slightly inelastic [32]. We found a similar effect in the Thermo X Series II; Cs^+ (electronic configuration $[\text{Xe}]$) was expected to be smaller than Ba^+ ($[\text{Xe}]s^1$), but Cs^+ had about the same collision cross section as Ba^+ [33]. The electronic configuration of Y^+ of s^2 , a closed shell as well, may also explain why the measured collision cross section of Y^+ is larger than that for Mo^+ .

Determination of CRI Dimensions and Conditions

The premise behind the CRI is the same as that of a collision cell; however, higher flow rates are necessary to achieve comparable kinetic energy losses with the CRI. Similar to the previous collision cell experiment, the approximate maximum kinetic energies of $^{89}\text{Y}^+$, $^{95}\text{Mo}^+$, $^{98}\text{Mo}^+$, $^{89}\text{Y}^{16}\text{O}^+$, $^{107}\text{Ag}^+$ and $^{109}\text{Ag}^+$ were determined on the CRI instrument based on the quadrupole stopping curves at helium flow rates through the skimmer cone of 0, 30, 70, and 100

mL/min. For these measurements, it was assumed that the ion mirror, which deflects the ion beam 90° into the mass analyzer, does not filter the ions based on kinetic energy, at least not severely. This assumption is confirmed by the variation of maximum kinetic energies with m/z for the Aurora Elite shown in Figure 3. This range is comparable to the kinetic energies measured by various older ICP-MS instruments, as previously discussed [22, 24, 25, 26].

The pole bias versus ion signal plots for the CRI instrument are shown in Figure 4. Again YO^+ ions have a measurably lower kinetic energy than nearby atomic ions. It is difficult to compare kinetic energy loss between the collision cell and the CRI because of the large difference in the helium gas flows required. At a glance, it is noticeable that ions undergo more kinetic energy loss and there is a larger difference in kinetic energy between the polyatomic oxide ion ($^{89}\text{Y}^{16}\text{O}^+$) and the nearby ions of similar masses ($^{89}\text{Y}^+$, $^{95}\text{Mo}^+$, $^{98}\text{Mo}^+$, $^{107}\text{Ag}^+$ and $^{109}\text{Ag}^+$) in the collision cell instrument. The ion signals for $^{89}\text{Y}^{16}\text{O}^+$ become unstable at high He flow rates in the CRI because the $^{89}\text{Y}^{16}\text{O}^+$ ions are attenuated so extensively and approach the instrumental limit of detection as the helium gas flow is increased. The ability to measure stopping curves for low-abundance ions on the Aurora Elite is limited by its detector. When the instrument is in CRI mode, the detector can only measure signal levels up to $\sim 10^7$ c/s. To stay within this signal range, the yttrium concentration of the analyzed solution was adjusted; however, signal loss of the $^{89}\text{Y}^{16}\text{O}^+$ ions caused by collisions restricted the ability to measure the pole bias curves for both the $^{89}\text{Y}^{16}\text{O}^+$ and the $^{89}\text{Y}^+$ ions using the same Y solution.

From the pole bias curves, the maximum kinetic energies and the number of collisions undergone by each ion were determined using the same methods as the previous collision cell experiment. These values are presented in Tables 7 and 8. Comparing the values achieved with the CRI to the collision cell, it appears that ~ 30 mL/min of helium through the CRI generates

approximately the same number of collisions as 0.5 mL/min of helium through the much longer (13.58 cm) hexapole collision cell in the Thermo X Series II.

Using the corrected collision cross sections determined in the collision cell experiment and the calculated number of collisions undergone in the CRI, the product nL (i.e., the gas density multiplied by the length of the collision region) in the CRI can be determined. The calculated nL product value for each ion and an average for each helium flow rate are shown in Table 9. From the average nL product values, it is possible to establish a general understanding of the underlying CRI dynamics and dimensions.

One concern with comparing the CRI to a collision cell is the shape of the CRI collision region. Figure 5 shows a generic depiction of the CRI arrangement. Note that the CRI skimmer cone has a conical shape unlike a cylindrical collision cell. We assume that the shape of the collision region is not a big factor. Another concern is the distance downstream from the CRI skimmer tip where the collisions occur. The gas density here changes with axial position, whereas it is constant with a multipole collision cell. It is highly probable that most of the collisions take place near the skimmer tip between the edges of the skimmer cone opening through which the helium is supplied. The exact scenario in which the collisions take place is unknown.

For sake of argument, suppose that 99% of the collisions occur before the ions travel 2 mm downstream from the skimmer tip, the approximate distance between the edges of the skimmer cone opening (Figure 5). An approximate average gas density can be calculated for the 2 mm CRI collision region. With these caveats, the average gas density was estimated to be $2.2E+15 \text{ cm}^{-3}$ at 30 mL/min He, $6.0E+15 \text{ cm}^{-3}$ at 70 mL/min, and $9.0E+15 \text{ cm}^{-3}$ at 100 mL/min. These gas density values appear to be reasonable for adequate collisions to occur in the CRI

collision region. The gas density in the supersonic beam entering the skimmer tip is estimated to be approximately $1\text{E}+16\text{ cm}^{-3}$ [26], comparable to the CRI gas densities cited above. If the gas density in the CRI region were much higher than this value, the beam from the sampler would not penetrate through the skimmer efficiently [34].

Conclusion

The collision cross sections of $^{89}\text{Y}^+$, $^{95}\text{Mo}^+$, $^{98}\text{Mo}^+$, $^{89}\text{Y}^{16}\text{O}^+$, $^{107}\text{Ag}^+$ and $^{109}\text{Ag}^+$ ions were determined using the known characteristics of the collision cell in the Thermo X Series II ICP-MS and the kinetic energy suppression caused with increasing helium gas flow. These ions were found to have collision cross sections in the 10^{-15} cm^2 range. The determined values were found to be comparable to published cation collision cross sections and known periodic trends.

Based on the calculated cross sections, general characteristics were determined for the CRI collision region in an Aurora Elite ICP-MS. The general assumptions made to determine these characteristics were (1) plasma conditions and the electronic energy level distribution of each ion were very similar between ICP-MS instruments implemented, (2) the shape of the collision region does not have an influence on the relationship between the number of collisions undergone by an ion and the ion's collision cross section, and (3) 99% of the collisions take place in very close proximity to the CRI skimmer cone tip spanning a density gradient of length $\sim 2\text{ mm}$. Based on these assumptions, the density in the collision region was determined to range from $\sim 2.2\text{E}+15\text{ cm}^{-3}$ to $\sim 9.0\text{E}+15\text{ cm}^{-3}$ with increasing helium flow rate from 30 mL/min to 100 mL/min. These calculated densities, based on the ideal gas law, allow adequate collisions to occur in the CRI collision region, while still allowing ions from the plasma to transverse into the mass spectrometer for detection.

Further work on this general topic could address the influence of the extraction lenses following the CRI skimmer cone. It is expected that the position and diameter of the first extraction lens may play a crucial role in the resulting gas density in the CRI collision region. This may be addressed by modification of the first extraction lens, i.e. changing the position and/or diameter. It may also be addressed by gas flow simulations based on collision gas flow rates, measured skimmer cone dimensions, and the assumed skimmer cone shape. Simulations may also contribute more information to the research previously discussed.

Acknowledgements

This work was performed at the Ames Laboratory. The authors thank Iouri Kalinitchenko and Andrew Toms for information provided about the Aurora Elite ICP-MS. The authors also thank Wenyu Huang for use of the Thermo X Series II ICP-MS and Mike Plantz for information pertaining to the collision cell in the Thermo X Series II.

References

- [1] D. J. Douglas, J. B. French, Collisional Focusing Effects in Radio Frequency Quadrupoles, *J. Am. Soc. Mass Spectrom.* 3 (1992) 398-408.
- [2] N. Yamada, J. Takahashi, K. Sakata, The effects of cell-gas impurities and kinetic energy discrimination in an octopole collision cell ICP-MS under non-thermalized conditions, *J. Anal. At. spectrom.* 17 (2002) 1213-1222.
- [3] S. D. Tanner, V. I. Baranov, D. R. Bandura, Reaction cells and collision cells for ICP-MS: a tutorial review, *Spectrochim. Acta Part B* 57 (2002) 1361-1452.
- [4] S. Zhang, W.-h. Zhang, Z.-r. Li, Z.-g. Jiang, J.-t. Wang, F.-l. Liang, New dry ashing-wet digestion method and ICP-MS determine the content of titanium dioxide in foods, *Shipin Yanjiu Yu Kaifa* 34 (2013) 77-80.

- [5] W. Cieslak, K. Pap, D. R. Bunch, E. Reineks, R. Jackson, R. Steinle, S. Wang, Highly sensitive measurement of whole blood chromium by inductively coupled plasma mass spectrometry, *Clin. Biochem.* 46 (2013) 266-270.
- [6] A. Liba, Transforming ICP-MS technology: advances in interference removal for accurate arsenic analysis in food and beverages, in Abstract of Paper, 245th ACS National Meeting & Exposition, New Orleans, LA, (2013).
- [7] N. I. Rousis, I. N. Pasiadis, N. S. Thomaidis, Attenuation of interference in collision/reaction cell inductively coupled plasma mass spectrometry, using helium and hydrogen as cell-gases - application in multi-element analysis of mastic gum, *Anal. Methods* 6 (2014) 5899-5908.
- [8] D. J. Douglas, Some Current Perspectives on ICP-MS, *Can. J. Spectrosc.* 34 (1989) 38-49.
- [9] J. T. Rowan, R. S. Houk, Attenuation of polyatomic ion interferences in inductively coupled plasma mass spectrometry by gas-phase collisions, *Appl. Spectrosc.* 43 (1989) 976-980.
- [10] X. Wang, I. Kalinitchenko, Fundamental and Practical Aspects of the CRI Technology for ICP-MS, (2007).
- [11] Leybold-Heraeus Vacuum Products Inc., Vacuum Technology, Its Foundations, Formulae and Tables, 2001.
- [12] T. Covey, D. J. Douglas, Collision Cross Section of Protein Ions, *J. Am. Soc. Mass Spectrom.* 4 (1993) 616-623.
- [13] H. W. Ellis, R. Y. Pai, E. W. McDaniel, E. A. Mason, L. A. Viehland, Transport properties of gaseous ions over a wide energy range, *At. Data Nucl. Data Tables* 17 (1976) 177-210.
- [14] H. W. Ellis, E. W. McDaniel, D. L. Albritton, L. A. Viehland, S. L. Lin, E. A. Mason, Transport properties of gaseous ions over a wide energy range: part 2, *At. Data Nucl. Data Tables* 22 (1978) 179-217.
- [15] H. W. Ellis, M. G. Thackston, E. W. McDaniel, E. A. Mason, Transport properties of gaseous ions over a wide energy range: part 3, *At. Data Nucl. Data Tables* 31 (1984) 113-151.
- [16] C. Iceman, C. Rue, R. M. Moision, B. K. Chatterjee, P. B. Armentrout, Ion mobility studies of electronically excited states of atomic transition metal cations: Development of an ion mobility source for guided ion beam experiments, *J. Am. Soc. Mass Spectrom.* 18 (2007) 1196-1205.

- [17] A. A. Mills, J. H. Macedone, P. B. Farnsworth, High resolution imaging of barium ions and atoms near the sampling cone of an inductively coupled plasma mass spectrometer, *Spectrochim. Acta Part B* 61 (2006) 1039-1049.
- [18] J. L. Jacobs, R. S. Houk, Updated ionization efficiency calculations of inductively coupled plasma mass spectrometry, Unpublished Work, Iowa State University (2015).
- [19] R. S. Houk, N. Praphairaksit, Dissociation of polyatomic ions in the inductively coupled plasma, *Spectrochim. Acta Part B* 56 (2001) 1069-1096.
- [20] S. M. McIntyre, J. W. Ferguson, R. S. Houk, Determination of dissociation temperature of ArO^+ in inductively coupled plasma-mass spectrometry: Effects of excited electronic states and dissociation pathways, *Spectrochim. Acta Part B* 66 (2011) 581-587.
- [21] S. M. McIntyre, J. W. Ferguson, T. M. Witte, R. S. Houk, Measurement of gas kinetic temperatures for polyatomic ions in inductively coupled-plasma spectrometry: Validation and refinement, *Spectrochim. Acta Part B* 66 (2011) 248-254.
- [22] S. D. Tanner, Plasma temperature from ion kinetic energies and implications for the source of diatomic oxide ions in inductively coupled plasma mass spectrometry, *J. Anal. Atom. Spectrom.* 8 (1993) 891-897.
- [23] J. A. Olivares, R. S. Houk, Kinetic energy distribution of positive ion in an inductively coupled plasma mass spectrometer, *Appl. Spectrosc.* 39 (1985) 1070-1077.
- [24] C. H. Ebert, T. M. Witte, R. S. Houk, Investigation into the behavior of metal-argon polyatomic ion (MAr^+) in the extraction region of inductively coupled plasma-mass spectrometry, *Spectrochim. Acta Part B* 76 (2012) 119-125.
- [25] A. Montaser, H. Tan, I. Ishii, S.-H. Nam, M. Cai, Argon inductively coupled plasma mass spectrometry with thermospray, ultrasonic, and pneumatic nebulization, *Anal. Chem.* 63 (1991) 2660-2665.
- [26] K. E. Jarvis, A. L. Gray, R. S. Houk, *Handbook of Inductively Coupled Plasma Mass Spectrometry*, New York: Blackie and Son, Ltd, 1992.
- [27] R. S. Houk, ICP-MS Short Course I, Pittsburgh Conference, 2015.
- [28] J. W. Olesik, Investigating the fate of individual sample droplets in inductively coupled plasmas, *Appl. Spectrosc.* 51 (1997) 158A-175A.
- [29] D. S. Gaal, P. S. Gaal, *Thermal Conductivity 30: Thermal Expansion 18*, Pittsburgh, 2009.

- [30] T. Wyttenbach, J. Gidden, M. T. Bowers, Developments in ion mobility: Theory, instrumentation, and applications, in C.L. Wilkins, S. Trimpin, Ion mobility spectrometry - mass spectrometry, Boca Raton, Taylor and Francis Group, LLC, 2011, pp. 3-30.
- [31] L. S. Brown, T. A. Holme, Chemistry for Engineering Students, 3rd edition, Stamford, CT: Cengage Learning, 2011.
- [32] E. A. Mason, E. W. McDaniel, Transport Properties of Ions in Gases, New York: John Wiley & Sons, Inc., 1988.
- [33] C. Ebert, Unpublished Work, Iowa State University.
- [34] N. Baylor, P. B. Farnsworth, Experimental characterization of the effect of skimmer cone design on shock formation and ion transmission efficiency in the vacuum interface of an inductively coupled plasma mass spectrometer, Spectrochim. Acta Part B 69 (2012) 2-8.
- [35] Aurora Elite ICP-MS Software.

Table 1: Thermo X-Series II instrumental parameters

Parameter	Value
Extraction Lens (V)	approximately -382 (optimized by instrument)
Lens 1 (V)	-1400
Lens 2 (V)	-97.3
Focus (V)	12.5
D1 (V)	-47.8
D2 (V)	-143
Hexapole Bias (V)	0.7
Nebulizer (L/min)	0.88
Lens 3 (V)	-182.7
Forward Power (Watts)	1000
Horizontal	40
Vertical	457
DA (V)	-43.9
Cool Gas Flow (L/min)	13.9
Auxiliary Gas Flow (L/min)	0.82
Sampling Position	226 (on center)

Table 2: Aurora Elite instrumental parameters

Parameter	Value
Flow Parameters (L/min)	
Outer Gas Flow	18.0
Sheath Gas	0.30
Nebulizer Flow	0.99
Torch Alignment (mm)	
Sampling Depth	6.5
Other	
RF Power (kW)	1.40
Pump Rate (rpm)	5
Stabilization delay (s)	30
Ion Optics (volts)	
First Extraction Lens	-38
Second Extraction Lens	-212
Third Extraction Lens	-399
Corner Lens	-383
Mirror Lens Left	60
Mirror Lens Bottom	49
Entrance Lens	6
Fringe Bias	-4.7
Entrance Plate	-45

Table 3: The maximum kinetic energy (eV) of each ion at each helium flow rate in a collision cell. The reproducibility of maximum kinetic energy based on the stopping curves is ~0.1 eV.

Helium Flow Rate (mL/min)	$^{89}\text{Y}^+$	$^{95}\text{Mo}^+$	$^{98}\text{Mo}^+$	$^{89}\text{Y}^{16}\text{O}^+$	$^{107}\text{Ag}^+$	$^{109}\text{Ag}^+$
0	3.96	4.06	4.11	3.77	4.27	4.31
0.5	3.07	3.32	3.38	2.58	3.51	3.55
1	2.64	2.99	3.04	1.70	3.16	3.19
2.5	0.68	1.16	1.21	-0.10	1.22	1.24
5	-0.32	-0.18	-0.18	-0.71	-0.26	-0.26

Table 4: The number of collisions undergone by each ion at each helium flow rate in a collision cell

Helium Flow Rate (mL/min)	$^{89}\text{Y}^+$	$^{95}\text{Mo}^+$	$^{98}\text{Mo}^+$	$^{89}\text{Y}^{16}\text{O}^+$	$^{107}\text{Ag}^+$	$^{109}\text{Ag}^+$
0	Assumed 0 Collisions					
0.5	2.93	2.50	2.51	5.18	2.71	2.74
1	4.71	3.78	3.83	10.87	4.17	4.28
2.5	20.58	15.48	15.61	--	17.45	17.61
5	--	--	--	--	--	--

Table 5: Calculated approximate gas density (n) at each helium flow rate in a collision cell

Helium Flow Rate (mL/min)	Gas Density (cm^{-3})
0	0
0.5	1.03 E +14
1	2.06 E +14
2.5	5.14 E +14
5	1.03 E +15

Table 6: Ion collision cross sections

Ion	Measured Collision Cross Section (cm^2) (\pm Standard Deviation)	Corrected Collision Cross Section (cm^2) (Reference [16])
$^{89}\text{Y}^+$	1.77E-15 (\pm 1.17E-16)	5.68E-15
$^{95}\text{Mo}^+$	1.44E-15 (\pm 1.24E-16)	4.62E-15
$^{98}\text{Mo}^+$	1.46E-15 (\pm 1.20E-16)	4.68E-15
$^{89}\text{Y}^{16}\text{O}^+$	3.85E-15 (\pm 5.19E-16)	12.4E-15
$^{107}\text{Ag}^+$	1.58E-15 (\pm 1.26E-16)	5.08E-15
$^{109}\text{Ag}^+$	1.62E-15 (\pm 1.23E-16)	5.19E-15

Table 7: Maximum kinetic energy (eV) at each helium flow rate in a collision reaction interface. The reproducibility of maximum kinetic energy based on the stopping curves is ~0.1 eV.

Helium Flow Rate (mL/min)	$^{89}\text{Y}^+$	$^{95}\text{Mo}^+$	$^{98}\text{Mo}^+$	$^{89}\text{Y}^{16}\text{O}^+$	$^{107}\text{Ag}^+$	$^{109}\text{Ag}^+$
0	2.64	2.70	2.72	2.76	2.84	2.88
30	2.01	2.30	2.33	1.94	2.46	2.48
70	1.47	1.73	1.73	1.16	1.76	1.77
100	1.03	1.36	1.41	0.72	1.43	1.45

Table 8: The number of collisions undergone by each ion at each helium flow rate in a collision reaction interface

Helium Flow Rate (mL/min)	$^{89}\text{Y}^+$	$^{95}\text{Mo}^+$	$^{98}\text{Mo}^+$	$^{89}\text{Y}^{16}\text{O}^+$	$^{107}\text{Ag}^+$	$^{109}\text{Ag}^+$
0	Assumed 0 Collisions					
30	3.15	2.02	1.94	4.80	1.99	2.11
70	6.81	5.51	5.68	11.80	6.67	6.86
100	10.93	8.48	8.33	18.36	9.52	9.66

Table 9: The calculated gas density (n) times collision region length (L) for CRI in terms of each measured isotope at each helium flow rate. The lower table shows the calculated average at each helium flow rate.

Helium Flow Rate (mL/min)	Calculated n * L for each isotope (cm ⁻²)					
	$^{89}\text{Y}^+$	$^{95}\text{Mo}^+$	$^{98}\text{Mo}^+$	$^{89}\text{Y}^{16}\text{O}^+$	$^{107}\text{Ag}^+$	$^{109}\text{Ag}^+$
30	5.54E+14	4.36E+14	4.14E+14	3.88E+14	3.91E+14	4.06E+14
70	1.20E+15	1.19E+15	1.21E+15	9.54E+14	1.31E+15	1.32E+15
100	1.92E+15	1.83E+15	1.78E+15	1.48E+15	1.87E+15	1.86E+15

Helium Flow Rate (mL/min)	Average n * L (cm ⁻²) (± Standard Deviation)
30	4.32E+14 (± 5.71E+13)
70	1.20E+15 (± 1.21E+14)
100	1.79E+15 (± 1.44E+14)

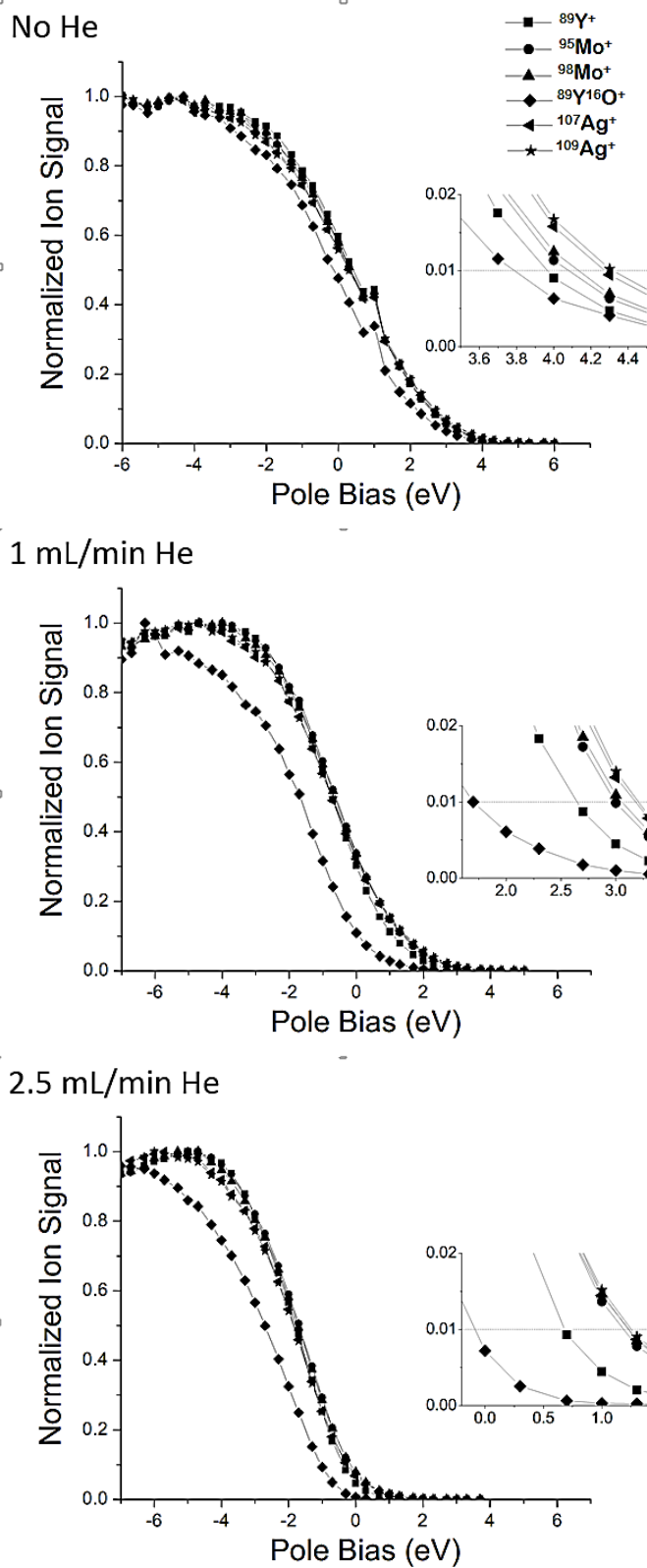


Figure 1: Plots of pole bias vs. normalized ion signal for helium flow rates of 0, 1, and 2.5 mL/min in the collision cell of a Thermo X-Series II. Note that YO^+ has the lowest maximum kinetic energy when no He is added. This is also consistent with Tanner's measurements [22].

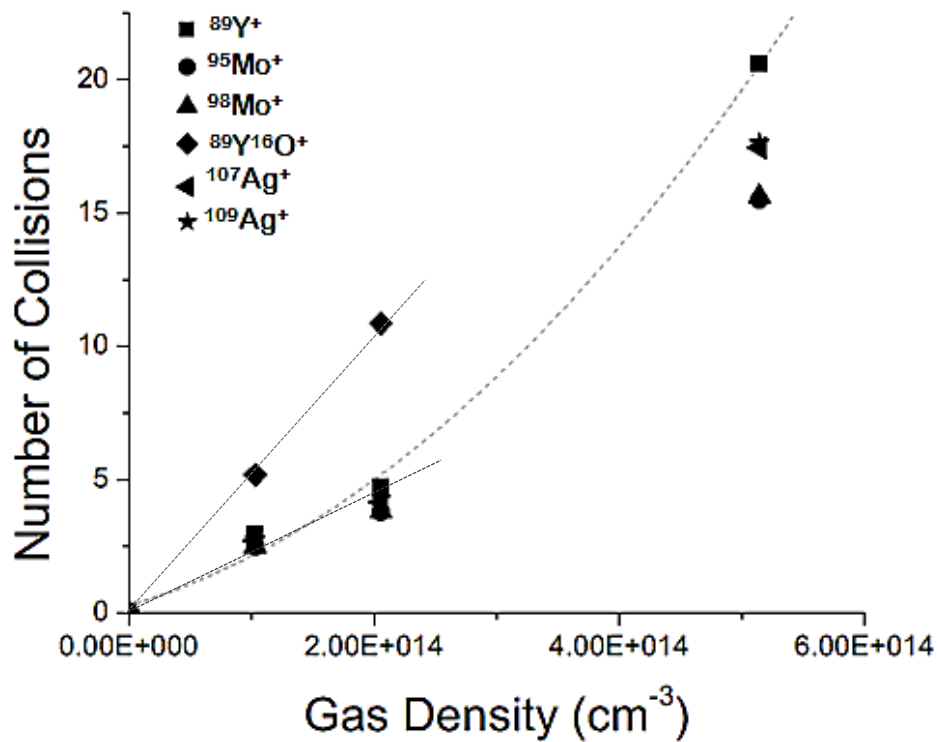


Figure 2: The number of collisions undergone by each ion plotted against the collision cell gas density. The linear trend turns into a curved trend as the density, or flow rate of helium, within the collision cell is increased after 1 mL/min. This is indicative of a change in flow regime with increasing flow rate. Only the leftmost linear point were used for calculation purposes.

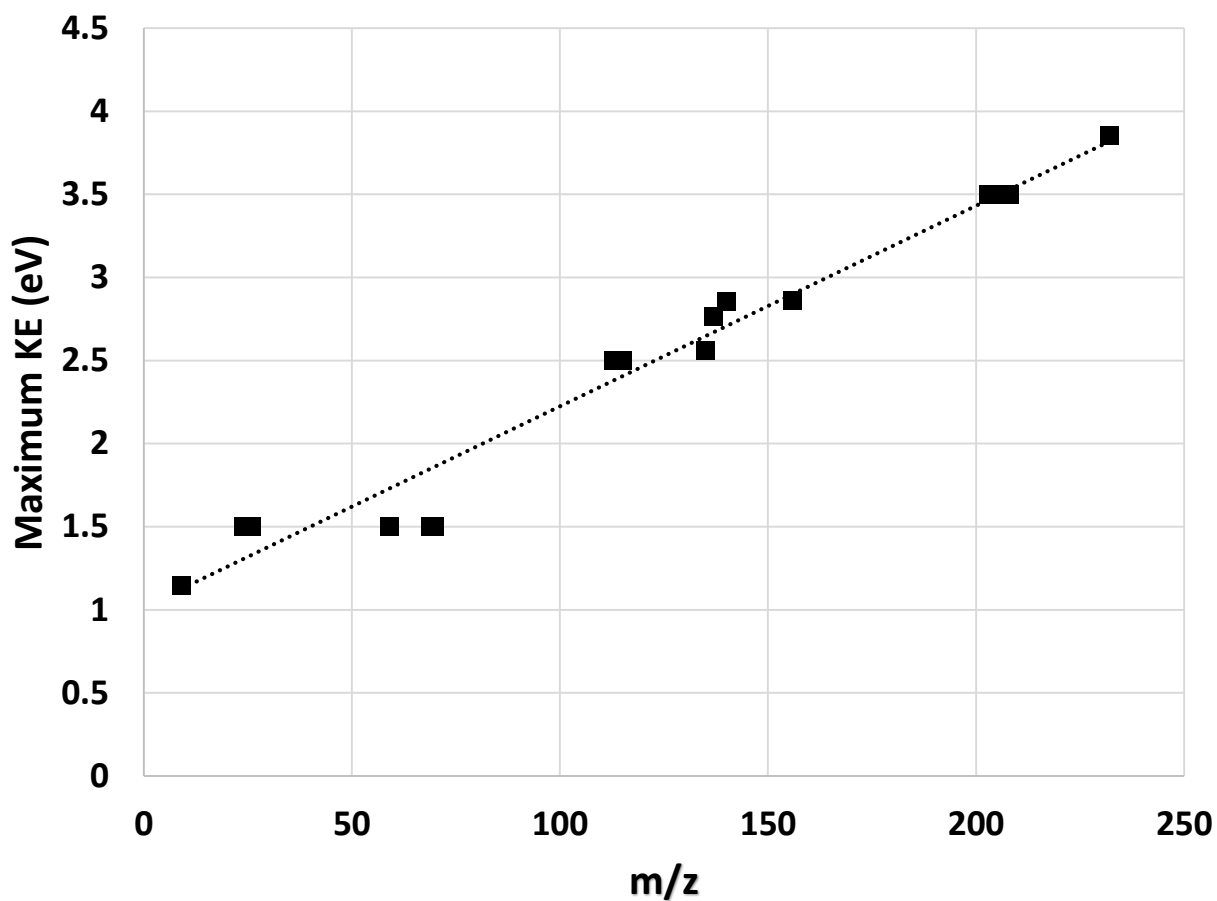


Figure 3: The measured maximum kinetic energies with increasing m/z in the Aurora Elite ICP-MS. This plot show that the measured maximum kinetic energies in this instrument containing an ion mirror are comparable to the maximum kinetic energies measured in older ICP-MS instrument.

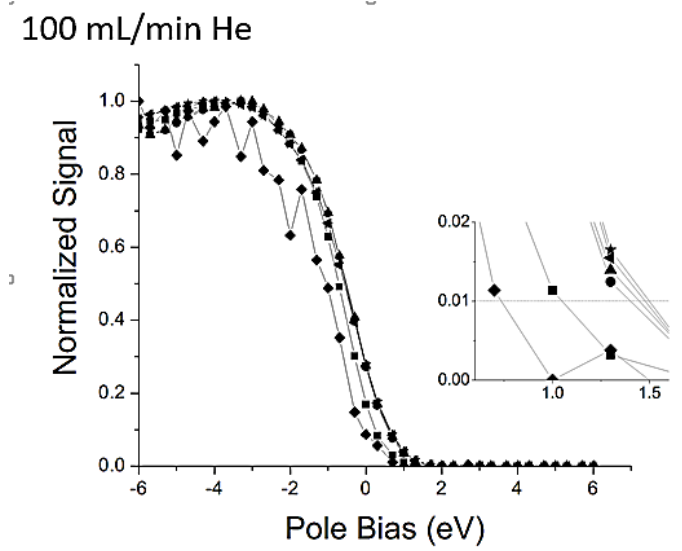
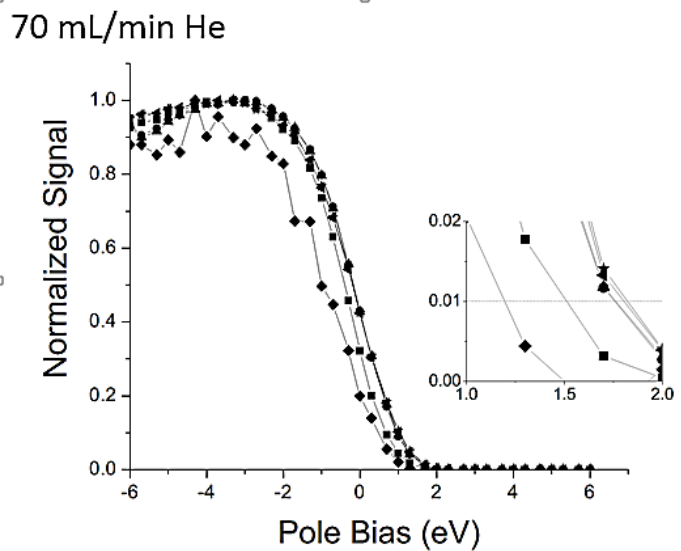
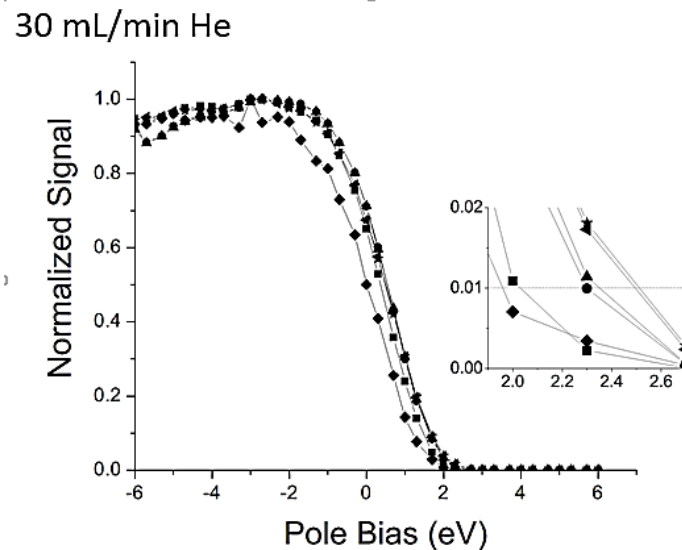
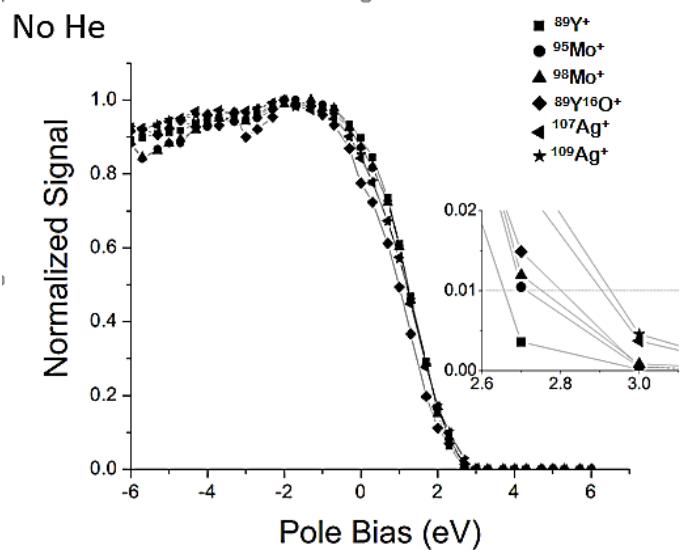


Figure 9: Plots of pole bias vs. normalized ion signal for helium flow rates of 0, 30, 70, and 100 mL/min in the collision reaction interface of the Aurora Elite ICP-MS.

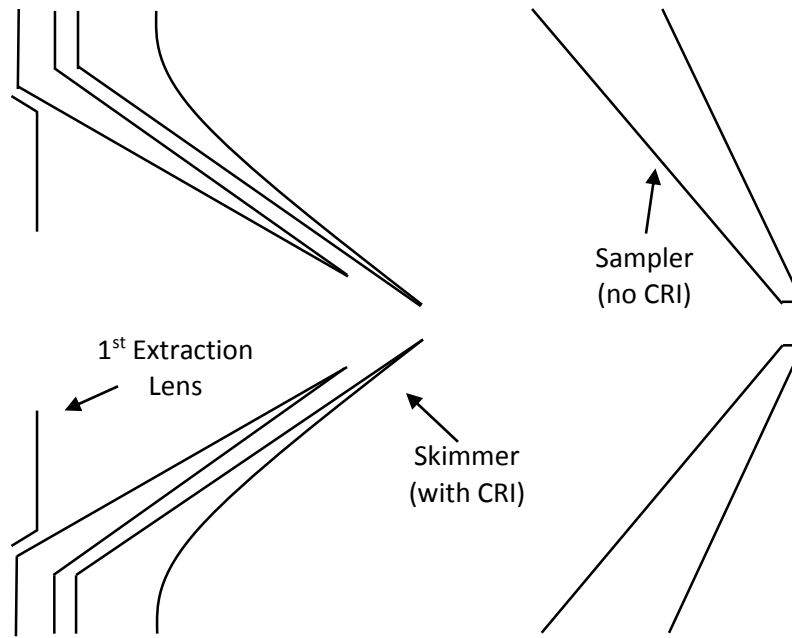


Figure 5: Depiction of the CRI skimmer cone and the CRI collision region (Redrawn from [35])

CHAPTER 4. THE FORMATION OF SECONDARY METAL

MONOHYDRIDE IONS IN ICP-MS

WITH THE COLLISION REACTION INTERFACE

J.L. Jacobs and R.S. Houk

Abstract

One of the technologies available for the mitigation of polyatomic interference ions in ICP-MS is the collision reaction interface (CRI). The CRI introduces collision gas directly into the plasma expansion, which provides for many collisions. One concern with implementing H₂ as a reaction gas via the CRI is the possible formation of monohydride ions (MH⁺, M = atomic ion). This study focuses on the formation of MH⁺ ions and the influence of increasing H₂ gas flow through the CRI skimmer cone. It was found that no other new background ions were formed due to the addition of H₂ gas. For some analyte ions, specifically U and Sb, additional MH⁺ ions are formed; however these ions are suppressed as H₂ gas flow is increased. Finally, ion kinetic energy measurements provide insight into the source of MH⁺ ion formation in the CRI and plasma expansion regions.

Introduction

Polyatomic ions are often a major concern in inductively coupled plasma mass spectrometry (ICP-MS) analyses. Polyatomic ions have the same nominal mass-to-charge ratio (m/z) as the analyte ions of interest, which prevents accurate quantification of those analyte ions. Low resolution quadrupole mass spectrometers generally cannot separate these polyatomic and

analyte ions via the mass analyzer alone. High resolution instrumentation is capable of separating most polyatomic ions, but the cost and complexity of this instrumentation is high. Low resolution instrumentation requires additional mitigation techniques to remove polyatomic ion interferences prior to ion detection.

Collision methods are most often the interference mitigation technique of choice in low resolution quadrupole instrumentation. Multiple types of collision technologies are available for this purpose; the most common is the collision cell. A collision cell is an enclosed set of quadrupole, hexapole, or octopole rods placed between the skimmer and the mass analyzer. In the collision cell, a gas is added to remove polyatomic ions through either kinetic energy discrimination or chemical reactions. Kinetic energy discrimination (KED) uses collisions to dampen the ion energies of the larger polyatomic ions, which prevents the ions from being transmitted by the mass analyzer [1]. Helium is often used for the removal of polyatomic ions in this manner [2]. Reactive gases, on the other hand, convert troublesome polyatomic ions to species at a different m/z value. A variety of reactive gases are available. Hydrogen (H_2) is commonly used on various instruments for the removal of argon adducts, such as ArO^+ , ArN^+ , Ar_2^+ and $ArCl^+$, which are often present in abundance due to the argon plasma gas [3].

Another collision technology available, but as yet less widely implemented, is the collision reaction interface (CRI). The premise behind CRI technology is very similar to that of the collision cell. Interference ions are removed via either KED or reactions via a reaction gas. The CRI introduces the collision gas directly into the plasma expansion at either the tip of the sampler and/or skimmer cones [4]. Collisions in the skimmer cone have come to be used more often than the sampler [5]. Implementation of a collision or reaction gas directly in the plasma expansion region is advantageous because the region is very small, which allows for the identity

and density of the collision gas to be changed very quickly. Also, the plasma expansion region has a high gas density which increases the likelihood of many collisions [4]. Helium and/or hydrogen are most often the gases implemented for interference removal via the CRI.

One concern with adding H_2 into the dense expansion region of the plasma is the possible formation of MH^+ ions or other polyatomic ions, which may lead to worse interferences. “New” polyatomic ions (i.e., species not observed from the plasma itself) made in other collision cells are attenuated by kinetic energy, the m/z window on the collision cell, or prior m/z analysis [6]. The latter two options are not available in instrumentation with CRI technology. Very little research has been performed to determine if interference ions are produced when H_2 is applied as a reaction gas with the CRI.

In this paper, background spectra are measured with increasing H_2 flow rate to determine if additional background polyatomic ions are formed due to reactions of background ions with the H_2 added through the skimmer. Subsequently, analyte ions are added to determine if H_2 reacts with those analyte ions to form MH^+ ions. Uranium was chosen for this study because it is known to form a small amount of MH^+ ions, probably in the plasma, and is often an issue in accurate plutonium measurements [7, 8]. Also, no interfering species are present at m/z 239 due to plutonium being a synthetic element. Antimony was chosen because it is not known to form MH^+ ions in the plasma prior to extraction, and therefore, if SbH^+ ions are formed, they are definitely made in the CRI. Antimony is also closer to the mass range in which CRI technology would generally be implemented. Following the initial experiments, variations in instrumental parameters and their influences on MH^+ ion signals, and kinetic energy comparisons of MH^+ ions and their parent ions are discussed. The primary goal of these experiments is to deliberately

make a polyatomic ion only, or mostly, in the CRI region, and then determine why few such ions are seen normally.

In many analyses performed using ICP-MS, the presence of small amounts of MH^+ ions would not have a significant effect on the results. The main scenarios in which MH^+ ions would be of concern are those in which highly precise measurements of trace elements at m/z values adjacent to the major elements are necessary. For example, if trace levels of Pr at m/z 141 need to be measured in a concentrated Ce solution and if CeH^+ ions are present, quantification of Pr will be difficult. MH^+ ions have already been determined as an issue in accurate plutonium measurements when uranium is present [7]. Another potential problem is high precision isotope ratio measurements. In geochemistry, miniscule errors in isotope ratios play a very large role in dating determinations. If MH^+ ions are present, even at very low MH^+/M^+ signal ratios, the dating determination based on those isotopes may be inaccurate. This paper is not meant to discuss if all metal ions interact with H_2 to form MH^+ ions; however, it is meant to determine if MH^+ ions are a possibility in ICP-MS analyses and if CRI technology influences their abundance.

Experimental

Reagents and Materials

All standard solutions were prepared by serial dilution of commercially available single element standards (PlasmaChem Associates, Inc.) with 1% nitric acid. The 1% nitric acid solution was prepared by dilution of concentrated 70 % nitric acid (HNO_3 , Fisher Scientific) with deionized water (18 $M\Omega$ cm, Barnsted Nanopure). The concentrated HNO_3 was purified via sub-

boiling distillation (Savillex) prior to use. All solutions were prepared in clean plastic Nalgene bottles.

Industrial grade argon (99.995 % purity, Matheson) was used for plasma generation.

Zero grade hydrogen (99.999 % purity, Matheson) was used as a collision gas.

Instrumentation

All analyses were performed using an Aurora Elite ICP-MS (formerly Bruker Daltonics, now Analytik Jena). The metal solutions were pumped peristaltically into a low flow nebulizer (Micro Mist) with an uptake rate of approximately 220 $\mu\text{L}/\text{min}$ and an approximate sample argon gas flow rate of 1.00 L/min. A peltier cooled quartz double pass spray chamber was used at a temperature of 3°C. The demountable quartz torch was positioned on center approximately 6 mm from the sampler cone orifice and the additional gas flows were set at 0.3, 1.8, and 18 L/min for the sheath, auxiliary, and cool gases, respectively.

Grounded nickel cones were used at the interface between the inductively coupled plasma and the mass spectrometer. The sampler was a single cone, i.e. it had no CRI capabilities. The skimmer was a double cone equipped with CRI capabilities which allows for the addition of H₂ or He as a collision gas. Hydrogen was added at various flow rates, ranging from 0 mL/min to 120 mL/min, for each experiment discussed.

The ion optic voltages following the interface were optimized for each experiment discussed. In most of the experiments, the optics were optimized for normal instrument sensitivity. Normal instrument sensitivity maximized singly charged ion signals and minimized metal oxide ions ($\text{CeO}^+/\text{Ce}^+ < 2\%$) and doubly charged ions ($\text{Ba}^{2+}/\text{Ba}^+ < 3\%$) signal ratios. The

software uses an optimization algorithm that focuses on the signals of Be^+ , In^+ , Ba^+ , Ba^{++} , Ce^+ , CeO^+ , and Th^+ to achieve these optimum conditions.

In a few experiments, the optimization algorithm used by the software for optimization was edited to maximize specific ions of interest and/or optimize voltages only on specific components of the ion optics. The optimization algorithm was edited using the Setup Optimization software. The ion optics of the Aurora Elite differ from those in other commercially available quadrupole mass spectrometers due to the introduction of a mirror lens that directs the ion beam 90° from its original trajectory. The mirror lens is one of the main ion optic components of interest in this study on the formation of MH^+ ions.

Results and Discussion

Comparison of Background Spectra

Background spectra were analyzed at various H_2 flow rates to determine if new or additional background ions are formed in the CRI. Full mass spectra were taken of 1% nitric acid solutions at H_2 flow rates from 0 mL/min to 120 mL/min at intervals of 10 mL/min. A few of these spectra are shown in figure 1. Normal instrument sensitivity optimization parameters were used for this comparison.

A comparison of the spectra at each flow rate shows that no notable new background polyatomic ions are formed when adding H_2 through the CRI skimmer cone. Most of the polyatomic ions that are formed are consistent with those expected from reactions of H_2 with major background ions, especially O^+ , H_2O^+ , and Ar^+ . These ions are initially present in the plasma without the addition of H_2 via the CRI. Figure 1 shows that the signals increase initially with H_2 gas flow rate (up to approximately 30 mL/min) for mass-to-charge values corresponding

to H_3^+ , H_2O^+ , H_3O^+ , HO_2^+ , ArH^+ , ArH_2^+ , and ArH_3^+ . As the H_2 flow rate is increased past 30 mL/min, these signals drop and eventually approach zero.

The suppression of all these ions (H_3^+ , H_2O^+ , H_3O^+ , HO_2^+ , ArH^+ , ArH_2^+ , and ArH_3^+) at high H_2 flow rate is analytically valuable. This effect is likely caused by both a) extensive chemical reactions ending in H_3^+ and H_3O^+ , and b) collision-induced reduction of ion kinetic energies that ultimately prevents the background ions from being transmitted into the mass analyzer. Note that the production of vast amounts of new ions does not persist at very high H_2 flow rates (> 90 mL/min). The only product ions still remaining are small amounts of H_3O^+ and H_3^+ . These ions are expected and are likely product ions of multiple sequential reactions between original background ions from the ICP, initial product ions formed by early reaction between ions and H_2 , and multiple succeeding reactions.

Formation of Metal Monohydride (MH^+) Ions

The lack of polyatomic ions at high H_2 flow rates raises the question: what happens to the product ions formed by reactions of H_2 with background ions? To study this question we looked for polyatomic ions not originally present, i.e., ions made only in the CRI collision region. Tests for MH^+ ions were performed initially at H_2 flow rates that were representative of the typical operating range for H_2 with the CRI skimmer cone. Antimony, uranium, and their corresponding MH^+ ion signals were measured at H_2 flow rates of 0 mL/min, 80 mL/min, and 90 mL/min through the skimmer cone. The ion optics were optimized for normal instrument sensitivity.

With no H_2 flowing through the CRI skimmer cone, the signal ratios for SbH^+/Sb^+ and UH^+/U^+ were measured to fall between $\sim 1 \times 10^{-5}$ and 3×10^{-5} . For MH^+ ions directly from the

ICP, the signals are low and unstable. Comparable UH^+/U^+ signal ratios ($\sim 10^{-6}$) were found by Taylor et al. using a magnetic sector multicollector instrument [7]. When H_2 gas was added at 80 mL/min, which is the low end of the normal CRI operating range, the UH^+/U^+ signal ratio increased significantly to $\sim 6 \times 10^{-3}$. Figure 2 shows a spectrum of U^+ and UH^+ at m/z 238 and 239; these ions are clearly resolved by the mass analyzer. Additional UH^+ is actually being formed, and the increased ratio of UH^+ to U^+ is not caused by tailing of the $^{238}\text{U}^+$ peak.

The SbH^+/Sb^+ signal ratio increased from almost zero to approximately 6×10^{-4} at 80 mL of H_2/min . This measured ratio is one full order of magnitude smaller than the UH^+/U^+ ratio. We suspect the dissociation energy of UH^+ (3.3 ± 0.5 eV) [9] is higher than that for SbH^+ , whose value is not known.

Increasing the H_2 gas flow from 80 mL/min to 90 mL/min provides interesting insight into the mechanism behind MH^+ ion formation in the CRI collision region. At a flow rate of 90 mL/min, the UH^+/U^+ and SbH^+/Sb^+ ratios actually decrease in comparison to the values at 80 mL/min. The new ratios are 4×10^{-3} for UH^+/U^+ and 4×10^{-4} for SbH^+/Sb^+ . This decrease in measured SbH^+ and UH^+ ions is, again, likely caused by collision induced ion loss. The MH^+ ions are still being formed through reactions of the monatomic ions with H_2 ; however, additional collisions are reducing the ion kinetic energies and increasing ion scatter within the CRI collision region. It is also possible that the MH^+ ions are slightly larger than the monatomic ions which would lead to the MH^+ ions undergoing more collisions than the monatomic ions. Unfortunately, the collision cross-sections of MH^+ ions are not widely known either. Therefore, it cannot be determined if size is an important factor in the decreasing MH^+ ion ratios based on these data alone.

Since MH^+ ion levels increase noticeably at 80 mL/min and then decrease at 90 mL/min, the MH^+ levels were measured at various H_2 flow rates from 0 mL/min to 100 mL/min at an interval of 10 mL/min (Figure 3). The SbH^+/Sb^+ ratio reaches its maximum value at approximately 20 mL/min, while UH^+/U^+ reaches its maximum at 30 mL/min. At higher flow rates, the MH^+/M^+ signal ratios decrease. Although the MH^+ ion levels increase significantly with the initial flow rates of H_2 added, the relative amounts of MH^+ ions remaining in the typical CRI operating range are rather small, although much higher than from the ICP alone. As stated above, the higher H_2 flow rates are generally used analytically.

Contribution of the Ion Optics to MH^+ Ion Levels

The unique arrangement of the ion optics in the Aurora Elite contributes largely to the shape and path of the resulting ion beam from the plasma and the CRI collision region. Following the CRI collision region, extraction lenses focus the ion beam toward the ion mirror. The ion mirror deflects the ion beam 90° off axis towards the detector. This 90° deflection prevents photons and neutral atoms from interfering with ion detection.

To determine if the ion optics arrangement has an effect on the level of MH^+ ions reaching the detector, the ion optics were optimized selectively for U^+ and UH^+ ions. For comparison, the mirror lens' components (left, right, and top) were also optimized separately from the other ion optics to determine if the 90° path deflection has a significant effect on the level of U^+ and UH^+ ions present as well. For this experiment, the H_2 flow rate through the skimmer cone was set to 85 mL/min to remain representative of the typical H_2 flow rate range used for analysis.

As a reference, the UH^+/U^+ signal ratios were re-measured to be $\sim 3.5 \times 10^{-5}$ without H_2 and $\sim 4 \times 10^{-3}$ at 85 mL H_2/min . These values were consistent with those measured in the previous flow rate experiments. The remaining measurements for these ion optics experiments are presented in Table 1. These results show that the ion optics, specifically the mirror lens components, have a large role in MH^+ transmission. Optimizing the mirror lens only (D in Table 1) accounts for 90% of the maximum observable UH^+ ions (C in Table 1).

In most applications of ICP-MS, MH^+ ions would not be the main focus of analysis and therefore, the instrument would not be optimized deliberately for a MH^+ ion. In most cases, the optimization process is done for the highest possible sensitivity of all monatomic ions with low levels of possible interfering polyatomic ions. When optimized for these conditions, the MH^+ ions are much less abundant than those found in this specific experiment. However, this experiment does show that more MH^+ ions are present in the ion beam than are actually transmitted into the mass analyzer by the ion optics of the Aurora Elite. This reduces the level of MH^+ ions to some extent.

Kinetic Energy Comparison of MH^+ Ions and M^+ Ions

As mentioned previously, the MH^+ ion signals are suppressed as the H_2 flow rate is increased after approximately 30 mL/min through the CRI skimmer cone. Although H_2 is most often used as a reactive gas in the CRI, it is likely that kinetic energy discrimination (KED) is also occurring due to an increased number of collisions as the H_2 flow rate is increased. To confirm this, kinetic energy measurements were taken via stopping curves for the MH^+ ions and their parent monatomic ions. Stopping curves are created by measuring the ion signal with increasing positive quadrupole bias voltages. The maximum kinetic energy of an ion is

determined to be the quadrupole bias voltage at which the ion signal is attenuated to 1% of the maximum ion signal.

A typical set of stopping curves is shown in Figure 4. These stopping curves show the measured ion signals for $^{235}\text{U}^+$, $^{238}\text{U}^+$, and $^{238}\text{U}^1\text{H}^+$ versus the quadrupole DC bias voltage at H_2 flow rates of 0 mL/min, 30 mL/min, and 85 mL/min. The stopping curve for $^{235}\text{U}^1\text{H}^+$ could not be measured due to the signal intensity being below the instrumental limit of detection for m/z 236.

In these stopping curves, it can be seen that the maximum kinetic energy for the UH^+ ions is substantially less than that of the U^+ ions at each H_2 flow rate. The approximate maximum kinetic energies from these stopping curves are shown in Table 1. At H_2 flow rates of 30 mL/min and 85 mL/min, UH^+ consistently has a kinetic energy of 0.7 eV to 0.8 eV lower than U^+ . Although an exact numerical value of the maximum kinetic energy for UH^+ at a H_2 flow rate of 0 mL/min could not be determined due to signal instability, an estimated value is shown in Table 2. It can clearly be seen that the maximum kinetic energy is still less than that of U^+ .

The approximate kinetic energies for SbH^+ and Sb^+ are also shown in Table 2. Like UH^+ and U^+ , SbH^+ consistently has a lower kinetic energy than Sb^+ ; however, the energy difference is larger between SbH^+ and Sb^+ than for UH^+ and U^+ .

If the MH^+ ions were only produced within the plasma, they would have a similar maximum kinetic energy to their parent monatomic ions based, on their similarity in m/z . For comparison, stopping curves were measured for ArH^+ ions which are normally present in the background spectrum and are known to form naturally in the plasma or early in the supersonic expansion [10, 11]. ArH^+ at m/z 37 is highly abundant and was found to have a very similar

maximum kinetic energy to Ar^+ at m/z 38 (Table 2). The maximum kinetic energies for Ar^+ ions at m/z 36 and 40, as well as the ArH^+ ions at m/z 39 and 41, could not be measured at the same time as m/z 37 and 38 due to detector limitations.

Taking this into consideration, estimated values in Table 2 clearly show that UH^+ has a maximum kinetic energy that is much lower than that of U^+ at all H_2 flow rates, even with no added H_2 . This difference indicates that, when H_2 is added through the CRI, UH^+ ions are not formed solely in the plasma and are mainly formed in the region in which the CRI collisions are taking place. UH^+ ions have the characteristic kinetic energy of the expansion from the skimmer tip [12] caused by the deliberate shockwave made with H_2 ; whereas, U^+ ions have a kinetic energy characteristic of ions present outside the sampler in the ICP. Ions formed in CRI, i.e. the skimmer expansion, have different kinetic energies than those that come from the plasma.

Conclusion

MH^+ ions, with the exception of ArH^+ , are not abundantly produced in the plasma in ICP-MS. Depending on the specific application, the levels of MH^+ ions present from the plasma alone would not have a large impact on the results of the analysis. However, the addition of H_2 gas through the CRI skimmer cone into the dense plasma expansion makes the presence of MH^+ ions more of a concern.

Adding H_2 as a reaction gas through the CRI introduces the possible formation of more MH^+ ions than are initially present from the plasma alone. In this study, it was found that some new MH^+ ions, specifically UH^+ and SbH^+ , are formed as H_2 is added through the CRI skimmer. At low H_2 flow rates, UH^+ and SbH^+ ion levels are significantly presents, approaching 1% (MH^+/M^+) in some cases. However, as the H_2 flow rate is increased, the levels of MH^+ ions

decrease due to reduction in kinetic energy and collision induced ion losses. In the normal CRI operating range for H₂, the MH⁺ ion levels are approaching insignificant levels, but they are still much higher than those originally present without added H₂.

In terms of background ions, it was found that no notable new background ions were formed due to the addition of H₂ gas, even at low flow rates. Only ions that were originally present from the plasma as a result of the plasma gas reacting with the blank solvent solution increased initially in intensity. Like the MH⁺ ions, these ions too were removed via collisions with increasing H₂ flow rate and are suppressed greatly in the normal CRI operating range for H₂. Only H₃O⁺ and H₃⁺ remain at significant levels in this range, but these ions are expected and are likely product ions of multiple sequential reactions.

Lastly, based on maximum kinetic energy measurements, it was found that MH⁺ ions have maximum kinetic energies that are substantially lower than those of their parent monatomic ions initially formed in the plasma. These lower kinetic energies indicate that the MH⁺ ions are, in fact, formed in a different location than the ICP, most likely the CRI collision region. This conclusion was confirmed by comparing the differences in kinetic energies to the maximum kinetic energies of Ar⁺ and ArH⁺ which are known to be highly abundant in the plasma.

Overall, this study indicates that MH⁺ ions may be more of a concern than originally anticipated when using CRI technology to implement H₂ as a reaction gas. This would most likely be applicable in scenarios where highly precise measurements of sequential elements or isotopes are necessary. Further research may be necessary to account for MH⁺ ion in these scenarios. Additional MH⁺ ions may also be more abundant in other various ICP-MS instruments than commonly thought; however, further research is necessary to study this possibility.

Acknowledgements

This research was performed in the Ames Laboratory. The authors would like to thank Analytik Jena for providing the Aurora Elite instrumentation and Andrew Toms for providing suggestions and information about the instrumentation.

References

- [1] D. J. Douglas, J. B. French, Collisional focusing effects in radio frequency quadrupoles, *J. Am. Soc. Mass. Spectrom.* 3 (1992) 398-408.
- [2] X. Wang, I. Kalinitchenko, Fundamental and practical aspects of the CRI technology for ICP-MS, (2007).
- [3] J. T. Larsen, I. Kalinitchenko, Eliminating ICP-MS Interferences with kinetic energy discrimination CRI and 3D ion mirror, 22 January 2014. [Online]. Available: https://www.bruker.com/fileadmin/user_upload/8-PDF-Docs/Separations_MassSpectrometry/Literature/literature/Presentations/PWC14_JoernLarsenCRI.pdf. [Accessed 9 April 2015].
- [4] C. D. Pereira, E. E. Garcia, F. V. Silva, A. A. Nogueira, J. A. Nobrega, Behaviour of arsenic and selenium in an ICP-QMS with collision and reaction interface, *J. Anal. At. Spectrom.* 25 (2010) 1763-1768.
- [5] R. F. Salazar, M. B. Guerra, E. R. Periera-Filho, J. A. Nobrega, Performance evaluation of collision-reaction interface and internal standardization in quadrupole ICP-MS measurements, *Talanta* 86 (2011) 241-247.
- [6] S. D. Tanner, V. I. Baranov, D. R. Bandura, Reaction cells and collision cells for ICP-MS: a tutorial review, *Spectrochim. Acta Part B* 57 (2002) 1361-1452.
- [7] R. N. Taylor, T. Warneke, J. A. Milton, I. W. Croudace, P. E. Warwick, R. W. Nexbitt, Plutonium isotope ratio analysis in femtogram to nanogram levels by multicollector ICP-MS, *J. Anal. At. Spectrom.* 16 (2001). 279-284.
- [8] M. G. Minnich, R. S. Houk, Comparison of cryogenic and membrane desolvation for attenuation of oxide, hydride, and hydroxide ion and ions containing chlorine in inductively coupled plasma mass spectrometry, *J. Anal. At. Spectrom.* 13 (1998) 167-174.

- [9] P. E. Moreland, JR., D. J. Rokop, C. M. Stevens, Mass-Spectrometric Observations of Uranium and Plutonium Monohydrides Formed by Ion-Molecule Reaction, *Int. J. Mass Spectrom. Ion Phys.* 5 (1970) 127-136.
- [10] D. J. Douglas, J. B. French, Gas dynamics of the inductively coupled plasma mass spectrometry interface, *J. Anal. Atomic Spectrom.* 3 (1988) 743-747.
- [11] N. S. Nonose, N. Matsuda, N. Fudagawa, M. Kubota, Some characteristics of polyatomic ion spectra in inductively coupled plasma mass spectrometry, *Spectrochim. Acta Part B* 49 (1994) 955-974.
- [12] N. Taylor, P. B. Farnsworth, Experimental characterization of the effect of skimmer cone design on shock formation and ion transmission efficiency in the vacuum interface of an inductively coupled plasma mass spectrometer, *Spectrochim. Acta Part B* 69 (2012) 2-8.

Table 1: UH^+/U^+ Signal Ratio at various ion optic optimization parameters. (A) Normal sensitivity ion optics optimization parameters optimized for the entire mass range without H_2 flow added, (B) with H_2 flow of 85 mL/min, (C) all ion optics re-optimized specifically for UH^+ and U^+ ion signals with H_2 flow of 85 mL/min, (D) only mirror lens parameters optimized for UH^+ and U^+ ion signals with H_2 flow of 85 mL/min.

Ion Optics Conditions	UH^+/U^+ Signal Ratio
A	2.3×10^{-5}
B	4×10^{-3}
C	1×10^{-2}
D	9×10^{-3}

Table 2: Approximate maximum kinetic energy of measured MH^+ ions and their corresponding parent ions.

H₂ CRI Flow	Max Kinetic Energy (eV)		
	$^{235}\text{U}^+$	$^{238}\text{U}^+$	$^{238}\text{U}^1\text{H}^+$
0 mL/min	3.67	3.71	(2.68)*
30 mL/min	3.09	3.14	2.33
85 mL/min	2.29	2.33	1.60

H₂ CRI Flow	Max Kinetic Energy (eV)			
	$^{121}\text{Sb}^+$	$^{121}\text{Sb}^1\text{H}^+$	$^{123}\text{Sb}^+$	$^{123}\text{Sb}^1\text{H}^+$
0 mL/min	2.96	--*	2.98	--*
30 mL/min	2.17	0.87	2.20	0.91
85 mL/min	0.90	-0.08**	0.92	-0.03**

H₂ CRI Flow	Max Kinetic Energy (eV)	
	$^{36}\text{Ar}^1\text{H}^+$	$^{38}\text{Ar}^+$
0 mL/min	1.48	1.47

* Insufficient signal present for accurate measurement

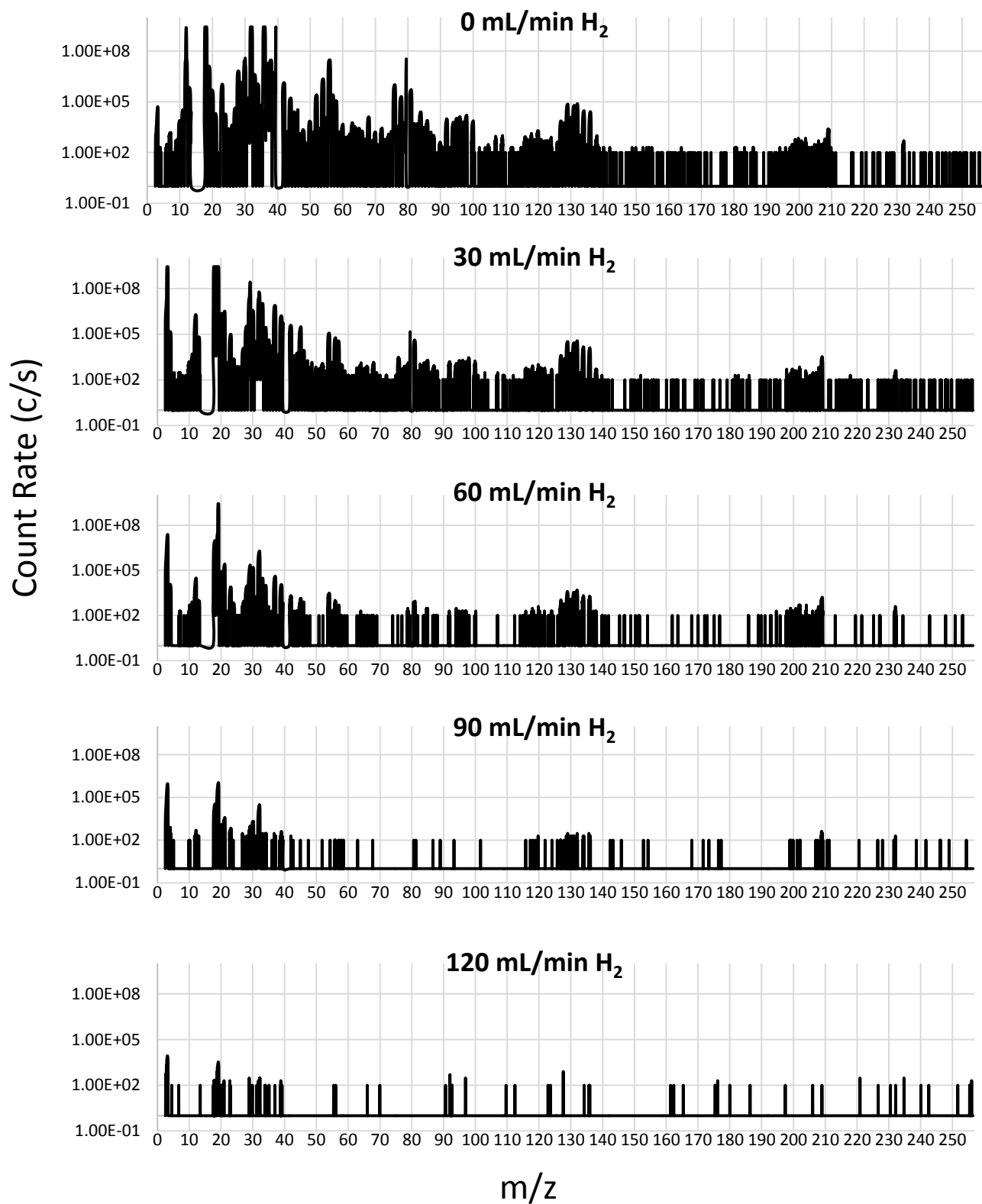


Figure 1: Background spectra at various H_2 flow rates. There is a noticeable increase in H_3^+ , H_2O^+ , H_3O^+ , HO_2^+ , ArH^+ , ArH_2^+ , and ArH_3^+ signals up to 30 mL/min H_2 .

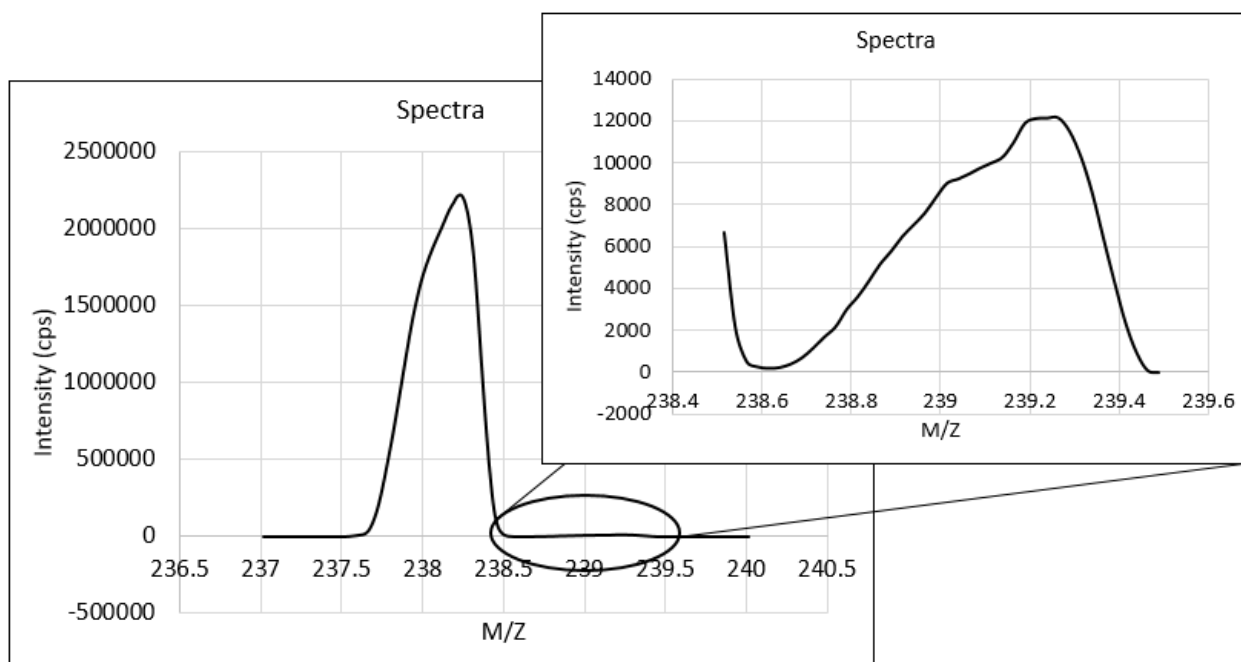


Figure 2: Spectra of U^+ and UH^+ at a H_2 flow rate of 80 mL/min. A distinct valley is seen between the two peaks which signifies UH^+ is actually being resolved from U^+ .

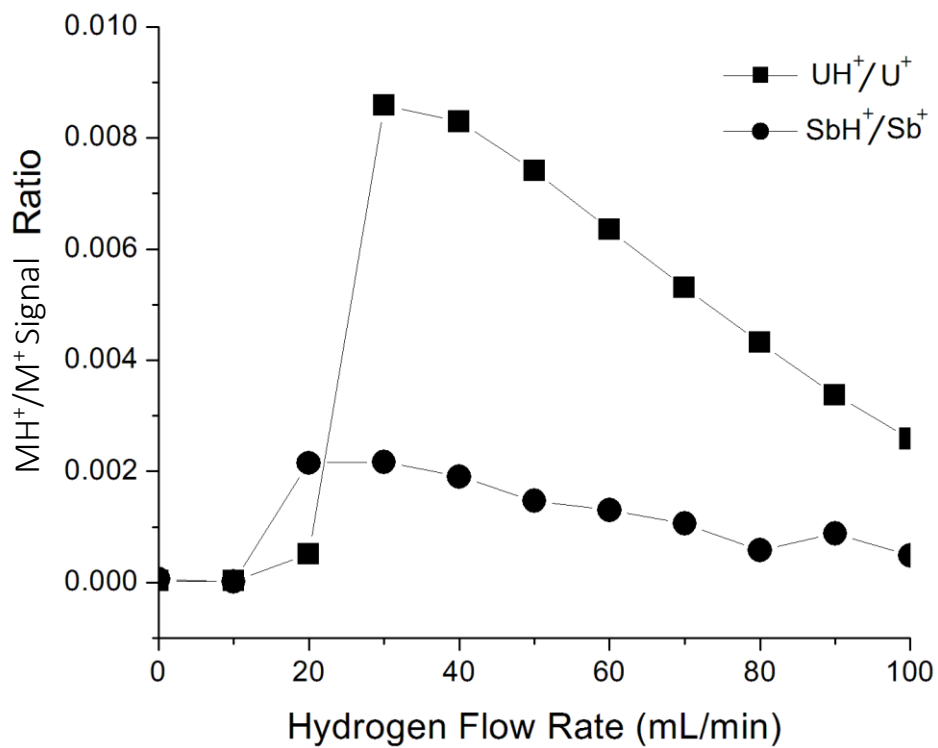


Figure 3: UH⁺/U⁺ and SbH⁺/Sb⁺ ratios at flow rates of H₂ ranging from 0 mL/min to 100 mL/min.

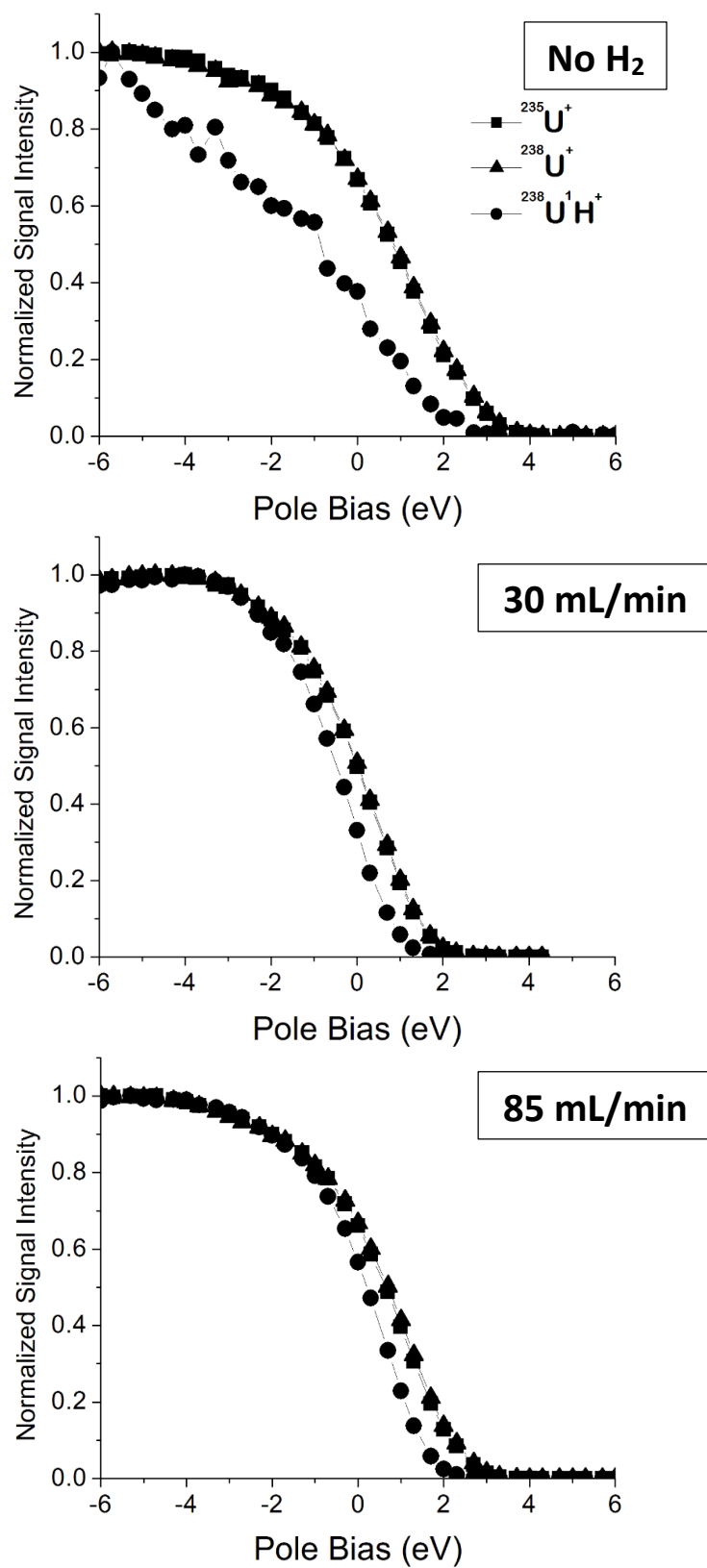


Figure 4: Normalized ion signal intensity versus quadrupole bias.

CHAPTER 5: GENERAL CONCLUSIONS

The composition of the plasma and the ion beam are very important in ICP-MS. However, all aspects of the way ions are made and transported in ICP-MS are not fully understood. This dissertation delves into several aspects of analyte ionization and polyatomic ion mitigation to better understand ion formation, ion transport, and reactions taking place as the analyte ions are transported through the ICP-MS.

Chapter 2 shows that small changes in plasma temperature can make a large difference in the efficiency of ionization in the ICP. The ionization efficiency of analyte ions in an ICP is a determining factor in the efficiency and applicability of ICP-MS for elemental analysis. Chapter 2 also discusses the abundance of M^{2+} ions and the ionization and dissociation of MO^+ ions, which can interfere with analyte ions at the same nominal m/z values. It is important to maintain a plasma temperature in ICP-MS to produce maximum amounts of M^+ ions while maintaining minimum amounts of MO^+ and M^{2+} ions for accurate elemental analyses.

Chapter 3 discusses the collision reaction interface (CRI). CRI is a commercially available collision technology implemented for the removal of polyatomic ion interferences from the ion beam via a collision or reaction gas. The CRI is not as thoroughly characterized as the more widely used multipole collision cell. Approximate characteristics of the CRI were determined based on calculated collision cross sections established using a collision cell. If 95% of the collisions in the CRI are assumed to occur within 2 mm of the CRI skimmer tip, a gas density of less than 10^{16} cm^{-3} within the CRI region is conducive to allowing adequate collisions

to occur for interference removal, while allowing an adequate number of ions to transverse into the mass spectrometer for detection.

Finally, Chapter 4 describes the formation of metal monohydride (MH^+) ions in the CRI collision region with the addition of hydrogen gas. Although the CRI is intended to remove polyatomic ion interferences, it was found that some new MH^+ ions, specifically UH^+ and SbH^+ , are formed as H_2 is added through the CRI skimmer. As the H_2 flow rate is increased, the levels of MH^+ ions decrease due to reduction in ion kinetic energy and collision induced ion losses. This study indicates that MH^+ ions may be more of a concern than originally anticipated when using CRI technology with H_2 as a reaction gas.

Overall, these chapters demonstrate that small changes to the characteristics of the plasma and/or the ion beam may have a large impact on the results of an analysis. Improved knowledge of the plasma specifically plasma temperature and composition, collision technologies, and the behavior of collision and/or reaction gases in ICP-MS would allow for improvements in areas of application in which ICP-MS is commonly implemented.

APPENDIX A. GIANT MAGNETIC ANISOTROPY AND TUNNELLING

OF THE MAGNETIZATION IN $\text{Li}_2(\text{Li}_{1-x}\text{Fe}_x)\text{N}$

A. Jesche¹, R.W. McCallum^{1,2}, S. Timmaiah¹, J.L. Jacobs^{1,3}, V. Taufour⁴, A. Kreyssig^{1,4},
R.S. Houk^{1,3}, S.L. Bud'ko^{1,4} & P.C. Canfield^{1,4}

¹*The Ames Laboratory, Iowa State University, Ames, Iowa, USA*

²*Department of Materials Science and Engineering, Iowa State University, Ames, Iowa, USA*

³*Department of Chemistry, Iowa State University, Ames, Iowa, USA*

⁴*Department of Physics and Astronomy, Iowa State University, Ames, Iowa, USA*

A paper published in Nature Communications.

Abstract

Large magnetic anisotropy and coercivity are key properties of functional magnetic materials and are generally associated with rare earth elements. Here we show an extreme, uniaxial magnetic anisotropy and the emergence of magnetic hysteresis in $\text{Li}_2(\text{Li}_{1-x}\text{Fe}_x)\text{N}$. An extrapolated, magnetic anisotropy field of 220 Tesla and a coercivity field of over 11 Tesla at 2 Kelvin outperform all known hard-ferromagnets and single-molecule magnets (SMMs). Steps in the hysteresis loops and relaxation phenomena in striking similarity to SMMs are particularly pronounced for $x \ll 1$ and indicate the presence of nano-scale magnetic centres. Quantum tunnelling, in form of temperature-independent relaxation and coercivity, deviation from Arrhenius behaviour and blocking of the relaxation, dominates the magnetic properties up to 10 Kelvin.

The simple crystal structure, the availability of large single crystals, and the ability to vary the Fe concentration make $\text{Li}_2(\text{Li}_{1-x}\text{Fe}_x)\text{N}$ an ideal model system to study macroscopic quantum effects at elevated temperatures and also a basis for novel functional magnetic materials.

Introduction

Controlling individual spins on an atomic level is one of the major goals of solid state physics and chemistry. To this effect, single-molecule magnets (SMMs) ^[1] have brought significant insight ranging from fundamental quantum effects like tunnelling of the magnetization ^[2] and quantum decoherence ^[3] to possible applications in quantum computing ^[4] and high density data storage ^[5]. Their basic magnetic units are coupled spins of a few magnetic atoms which are embedded in and separated by complex organic structures. Whereas these are small magnetic units, they are still finite in extent and need to carefully balance coupling between magnetic atoms and isolation of one molecule from the next. Dimers of transition metals, as the small-size end-point of SMMs, have been theoretically proposed to be promising candidates for novel information storage devices ^[6]. An alternative approach for the design of magnetic materials based on a few or even single atoms as magnetic units are ad-atoms on metallic surfaces ^[7, 8]. The key property among these actually very different examples, and of any nano-scale magnetic system, is a large magnetic anisotropy energy.

Basic magnetic units of SMMs are transition metal ion clusters ^[9], lanthanide ion clusters ^[10, 11], or mixed clusters of both ^[12]. Even mononuclear complexes based on a single lanthanide ion have been realized ^[13, 14]. The lanthanide based systems are promising due to their large single ion anisotropy ^[15, 16] which often leads to large magnetic anisotropy energies. In contrast, single transition metal ions are seldom considered as suitable candidates and the number of reported

attempts to use them as mononuclear magnetic units is limited^[17, 18, 19]. The main reason is the widely known paradigm of 'orbital quenching'. This suppression of the orbital contribution to the magnetic moment by the crystal electric field leads to a comparatively small anisotropy energy (neglecting spin-orbit coupling, a pure spin contribution is by default isotropic). The absence of an orbital contribution is reflected, e.g., in the largely isotropic magnetization of the elemental ferromagnets Fe, Co, and Ni^[20, 21]. However, Klatyk *et al.*^[22] have suggested that a rare interplay of crystal electric field effects and spin-orbit coupling causes a large orbital contribution to the magnetic moment of Fe in polycrystalline $\text{Li}_2(\text{Li}_{1-x}\text{Fe}_x)\text{N}$. Based on the strong increase of the magnetization upon cooling^[22] and on Mössbauer spectroscopy^[22, 23] a ferromagnetic ordering with $T_C \approx 65$ K was inferred for $x=0.21$ and, furthermore, huge hyperfine fields were found. The orbital contribution to the magnetic moment of Fe as well as the large hyperfine fields were theoretically described within the framework of local density approximation (LDA) calculations^[22, 24]. Furthermore, a large magnetic anisotropy has been theoretically proposed^[22, 24].

Here we show the experimental verification of the large anisotropy by magnetization measurements on single crystals and reveal a huge magnetic hysteresis as the key property of functional magnetic materials. More importantly, we have discovered that this highly anisotropic transition metal system manifests strong indications of a macroscopic quantum tunnelling of the magnetization in the form of pronounced steps in the magnetization loops and a temperature-independent relaxation. Tunnelling of the magnetization explicitly refers to the macroscopic tunnelling of the total magnetization and not to microscopic tunnelling events influencing the domain-wall movement in ferromagnets^[25]. The Li_3N host provides an extremely anisotropic ligand field for the Fe atoms as well as an insulating environment in analogy to the 'organic framework' of SMMs. There are no indications for meso- or macroscopic phase separation

(Supplementary Note 1). Although we cannot completely rule out cluster formation (e.g. dimers or trimers of Fe on adjacent Li sites) the preponderance of the data support a single iron atom as mononuclear magnetic centre which is, furthermore, the simplest model and based on the fewest assumptions. The phenomenological similarities to SMMs indicate that the spontaneous magnetization and hysteresis are primarily caused by the extreme magnetic anisotropy and not by collective ordering phenomena. In accordance with earlier work on mononuclear systems, $\text{Li}_2(\text{Li}_{1-x}\text{Fe}_x)\text{N}$ might be considered as 'atomic magnet' [26] or 'single-ionic SMM' [15]. The magnetic anisotropy, coercivity and energy barrier for spin-inversion found in $\text{Li}_2(\text{Li}_{1-x}\text{Fe}_x)\text{N}$ are roughly one order of magnitude larger than in typical SMMs. Magnetic hysteresis exists up to comparatively high temperatures of $T \gtrsim 16$ K for $x \leq 1$ and is further enhanced up to $T \gtrsim 50$ K for the largest Fe concentration of $x=0.28$.

Results

Basic properties of $\text{Li}_2(\text{Li}_{1-x}\text{Fe}_x)\text{N}$

We grew $\text{Li}_2(\text{Li}_{1-x}\text{Fe}_x)\text{N}$ single crystals of several millimetre size (Figs. 1a, b) and Fe concentrations ranging over three orders of magnitude $x=0.00028$ to 0.28 by using a Li-flux method to create a rare, nitrogen-bearing metallic solution. $\text{Li}_2(\text{Li}_{1-x}\text{Fe}_x)\text{N}$ crystallizes in a hexagonal lattice, space group $P6/mmm$, with a rather simple unit cell (Fig. 1c) and lattice parameters of $a=3.652(8)$ Å and $c=3.870(10)$ Å for $x=0$. Fe-substitution causes an increase of a but a decrease of c by 1.1 % and 1.5 %, respectively, for $x=0.28$ with intermediate concentrations showing a linear dependence on x following Vegards law (Supplementary Fig. 1). As indicated by the notation of the chemical formula, the substituted Fe-atoms occupy only the Li-1b Wyckoff

position which is sandwiched between Li_2N layers. The iron concentrations, x , were measured by inductively coupled plasma mass spectrometry which enables a quantitative analysis on a parts per billion level (Fig. 1d). Structural parameters and selected x values were determined by single crystal and powder X-ray diffraction and are in good agreement with earlier results [22, 27, 28, 29]. To support our findings we present details of crystal growth procedure and chemical analysis (see Methods), as well as X-ray powder diffraction (Supplementary Fig. 2, Supplementary Note 2) and X-ray single crystal diffraction (Supplementary Tables 1 and 2, Supplementary Note 3).

The samples are air sensitive in powder form but visual inspection and magnetic measurements revealed no significant decay of larger single crystals on a timescale of hours. As stated in Ref. [30], this is probably "due, somewhat perversely, to the formation of a surface film of predominantly LiOH ". Covering the samples with a thin layer of Apiezon M grease further protects the sample and no degradation was observed over a period of several weeks. Single crystals which had been exposed to air for a few minutes and were stored afterwards in an inert atmosphere (argon or nitrogen) did not change their magnetic properties on a time scale of three months. The electrical resistivity at room temperature is estimated to be $\rho > 10^5 \Omega \text{cm}$ for all studied x .

Magnetization

Extreme magnetic anisotropy of $\text{Li}_2(\text{Li}_{1-x}\text{Fe}_x)\text{N}$ is conspicuously evident in the magnetization measurements shown in Figs. 2a,b for two very different Fe concentrations of $x = 0.0032$ and $x = 0.28$. For magnetic field applied along the c -axis, $H \parallel c$, the magnetization is constant for $\mu_0 H > 1 \text{ T}$ (starting from the field cooled state) with a large saturated moment of

$\mu_{\text{sat}}^{\parallel c} \approx 5 \mu_{\text{B}}$ per Fe atom. In contrast, the magnetization for $H \perp c$ is smaller and slowly increases

with field. A linear extrapolation to higher magnetic fields yields huge anisotropy fields of $\mu_0 H_{\text{ani}} \approx 88 \text{ T}$ ($x=0.0032$) and $\mu_0 H_{\text{ani}} \approx 220 \text{ T}$ ($x=0.28$) defined as the field strength where both magnetization curves intersect. The larger magnetic anisotropy field for $x=0.28$ is reflected in the larger coercivity field of $\mu_0 H_c = 11.6 \text{ T}$ found for this concentration. The inverse magnetic susceptibility, $\chi^{-1} = H/M$, roughly follows a Curie-Weiss behaviour for $T \gtrsim 150 \text{ K}$ and is strongly anisotropic over the whole investigated temperature range (Fig. 2c). The corresponding Weiss temperatures are $\Theta_{\text{W}}^{\perp c} = -80(10) \text{ K}$ and $\Theta_{\text{W}}^{\parallel c} = 100(10) \text{ K}$. In the following we discuss only measurements with $H \parallel c$ since available laboratory fields do not allow saturation of the magnetization for $H \perp c$. Both $\mu_{\text{sat}}^{\parallel c}$ and $\mu_{\text{eff}}^{\parallel c}$ were found to be largely independent of the Fe concentration but for a small tendency to decrease with increasing x (Fig. 1d, see Supplementary Note 4 for error analysis). The average values are $\mu_{\text{sat}}^{\parallel c} = 4.8(4) \mu_{\text{B}}$ and $\mu_{\text{eff}}^{\parallel c} = 6.5(4) \mu_{\text{B}}$ in good agreement with theoretical calculations for $x=0.17$ [24]. Furthermore, the obtained effective moment is surprisingly close to the $\mu_{\text{eff}} = 6.6 \mu_{\text{B}}$ expectation value of a fully spin-orbit coupled state (Hund's rule coupling) when assuming a $3d^7$ configuration for the proposed Fe^{+1} state (for a discussion of this unusual valence see [22, 24]).

In the following we focus on experimental results on the very dilute case which approaches an ideally non-interacting system of single magnetic atoms. The temperature-dependence of the M - H loops for $x=0.0032$ with a high density of data points are shown in Fig. 3a. Three main observations can be made:

First, the magnetization curve is essentially temperature-independent for $T < 10 \text{ K}$ with $\mu_0 H_c = 3.4 \text{ T}$ which indicates the irrelevance of thermal excitations. In contrast, H_c changes

dramatically between 10 and 16 K indicating a distinct separation into a low- and a high-temperature behaviour.

Second, there are pronounced steps in the magnetization. An enlarged view on part of the M - H loop, Fig. 3b, reveals steps in M at $\mu_0 H = 0, \pm 0.15$, and ± 0.55 T. Another, smaller but well defined, step occurs at $\mu_0 H = \pm 5$ T. The step-sizes are larger when H approaches zero and decrease with increasing temperature in contrast to the step-positions which are independent of temperature. No steps could be resolved for $T \gtrsim 16$ K. The steps are strongly suppressed with increasing x (Supplementary Fig. 3), most likely caused by an increasing Fe-Fe interaction and vanish for $x = 0.28$ (Fig. 2b).

Third, the M - H loop at $T = 2$ K starts from a saturated state where the Fe-magnetic moments appear to be aligned parallel to the field, $\mu \parallel H$ with $H \parallel c$. The first step occurs already in the first quadrant (upper right corner) when H approaches zero from positive values. Similar behaviour was observed in lanthanide-based mononuclear SMMs ^[25] whereas SMMs based on clusters show no corresponding steps in the first quadrant ^[1]. A decrease of the magnetization in the first quadrant, where H is still parallel to the initial magnetization, is incompatible with the c -axis being the easy axis. Rather, the moment seems to be tilted away from the c -axis and the reduced magnetization is the projection of the moment along the c -axis (see Discussion). Notice that an axis canted away from the c -axis would be 12- or 24-fold degenerate (depending on whether it is oriented along a high-symmetry direction like $h0l$ or not). Accordingly, the magnetization perpendicular to the c axis ($H \perp c, M \perp c$) is still small in zero field because the perpendicular components of the tilted moments cancel out.

In contrast to a common ferromagnet, the M - H loops not only depend on temperature but do also show a pronounced, characteristic dependence on the sweep-rate of the applied magnetic

field. Figures 3c,d show M - H loops at $T=2$ K for sweep rates between 15 mT/s and 1.1 mT/s, corresponding to a total time between 40 minutes and 9 hours and 10 minutes, respectively, for the whole loop. The step-sizes at $\mu_0 H = \pm 0.15$ and ± 0.55 T hardly depend on the sweep-rate, whereas the step-size at $H=0$ does. A low sweep-rate dependence of the step-size is in accordance with a large tunnelling gap, which is much smaller than the energy gap ^[31] (for a convenient description of the relation between sweep rate and tunnelling gap see ^[32] and references therein). Although the field values for the steps do not change significantly with sweep-rate, the width of the whole hysteresis loop (and therefore H_c) does (Fig. 3c). Pronounced sweep-rate dependence of H_c is observed also for higher Fe concentrations - see Supplementary Fig. 3. The observation of smaller H_c values in slower measurements clearly reveals the dynamic nature of the hysteresis. This observation motivated a detailed study of the time dependence of the magnetization, which is presented in the following section.

Relaxation

When a magnetic moment is subject to a change in the applied magnetic field it will take a finite relaxation time to reach the equilibrium state (see e.g. Ref. ^[33]). The sweep-rate dependence of the hysteresis loops indicates a time-scale of several hours for the relaxation in $\text{Li}_2(\text{Li}_{1-x}\text{Fe}_x)\text{N}$. This is so slow that the change of the magnetization with time, $M(t)$, during the relaxation process can be directly measured with standard laboratory magnetometers. Three procedures are schematically shown in the left panels of Fig. 4 (see Supplementary Note 4 for detailed measurement protocols). The corresponding experimental data are in the panels to the right:

Figures 4a-c show the relaxation after switching on the field. $M(t)$ increases rapidly for $T=16$ K and the magnetization is constant after $t\sim 500$ s. The relaxation is becoming markedly slower as the measurement temperature is reduced to $T=10$ K, and $M(t)$ keeps increasing up to the maximum measurement time. However, below 10 K, $M(t)$ is only weakly temperature dependent in $\mu_0=1$ T and essentially temperature-independent in $\mu_0H=2$ T. *This temperature-independence is inconsistent with a thermally activated relaxation process.* The inset of Fig. 4c shows an enlarged region of the plot. No correlation of relaxation with temperature is apparent. The relaxation for $T>16$ K is too fast to be measured directly and $M(t)$ is immediately constant once the field is stabilized. The relaxation process shows clear anomalies at the resonance fields (step-positions in M - H loops) as shown in Supplementary Fig. 4.

Figures 4d-f show the relaxation after switching off the field. The relaxation is fast for $T=16$ K but suppressed for lower temperatures. However, the decrease is non-uniform with temperature and markedly smaller at the lowest temperatures. $M(t)$ can be fitted to a stretched exponential

$$M(t)=M_0 \exp[-(t/\tau)^\beta], \quad (1)$$

with $M_0=M(t=0)$ and τ is the relaxation time (for details regarding the exponent β see Supplementary Fig. 5 and Supplementary Note 4). For $T>16$ K, τ is too small to be measured directly but can be determined from the out-of-phase part of the ac-magnetic susceptibility, $\chi''(T)$. The inset in Fig. 4f shows maxima in $\chi''(T)$ at temperatures T_{\max} which increase with the excitation frequency f . The maximum in $\chi''(T)$ corresponds to a maximum in the energy absorption of the ac-field by the sample and shows that the relaxation time equals the time scale of the experiment, i.e., $\tau=1/f$ at $T=T_{\max}$. The values obtained for τ are shown in Fig. 4f in form of

an Arrhenius-plot. For $T \geq 16$ K, τ follows a linear (Arrhenius-) behaviour with good agreement between directly and indirectly measured values. A fit of τ to a thermally activated law ($\tau = \tau_0 \exp[\Delta E/k_B T]$, dashed line) gives an energy barrier of $\Delta E/k_B = 430$ K and a pre-exponential factor $\tau_0 = 2.8 \cdot 10^{-10}$ s. For $T < 16$ K, τ deviates significantly from Arrhenius-behaviour and decreases much slower with decreasing temperature than expected for a thermally activated relaxation. A plateau, as shown in Fig. 4f, has been found in SMMs ^[2, 34] and is a clear fingerprint of quantum tunnelling.

Figures 4g-i show the relaxation in negative fields. This method is a variation of the previous one where the field is not simply switched off but ramped to a negative value opposite to the initial direction. As shown by the large magnetic hysteresis and the relaxation measurements above, the dominating energy scale of the system lies in the region of several Tesla acting on a few μ_B . Therefore, a magnetic field of a few milliTesla can, at most, merely change the energy level scheme. Furthermore, applying a negative field is expected to accelerate the decrease of $M(t)$. In contrast to both assumptions, small fields of $\mu_0 H = -1$ to -10 mT have a dramatic effect on the relaxation time and lead to an **increase** of τ by several orders of magnitude (black curves in Fig. 4h). In fact, the relaxation in $\mu_0 H = -10$ mT is becoming so slow that an accurate determination of τ is not possible within 4000 s but requires much longer measurement times (which is beyond the scope of this publication). The main effect of the small negative field is likely a destruction of the tunnelling condition by lifting the zero-field-degeneracy - resonant tunnelling of the magnetization occurs only between degenerate states ^[1].

In intermediate fields of $\mu_0 H = -50$ to -500 mT, the magnetization decreases rapidly until the applied field is stable (i.e. after 50 s for $\mu_0 H = -500$ mT), followed by a significantly slower relaxation. This indicates the presence of two time-scales for the relaxation, a fast one and a slow one. The slow relaxation can be associated with overcoming the large energy barrier in the a - b plane. However, the flipped moments are still not (anti-)parallel to the c -axis (Fig. 5a). The fast relaxation can be associated with the subsequent, full alignment of the magnetic moments along the c -axis by overcoming smaller, local maxima in the magnetic anisotropy energy (corresponding to the smaller steps in the M - H loop, see Fig. 5b). Only larger fields of $|\mu_0 H| > 1$ T cause a faster decrease of $M(t)$ when compared with zero field (Fig. 4i). A fast relaxation on the timescale of the experiment is reached in $\mu_0 H = -7$ T where $M(t)$ is saturated after $t \approx 2000$ s. Accordingly, the magnetization reaches saturation in a similar short time after applying a field of $\mu_0 H = 7$ T to an unmagnetized sample (analogue to Figs. 4a-c, not shown). It should be noted that the time-dependencies, as presented in this section, are not restricted to low Fe concentrations. Clear relaxation effects are observed through the whole concentration range with the tendency to slow down with increasing x .

Discussion

Our work shows that $\text{Li}_2(\text{Li}_{1-x}\text{Fe}_x)\text{N}$ not only has a clear and remarkable anisotropy, generally not associated with Fe moments, but also shows time-dependence more consistent with SMM systems. The strong correlation of relaxation time and coercivity field (Fig. 4f) indicates that the slow relaxation leads to magnetic hysteresis for $x \ll 1$, i.e., the dilute system is not a ferromagnet and hysteresis emerges from a slow decay of a polarized, paramagnetic state. Whether this holds true for the dense system ($x=0.28$), too, is not settled at this point - below

$T \approx 65$ K the ordering appears to be static on the timescale of Mössbauer spectroscopy [22, 23] (performed on polycrystalline material, $x=0.16$ and 0.21).

A possible schematic for the magnetic moment orientation and the magnetic anisotropy energy is depicted in Fig. 5. This model is purely based on the observed plateaus in the $M-H$ measurements and, beyond the extreme uniaxial symmetry of the iron environment, the origin of the magnetic anisotropy of $\text{Li}_2(\text{Li}_{1-x}\text{Fe}_x)\text{N}$ is still unclear. The anisotropy found in SMMs is based on the magnetic interactions within the transition metal cluster or on the single ion anisotropy of lanthanide ions (or on both). For the latter case, the anisotropy is caused by the crystal electric field which acts as perturbation on the multiplet ground state of the lanthanide ion which is determined by Hund's rule coupling. Neither of these conceptually simple scenarios is applicable for $\text{Li}_2(\text{Li}_{1-x}\text{Fe}_x)\text{N}$ since the Fe-atoms are too dilute to strongly interact with each other for $x \ll 1$ and the crystal electric field is too strong to be regarded as a small perturbation when compared with the spin orbit coupling. Instead we are left with the complex determination of the energy level scheme of the relevant Fe-3d electrons. Calculations based on LDA predict a counter-intuitive energy level scheme with the $3d_{z^2}$ level having the lowest energy followed by partially occupied $d_{x^2-y^2}$, d_{xy} levels [24]. A very similar level scheme was recently found for a mononuclear Fe-based SMM [19] sharing a similar structural motif as the Fe site in $\text{Li}_2(\text{Li}_{1-x}\text{Fe}_x)\text{N}$: a linear Fe^{+1} complex, which seems to be an essential ingredient for the emergence of unquenched orbital moments and large magnetic anisotropy.

Even though the exact microscopic origin of the energy barriers separating the magnetic states in $\text{Li}_2(\text{Li}_{1-x}\text{Fe}_x)\text{N}$ is not yet understood, we argue that quantum tunnelling has to be invoked to overcome them. From the Arrhenius-fit we find $\Delta/k_B=430$ K (Fig. 4f). Magnetization

measurements on single crystals allow for a second method to estimate the barrier-height: when H reaches the anisotropy field all moments are aligned along the field and the energy barrier is overcome. This gives rise to $\Delta E/k_B \approx \mu_0 H_{\text{ani}} \cdot \mu_{\text{sat}}/k_B \approx 88 \text{ T} \cdot 5 \mu_B/k_B = 300 \text{ K}$ in reasonable agreement with the above result. This value also agrees with the LDA based calculation of the anisotropy energy for $x=0.17$ ($\Delta/k_B=278 \text{ K}$)^[24]. Such a large barrier cannot be overcome thermally at $T=2 \text{ K}$ - an estimation of the relaxation time from thermally activated law and $\Delta/k_B=278 \text{ K}$ yields $\tau > 10^{43}$ years (give or take a millennium). Therefore, a tunnelling process is likely involved in the relaxation process where the applied magnetic field shifts the energy levels in and out of degeneracy in full analogy to SMMs. At this point it is not clear which levels of the single ion are brought in resonance by the applied magnetic field to explain the smaller steps in the M - H loops. Hyperfine interactions, as invoked for lanthanide based SMMs^[15] and $\text{LiY}_{0.998}\text{Ho}_{0.002}\text{F}_4$ (ref.^[35]), are likely too weak to account for steps at applied fields of $\mu_0 H=0.5 \text{ T}$ in particular since 98% of the Fe-atoms do not carry a nuclear moment.

Energy barriers of similar ($\Delta/k_B=300 \text{ K}$ ^[19, 36]) or even higher size ($\Delta/k_B=800 \text{ K}$ ^[37]) have been observed in mononuclear SMMs. However, the remanent magnetization for these samples is very small caused by short relaxation times at low temperatures, i.e., τ deviates from Arrhenius-behaviour with a relaxation time at the plateau in the order of seconds - in contrast to $\tau \sim 10^5 \text{ s}$ found for $\text{Li}_2(\text{Li}_{1-x}\text{Fe}_x)\text{N}$. The fortunate combination of a deviation from Arrhenius behaviour at high temperatures ($T > 10 \text{ K}$) with large values at the plateau leads to the extreme coercivities presented here. For potential data storage applications and stable magnetic materials, it is desirable to increase τ by suppressing the tunnel effect which can be achieved by enhanced

exchange coupling ^[11, 38]. On the other hand, studying tunnelling phenomena by itself requires isolated magnetic moments. Both goals can be satisfied by varying the Fe concentration in $\text{Li}_2(\text{Li}_{1-x}\text{Fe}_x)\text{N}$ accordingly. Thus for low Fe concentration of $x=0.0032$, statistically, 98% of the Fe atoms have only Li as nearest neighbours in the a - b plane and Fe-Fe interactions are negligible. Larger Fe concentrations show higher coercivity fields at the lowest temperatures (Supplementary Fig. 3), which are caused by larger relaxation times, indicating that Fe-Fe interactions are indeed detrimental to tunnelling. Provided the energy barriers can be further enhanced and tunnelling appropriately controlled this opens a route for the creation of hard permanent magnets from cheap and abundant elements.

One remaining question is: why is quantum tunnelling so elusive in inorganic compounds? Besides our discovery in $\text{Li}_2(\text{Li}_{1-x}\text{Fe}_x)\text{N}$ we are aware of only one other family of inorganic compounds showing macroscopic quantum tunnelling effects of the magnetization: $\text{LiY}_{0.998}\text{Ho}_{0.002}\text{F}_4$ (refs ^[26, 35]) and related systems. However, the characteristic energy scales are two orders of magnitude smaller than in $\text{Li}_2(\text{Li}_{1-x}\text{Fe}_x)\text{N}$ and magnetic hysteresis emerges only below $T=200$ mK with coercivity fields of $\mu_0 H_c=30$ mT. To observe a macroscopic quantum effect such as tunnelling of the magnetization, the interaction between the magnetic moments has to be small. Very generally, coupling leads to excitations (modes), which lead to dissipation that destroys the quantum state. This rules out systems with dense, interacting moments. Diluted systems of local magnetic moments have been the subject of extensive research mainly to study the Kondo effect. This necessarily requires metallic samples; the magnetic moments are not isolated but coupled to the electron bath which again leads to dissipation and the destruction of the quantum state. Insulating samples with diluted or non-interacting magnetic moments have

been far less studied - diluted magnetic semiconductors are explicitly excluded from this statement because of their finite carrier density. A possible explanation for the absence of magnetic tunnelling in insulators is a Jahn-Teller distortion which is frequently observed, e.g., in lanthanide zircons of the form RXO_4 (Ref. ^[39]) and references therein). According to the Jahn-Teller theorem ^[40], the orbital degeneracy of Fe should cause a structural distortion also for $Li_2(Li_{1-x}Fe_x)N$ in order to reach a stable state. In the diluted case it will occur locally for Fe and not necessarily for the whole crystal. Lifting the orbital degeneracy corresponds to a zero-orbital angular momentum, which is the only fully non-degenerate state. Consequently, a Jahn-Teller distortion would lead to a loss of the magnetic anisotropy and a decay of the energy-barrier. However, the Fe atom sits between two nitrogen neighbours which provide the dominant bonding. These three atoms can be regarded as acting like a linear molecule which is not subject to a Jahn-Teller distortion ^[40].

To summarize, we demonstrated a huge magnetic anisotropy and coercivity in $Li_2(Li_{1-x}Fe_x)N$ and want to emphasize the three properties which are probably essential for the emergence of macroscopic quantum tunnelling: the compound is insulating, the orbital magnetic moment of Fe is not quenched, and the N-Fe-N complex forms a linear molecule avoiding a Jahn-Teller distortion. These properties may serve as a basis for the design of materials featuring even higher characteristic energy scales.

Methods

Crystal growth

Starting materials were Li granules (Alfa Aesar, 99%), Li₃N powder (Alfa Aesar, 99.4%), and Fe granules (99.98%). The mixtures had a molar ratio of Li:Fe:N = 9- x_0 : x_0 :1 with $x_0 = 0$ to 0.5. A total mass of roughly 1.5 g was packed into a 3-cap Ta-crucible^[41] inside an Ar-filled glovebox. The Ta-crucible was sealed by arc-melting under inert atmosphere of ~0.6 bar Ar and subsequently sealed in a silica ampoule. The Li-Fe-N mixture was heated from room temperature to $T=900^{\circ}\text{C}$ over 4 h, cooled to $T=750^{\circ}\text{C}$ within 1.5 h, slowly cooled to $T=500^{\circ}\text{C}$ over 62 h and finally decanted to separate the Li₂(Li_{1- x} Fe _{x})N crystals from the excess liquid. Single crystals of hexagonal and plate-like habit with masses >100 mg could be obtained. The maximum lateral sizes of ≈ 10 mm were limited by the crucible size where the crystal thickness is typically ≈ 1 mm. Typically we found a few large single crystals with similar orientation clamped between the container walls above the bottom of the crucible and also several smaller ones attached to the bottom. We used pieces of the larger crystals for the magnetization measurements presented in this publication.

It should be noted that the smallest Fe concentration of $x=0.00028$, as measured by inductively coupled plasma mass spectrometry (ICP-MS, see below), was obtained without intentional introduction of Fe in the melt. Fe was most likely introduced as impurity from the starting materials or from the Ta-crucible.

Chemical analysis - ICP-MS

The $\text{Li}_2(\text{Li}_{1-x}\text{Fe}_x)\text{N}$ samples were analyzed using an inductively coupled plasma magnetic sector mass spectrometer (ICP-MS, Element 1, Thermo Scientific). The samples were introduced into the ICP via a low-flow nebulizer (PFA-100, Elemental Scientific Inc.) and double-pass spray chamber. The interface between the ICP and mass spectrometer was equipped with nickel sampler and skimmer (H-configuration) cones. The mass spectrometer was operated in medium resolution ($m/\Delta m=4000$) to separate the Fe^+ isotopes of interest from interfering species. The detector was operated in dual mode allowing for the operating software to selectively switch between analogue and counting measurements. Prior to sample analysis, the torch position and instrumental operating parameters (Table 1.) were adjusted for maximum peak height and signal stability. The main elements of interest for quantification were lithium (mass to charge ratio m/z 7) and iron (m/z 55.935 and 56.935). Tantalum (m/z 181) and calcium (m/z 43 and 44) were also measured to check for contamination from the crucible material and known impurities of the starting materials. Following these initial analyses, a full isotopic spectrum (m/z 7 to m/z 238) was measured in low resolution ($m/\Delta m=300$) for several representative samples to check for any other possible sources of contamination. Carbon, nitrogen, and oxygen could not be measured due to high background levels contributed by the acid solution, the argon gas, and the instrumental components. Minor amounts of tantalum and calcium were measured in the Li-Fe-N samples. All samples contained less than 0.4 mass % calcium (corresponding to $\text{Li}_{1-\delta}\text{Ca}_\delta$ with $\delta < 0.007$) and less than 0.1 mass % tantalum (corresponding to $\text{Li}_{1-\delta}\text{Ta}_\delta$ with $\delta < 0.0004$). The combined concentrations of all other contaminant elements comprised far less than 0.01 mass % of the solid samples.

All of the $\text{Li}_2(\text{Li}_{1-x}\text{Fe}_x)\text{N}$ samples were dissolved for ICP-MS analysis. Approximately 5 to 25 mg of solid sample was weighed accurately into an acid vapor washed Teflon bottle on a balance. A small amount (2 to 4 g) of cold ($\sim 3^\circ\text{C}$) deionized water was added and allowed to react. Once the sample mass stabilized, approximately 1.5 g of 70% nitric acid was added to completely dissolve the remaining solid. Upon complete dissolution, the solution was diluted with deionized water to a mass of 50 g. Aliquots of these original solutions were diluted with prepared aqueous 1% nitric acid to a concentration of 1 to 5 ppm in terms of the original solid sample mass. Standard solutions were prepared for the quantification of iron and lithium in the samples. A 1 ppm iron and lithium standard was prepared by diluting 1000 ppm stock solutions (SPEX CertiPrep, High-Purity Standards) with cleaned 1% nitric acid. Lower concentration standards were prepared via dilutions of the original 1 ppm standard solution. Blanks of the water and acids were analyzed and had negligible amounts of the analyte elements. The water used was 18 M Ω cm (Barnstead Nanopure) and the nitric acid was purified by sub-boiling distillation (Classic Sub-boiling Still Assembly, Savillex) before use. Lithium is prone to memory effects in ICP-MS due to either sample introduction or deposition and vaporization of Li from the cones. The Li^+ (and Fe^+) signals from the samples and standards all rinsed out to baseline between the measurements.

References

1. Gatteschi, D. & Sessoli, R. Quantum tunneling of magnetization and related phenomena in molecular materials. *Angew. Chem. Int. Ed. Engl.* **42**, 268-297 (2003).
2. Paulsen, C., Park, J.G., Barbara, B., Sessoli, R. & Caneschi, A. Novel features in the relaxation times of Mn_{12}Ac . *J. Magn. Magn. Mater.* **140-144**, 379-380 (1995).
3. Takahashi, S. *et al.* Decoherence in crystals of quantum molecular magnets. *Nature* **476**, 76-79 (2011).

4. Leuenberger, M.N., and Loss, D. Quantum computing in molecular magnets. *Nature* **410**, 789-793 (2001).
5. Bogani, L. and Wernsdorfer, W. Molecular spintronics using single-molecule magnets. *Nat. Mater.* **7**, 179-186 (2008).
6. Strandberg, T.O., Canali, C.M. & MacDonald, A.H. Transition-metal dimers and physical limits on magnetic anisotropy. *Nat. Mater.* **6**, 648-651 (2007).
7. Gambardella, P., *et al.* Giant magnetic anisotropy of single cobalt atoms and nanoparticles. *Science* **300**, 1130-1133 (2003).
8. Khajetoorians, A.A., *et al.* Current-driven spin dynamics of artificially constructed quantum magnets. *Science* **339**, 55-59 (2013).
9. Sessoli, R., Gatteschi, D., Caneschi, A. & Novak, M.A. Magnetic bistability in a metal-ion cluster. *Nature* **365**, 141-143 (1993).
10. Lin, P.H., *et al.* A polynuclear lanthanide single-molecule magnet with record anisotropic barrier. *Angew. Chem. Int. Ed. Engl.* **48**, 9489-9492 (2009).
11. Rinehart, J.D., Fang, M., Evans, W.J. & Long, J.R. Strong exchange and magnetic blocking in N_2^{3-} -radical-bridged lanthanide complexes. *Nat. Chem.* **3**, 538-542 (2011).
12. Osa, S. *et al.* A tetranuclear 3d-4f single molecule magnet: $[Cu^{II}LTb^{III}(hfac)_2]_2$. *J. Am. Chem. Soc.* **126**, 420-421 (2004).
13. Ishikawa, N., Sugita, M., Ishikawa, T., Koshihara, S. & Kaizu, Y. Lanthanide double-decker complexes functioning as magnets at the single-molecular level. *J. Am. Chem. Soc.* **125**, 8694-8695 (2003).
14. Jiang, S.D., Wang, B.W., Su, G., Wang, Z.M. & Gao, S. A mononuclear dysprosium complex featuring single-molecule-magnet behavior. *Angew. Chem. Int. Ed. Engl.* **122**, 7610-7613 (2010).
15. Ishikawa, N. Single molecule magnet with single lanthanide ion. *Polyhedron* **26**, 2147-2153 (2007).
16. Luzon, J. & Sessoli, R. Lanthanides in molecular magnetism: so fascinating, so challenging. *Dalton Trans.* **41**, 13556-13567 (2012).
17. Freedman, D.E., *et al.* Slow magnetic relaxation in a high-spin iron (II) complex. *J. Am. Chem.* **132**, 1224-1225 (2010).

18. Zadrozny, J.M. & Long, J.R. Slow magnetic relaxation at zero field in the tetrahedral complex $[\text{Co}(\text{SPh})_4]^{2-}$. *J. Am. Chem. Soc.* **133**, 20732-20734 (2011).
19. Zadrozny, J.M. *et al.* Magnetic blocking in a linear iron (I) complex. *Nat. Chem.* **5**, 577-581 (2013).
20. Honda, K. & Kaya, S. On the magnetization of single crystals of iron. *Sci. Rep. Tohoku Univ.* **15**, 721-753 (1926).
21. Kaya, S. On the magnetization of single crystals of nickel, on the magnetization of single crystals of cobalt. *Sci. Rep. Tohoku Univ.* **17**, 639-663 and 1157-1177 (1928).
22. Klatyk, J. *et al.* Large orbital moments and internal magnetic fields in lithium nitroferrate(I). *Phys. Rev. Lett.* **88**, 207202 (2002).
23. Ksenofontov, V. *et al.* In situ - High Temperature Mossbauer Spectroscopy of Iron Nitrides and Nitridoferrates. *Z. Anorg. Allg. Chem.* **629**, 1787-1794 (2003).
24. Novak, P. & Wagner, F.R. Electronic structure of lithium nitridoferrate: effects of correlation and spin-orbit coupling. *Phys. Rev. B* **66**, 184434 (2002).
25. Uehara, M., Barbara, B., Dieny, B. & Stamp, P.E. Staircase behaviour in the magnetization reversal of a chemically disordered magnet at low temperature. *Phys. Lett. A* **114**, 23-26 (1986).
26. Giraud, R., Tkachuk, A.M. & Barbara, B. Quantum dynamics of atomic magnets: cotunneling and dipolar-biased tunneling. *Phys. Rev. Lett.* **91**, 257204 (2003).
27. Rabenau, A. & Schultz, H. Re-evaluation of the lithium nitride structure. *J. Less. Common Met.* **50**, 155-159 (1976).
28. Klatyk, J. & Kniep, R. Crystal structure of dilithium (nitrodolomite/ferrate(I)), $\text{Li}_2[(\text{Li}_{1-x}\text{Fe}_x)\text{N}]$, $x=0.63$. *Z. Krist. New Cryst. Struct.* **214**, 447-118 (1999).
29. Yamada, A., Matsumoto, S. & Nakamura, Y. Direct solid-state synthesis and large-capacity anode operation of $\text{Li}_{3-x}\text{Fe}_x\text{N}$. *J. Mater. Chem.* **21**, 10021-10025 (2011).
30. Gregory, D. Nitride chemistry of the s-block elements. *Coord. Chem. Rev.* **215**, 301-345 (2001).
31. Barbara, B. *et al.* Evidence for resonant magnetic tunneling of rare-earth ions: from insulating to metallic matrix. *J. Magn. Magn. Mater.* **272-276**, 1024-1029 (2004).
32. Wernsdorfer, W. & Sessoli, R. Quantum phase interference and parity effects in magnetic molecular clusters. *Science* **284**, 133-135 (1999).

33. Cullity, B.D. in *Introduction to Magnetic Materials*. (ed. Cohen, M.) 442 (Addison-Wesley Publishing Company Reading, 1972).
34. Sanngregorio, C., Ohm, T., Paulsen, C., Sessoli, R. & Gatteschi, D. Quantum tunneling of the magnetization of an iron cluster nanomagnet. *Phys. Rev. Lett.* **78**, 4645-4648 (1997).
35. Giraud, R., Wernsdorfer, W., Tkachuk, A.M., Mailly, D. & Barbara, B. Nuclear spin driven quantum relaxation in $\text{LiY}_{0.998}\text{Ho}_{0.002}\text{F}_4$. *Phys. Rev. Lett.* **87**, 057203 (2001).
36. Ishikawa, N., Sugita, M., Ishikawa, T., Koshihara, S. & Kaizu, Y. Mononuclear lanthanide complexes with a long magnetization relaxation time at high temperatures: a new category of magnets at the single-molecular level. *J. Phys. Chem. B.* **108**, 11265-11271 (2004).
37. Gonidec, M. *et al.* Surface supramolecular organization of a terbium (III) double-decker complex on graphite and its single molecule magnet behavior. *J. Am. Chem. Soc.* **133**, 6603-3312 (2011).
38. Wernsdorfer, W., Aliaga-Alcalde, N., Hendrickson, D.N. & Christou, G. Exchange-biased quantum tunnelling in a supramolecular dimer of single-molecule magnets. *Nature* **416**, 406-409 (2002).
39. Kirschbaum, K., Martin, K., Parrish, D.A. & Pinkerton, A.A. Cooperative Jahn-Teller induced phase transition of TbVO_4 : Single crystal structure analyses of the tetragonal high temperature phase and twinned orthorhombic phase below 33 K. *J. Phys. Condens. Matter* **11**, 4483 (1999).
40. Jahn, H.A. & Teller, E. Stability of polyatomic molecules in degenerate electronic states. I. orbital degeneracy. *Proc. R Soc. Lond. A* **161**, 220-235 (1937).
41. Canfield, P.C. & Fisher, I.R. High-temperature solution growth of intermetallic single crystals and quasicrystals. *J. Cryst. Growth* **225**, 155-161 (2001).

FIGURES AND TABLES

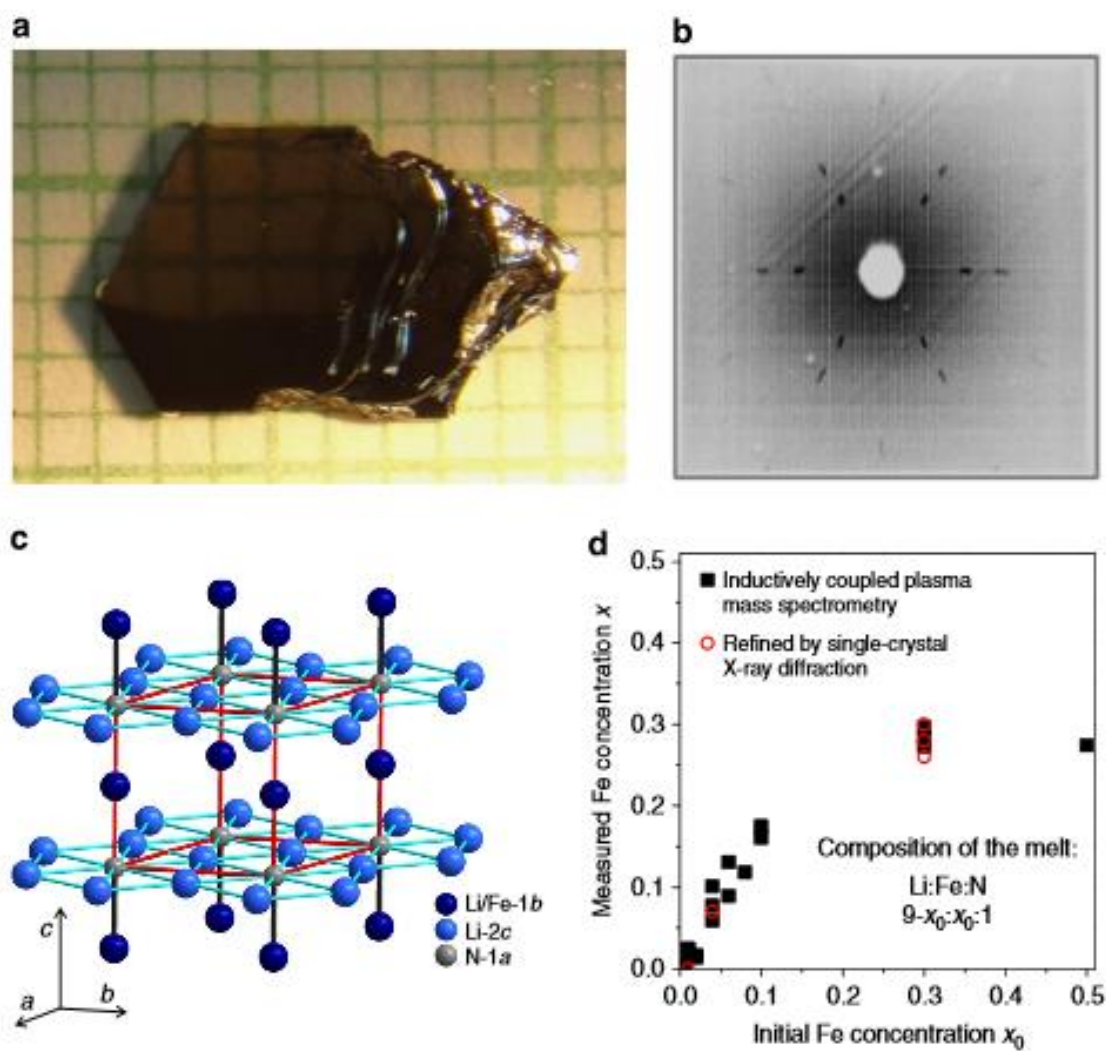


Figure 1: Basic structural properties. **a**, Single crystal of $\text{Li}_2(\text{Li}_{0.90}\text{Fe}_{0.10})\text{N}$ on a millimetre grid and **b**, corresponding Laue-back-reflection pattern. The crystal is not transparent and the faint grid pattern is a reflection off of the lens and the flat surface of the reflecting top facet. **c**, Crystal structure with Li_2N layers separated by a second Li-site which is partially occupied by Fe. The unit cell of the hexagonal lattice is indicated by red lines. **d**, Measured Fe concentration x as a function of the Fe concentration in the melt x_0 . For small concentrations, x tends to be larger than x_0 , however, a plateau in x as a function of x_0 emerges for $x_0 \gtrsim 0.3$. x was determined by both inductively coupled plasma mass spectrometry (see Methods) and by refinement of single crystal X-ray diffraction data (see Supplementary Fig. 1).

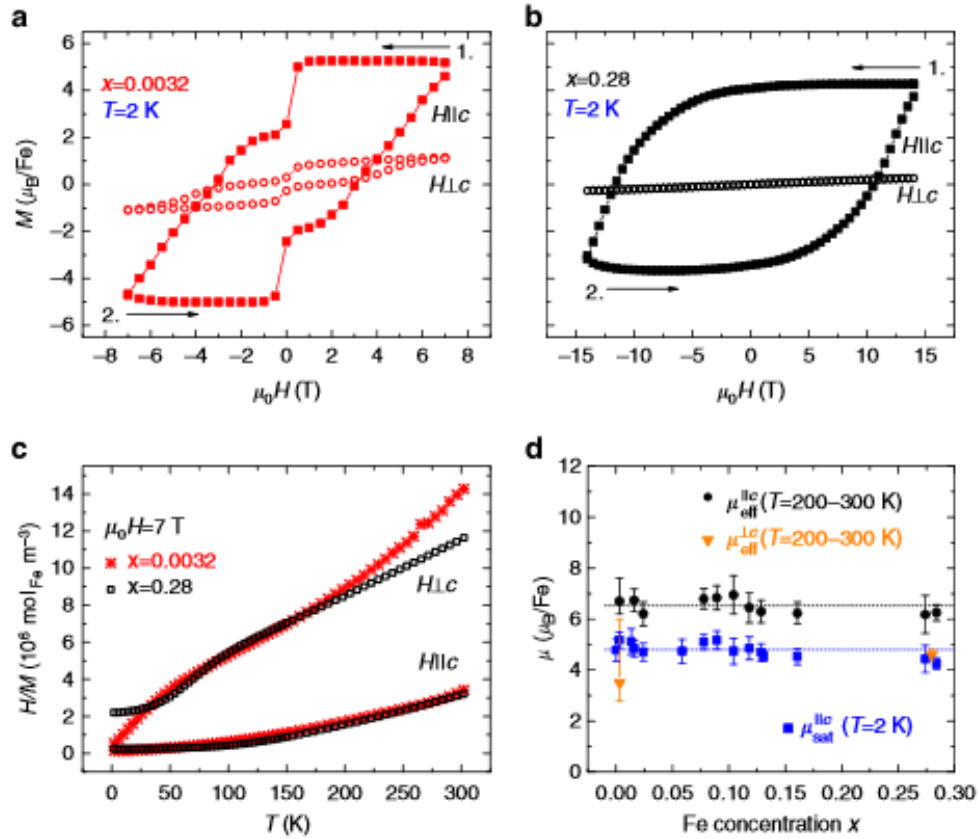


Figure 2: Basic magnetic properties of $\text{Li}_2(\text{Li}_{1-x}\text{Fe}_x)\text{N}$. **a, b**, Large hysteresis in the magnetization, $M(H)$, and a pronounced anisotropy depending on the orientation of the applied magnetic field, H , with respect to the crystallographic axes for $x = 0.0032$ and $x = 0.28$. Whereas M can be saturated for $H\parallel c$ it is slowly increasing with H for $H\perp c$ up to the highest available fields. **c**, The temperature dependence of the inverse magnetization for $x = 0.28$ follows a Curie-Weiss-law for $T \gtrsim 150$ K with effective moments of $\mu_{\text{eff}}^{\perp c} = 4.6(3)\mu_{\text{B}}$ for $H\perp c$ and $\mu_{\text{eff}}^{\parallel c} = 6.3(4)\mu_{\text{B}}$ for $H\parallel c$. Similar behaviour is observed for the two orders of magnitude lower concentration of $x = 0.0032$ where the deviation for $H\perp c$ at $T > 200$ K can be caused by a temperature-independent diamagnetic background of the Li_3N host which is negligible for higher Fe concentrations. **d**, Both, μ_{sat} and μ_{eff} were found to be largely independent of x over the whole investigated range of $x = 0.00028$ to 0.28 . The error bars are calculated based on the errors in assessing the sample mass and the Fe concentration and, for $x=0.0032$, on a diamagnetic contribution of the Li_3N host. The average values are $\mu_{\text{sat}}^{\parallel c} = 4.8(4)$ and $\mu_{\text{eff}}^{\parallel c} = 6.5(4)\mu_{\text{B}}$.

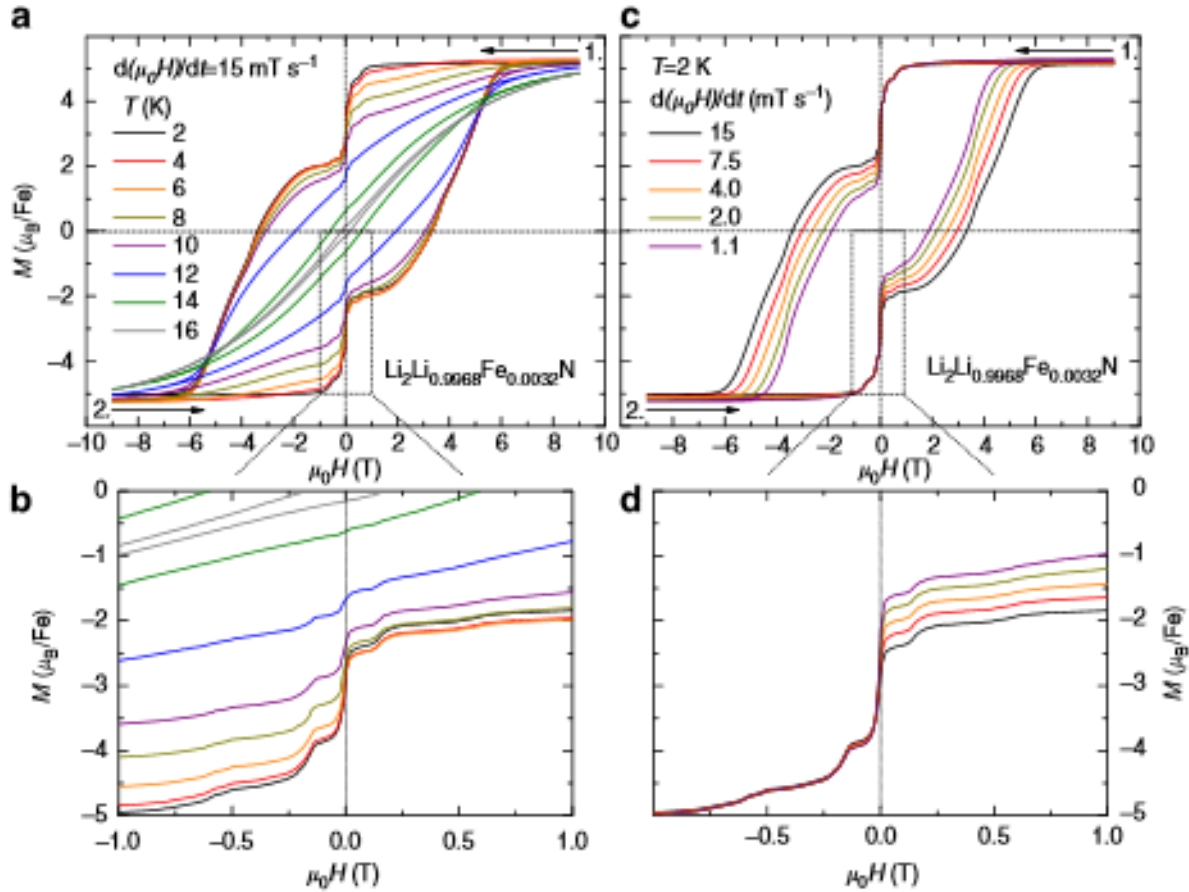


Figure 3: Temperature and sweep-rate dependence of the magnetization of $\text{Li}_2(\text{Li}_{1-x}\text{Fe}_x)\text{N}$ for $x = 0.0032$, $H \parallel c$. **a**, Hysteresis emerges for $T \leq 16\text{K}$ and the coercivity fields, H_c , are essentially temperature-independent below $T = 10\text{K}$. **b**, The clear steps in the magnetization are smeared out with increasing temperature and disappear for $T \geq 16\text{K}$. **c**, The pronounced sweep-rate dependence of the magnetization reveals the dynamic nature of the hysteresis. **d**, Only the step at $H = 0$ depends significantly on the sweep-rate indicating that the relaxation at the smaller steps at $\mu_0 H = \pm 0.15, \pm 0.55\text{T}$ is fast on the time-scale of the experiment. The step at $H = 0$ is attributed to a flip of the Fe magnetic moment from below to above the crystallographic a - b plane. The energy barrier associated with this transition seems to dominate the relaxation process and forms the global maximum in the magnetic anisotropy energy. The smaller steps are accordingly associated with tunnelling through smaller, local maxima.

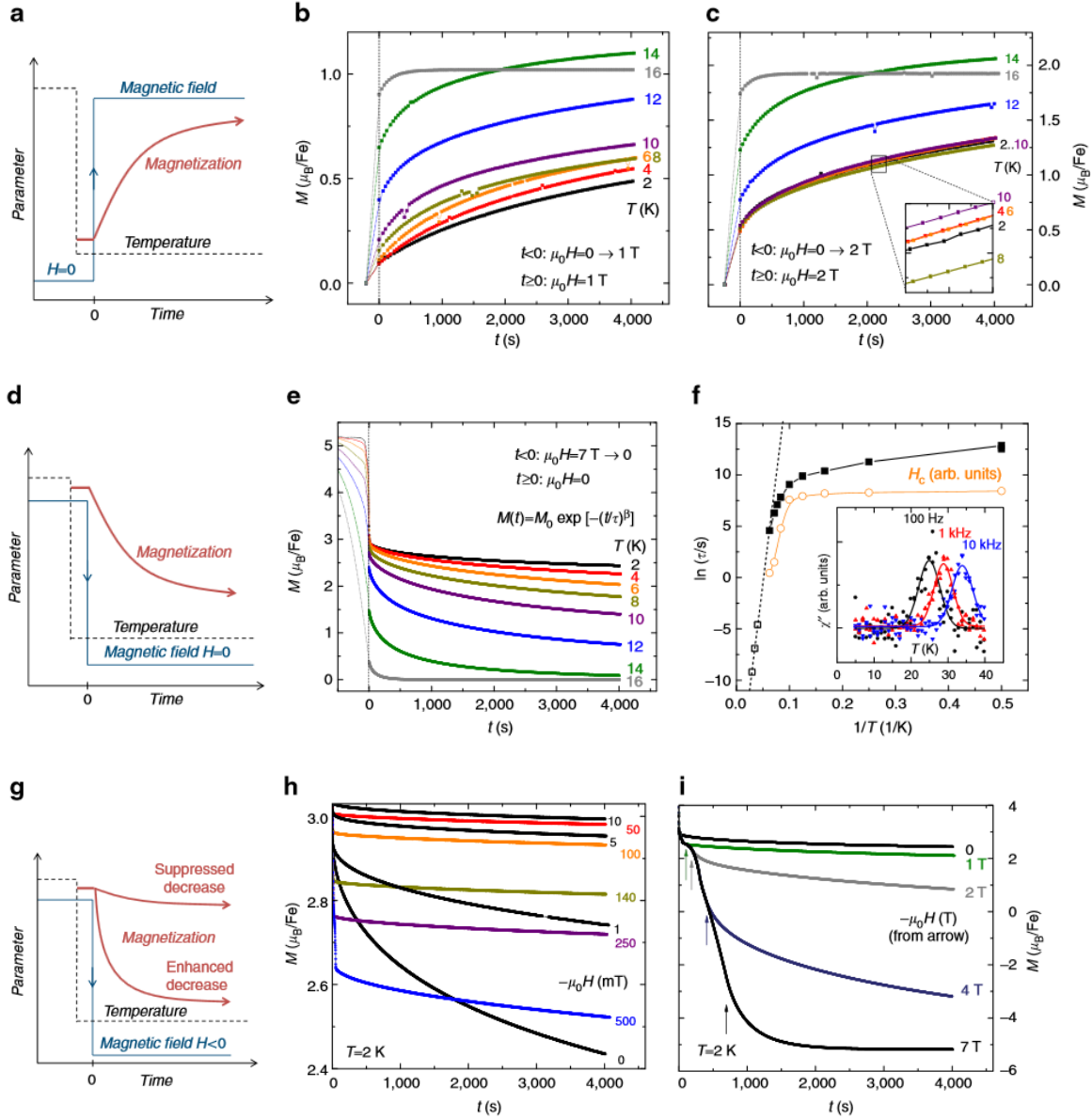


Figure 4: Time-dependence of the magnetization. **a, d, and g**, Schematics of different relaxation processes and corresponding experimental data on $\text{Li}_2(\text{Li}_{0.9968}\text{Fe}_{0.0032})\text{N}$ to the right. **b**, The increase in the magnetization as a function of time, $M(t)$, below $T = 10$ K is only weakly temperature dependent for $\mu_0 H = 1$ T. **c**, Increasing the applied field to $\mu_0 H = 2$ T leads to an essentially temperature-independent relaxation below $T = 10$ K which is inconsistent with a thermally activated relaxation process. **e**, Decrease in $M(t)$ after ramping the field from $\mu_0 H = 7$ T to 0. $M(t)$ is fit to a stretched exponential function and the obtained relaxation times, τ , are shown as closed squares in form of an Arrhenius-plot in **f**. **f**, τ determined from the imaginary part of the ac-magnetic susceptibility, $\chi''(T)$ (inset), is shown by open squares. Thermally activated behaviour is observed at higher temperatures (dashed line). The formation of a plateau towards lower temperatures is incompatible with thermally activated behaviour and indicates the relevance of quantum tunnelling. The coercivity field (open circles, sweep-rate 15 mT/s) shows similar temperature-dependence indicating slow relaxation as the origin of spontaneous magnetization. **g**, Small negative fields of a few mT, applied opposite to the initial applied field of $\mu_0 H = 7$ T, significantly reduce the decrease in $M(t)$ compared to $H = 0$. **i**, In contrast, $M(t)$ decreases faster in larger negative fields of $|\mu_0 H| \geq 1$ T.

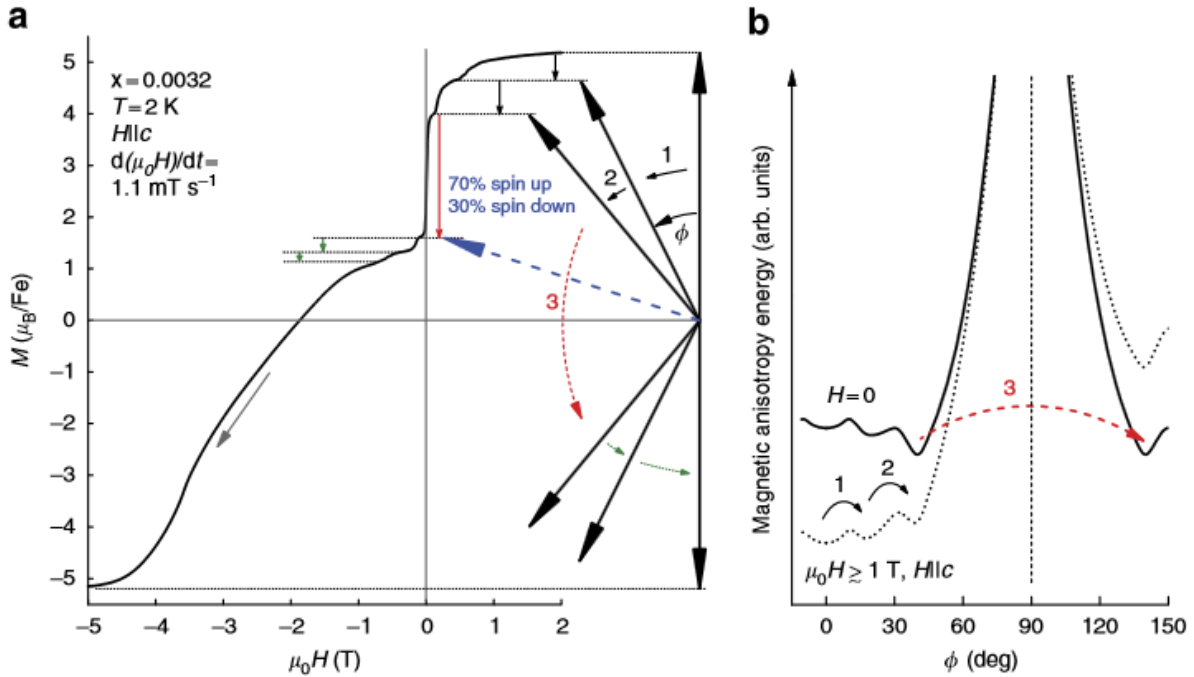


Figure 5: Magnetic moment orientation and anisotropy energy. **a**, Magnetization of $\text{Li}_2(\text{Li}_{1-x}\text{Fe}_x)\text{N}$ and a corresponding, possible orientation of the magnetic moment. This simplified model assumes a constant magnitude of the magnetic moment independent of the orientation with respect to the c -axis (ϕ is the angle between moment and c -axis). The plateau after step 2 corresponds to $\phi \sim 40^\circ$. The large jump in $M(H)$ at $H \sim 0$ is in accordance with a reorientation of 30% of the Fe magnetic moments from spin-up ($\phi \sim 40^\circ$) to spin-down ($\phi \sim 140^\circ$). A further, rapid reorientation for $H < 0$ is blocked because the resonance condition for magnetic tunnelling is destroyed for $H \neq 0$. **b**, Possible schematic of the magnetic anisotropy energy as a function of the angle to the crystallographic c -axis. The global minimum in zero-field appears at an angle of $\phi \sim 40^\circ$. Adding a sufficiently large Zeeman term for an applied field along the c -axis (dotted line) leads to a global minimum located at $\phi = 0^\circ$. The large step in the M - H loop occurring at zero field is associated with the resonant tunnelling through the large energy barrier centered at $\phi = 90^\circ$. Accordingly, the smaller steps correspond to transitions from a local to the (actual) global minimum in the total magnetic energy.

Table 1: ICP-MS operating parameters

RF power	1150 W
Outer gas flow	16 l min ⁻¹
Auxiliary gas flow	1.5 l min ⁻¹
Sample gas flow (argon)	1.04 l min ⁻¹
Sampling position	13 mm from load coil, on center
Signal ratios for tuning and optimization	Ce ²⁺ /Ce ⁺ ≈ 4%, CeO ⁺ /Ce ⁺ ≈ 7%

APPENDIX B. ALTERNATING MAGNETIC ANISOTROPY OF $\text{Li}_2(\text{Li}_{1-x}\text{T}_x)\text{N}$

WITH $T = \text{Mn, Fe, Co, AND Ni}$

A. Jesche,¹ L. Ke,¹ J. L. Jacobs,^{1,2} B. Harmon,^{1,3} R.S. Houk,^{1,2} and P. C. Canfield^{1,3}

1 The Ames Laboratory, Iowa State University, Ames, Iowa, USA

2 Department of Chemistry, Iowa State University, Ames, Iowa, USA

3 Department of Physics and Astronomy, Iowa State University, Ames, USA

A paper published in Physical Review B, 2015, 91(18)

Abstract

Substantial amounts of the transition metals Mn, Fe, Co, and Ni can be substituted for Li in single crystalline $\text{Li}_2(\text{Li}_{1-x}\text{T}_x)\text{N}$. Isothermal and temperature-dependent magnetization measurements reveal local magnetic moments with magnitudes significantly exceeding the spin-only value. The additional contributions stem from unquenched orbital moments that lead to rare-earth-like behavior of the magnetic properties. Accordingly, extremely large magnetic anisotropies have been found. Most notably, the magnetic anisotropy alternates as easy-plane \rightarrow easy-axis \rightarrow easy-plane \rightarrow easy-axis when progressing from $T = \text{Mn} \rightarrow \text{Fe} \rightarrow \text{Co} \rightarrow \text{Ni}$. This behavior can be understood based on a perturbation approach in an analytical, single-ion model. The calculated magnetic anisotropies show a surprisingly good agreement with the experiment and capture the basic features observed for the different transition metals.

Magnetic anisotropy or magnetic anisotropy energy (MAE) is a fundamental concept in solid state science affecting magnetic data storage, permanent magnets and the investigation of

various basic model systems. In a simple picture, MAE is the energy necessary to reorient magnetic moments in a certain material. Its value is largely determined by the single-ion anisotropy of the magnetic centers. This anisotropy stems from the orbital contribution to the magnetic moment (either directly or indirectly via spin-orbit coupling). Significant orbital contributions to the magnetic moment and the resulting large MAEs are usually associated with rare-earth elements. In contrast, the orbital moment in 3d transition metals is normally quenched by the crystal electric field. Accordingly, the magnetic anisotropy of these elements is often small or non-existent.

Recently, we have found a remarkable exception to this trend: iron, when substituted in lithium nitride, $\text{Li}_2(\text{Li}_{1-x}\text{Fe}_x)\text{N}$, behaves in many aspects like a rare-earth element^[1]. With an estimated MAE of several hundred Kelvin and, in accordance, an observed coercivity field of more than 11 Tesla this compound exceeds even the largest values observed in rare-earth based permanent magnets. Besides iron, other 3d transition metal substitutions were synthesized, in polycrystalline form, as early as 1949 by Sachsze and Juza^[2] and have been subjects of ongoing experiments^[3, 4, 5, 6, 7, 8, 9, 10] and theoretical investigations^[11, 12, 13]. It has been found that $T=\text{Mn}$, Fe, Co, Ni, and Cu can be substituted for one of the Li-sites: the two-fold coordinated 1b Wyckoff site. Indications for an unusual oxidation state of +1 were also reported^[2, 5, 6, 7, 14]. The transition metals carry a sizable local magnetic moment except for $T=\text{Cu}$ and highly concentrated $T=\text{Ni}$ ^[5, 7, 8]. Due to a lack of large enough single crystals, there has been no direct access to the anisotropy of the physical properties. Only recently we developed a single crystal growth technique that is based on a lithium-rich flux and is applicable to $\text{Li}_2(\text{Li}_{1-x}T_x)\text{N}$ as well as other nitrides and lithium based compounds^[14].

Here we present the magnetic anisotropy of $\text{Li}_2(\text{Li}_{1-x}\text{T}_x)\text{N}$ for $T = \text{Mn, Co, and Ni}$ and compare the results to our earlier $T=\text{Fe}$ work. Two concentrations, a dilute one and a more concentrated one, were grown, under similar conditions, for the different transition metals. The starting materials were mixed in a molar ratio of $\text{Li:T:Li}_3\text{N} = 8.97:0.03:1$ and $8.7:0.3:1$ for dilute and more concentrated samples, respectively. The mixtures were packed in a three-cap Ta crucible^[14, 15] heated from room temperature to $T=900^\circ\text{C}$ over 5 h, cooled to $T=750^\circ\text{C}$ within 1.5 h, slowly cooled to $T=500^\circ\text{C}$ over 60 h, and finally decanted to separate the single crystals from the excess flux. A picture of three representative single crystals on a millimeter grid is shown in Fig. 3b below. The actual transition metal concentration (as opposed to the nominally melt compositions given above) in the investigated single crystals was determined by chemical analysis using inductively coupled plasma mass spectrometry (ICP-MS)^[1]. The ICP-MS instrument was provided by Analytik Jena. The deviation from the initial concentration, with respect to nitrogen, differs from one transition metal to the other and also depends on the concentration (see Fig. 1 for the measured transition metal concentrations). However, the obtained concentrations, x , clearly reflect the different initial values and allow us to study the *dilute* and *concentrated* regimes. Magnetization measurements were performed using a Quantum Design Magnetic Property Measurement System equipped with a 7 Tesla magnet. The MAE was calculated analytically in a single-ion model based on second order perturbation theory using the Green's function method.

Figure 1 shows the isothermal magnetization in Bohr magnetons per transition metal ion at $T=2\text{ K}$. The measurements were performed for magnetic field applied parallel and perpendicular to the hexagonal c -axis, shown by black squares and red circles, respectively.

Results obtained for the dilute transition metal substitutions are shown on the left-hand side, more concentrated substitutions are shown to the right. The largest available field of $\mu_0 H = 7$ T allows for saturation of the magnetization only for Fe and dilute Ni (and comes close to saturation for dilute Mn). Furthermore, the anisotropy field (crossing point of the M -curves for $H \parallel c$ and $H \perp c$) lies well above the largest available fields. Therefore, it is not possible to accurately quantify the MAE from our data (for $T \neq \text{Fe}$). However, the alternating change from easy-plane to easy-axis behavior is evident and independent of x . Further trends can be recognized: (I) The anisotropy decreases with increasing x , except for $T = \text{Fe}$. (II) The magnetization values that are approached for $\mu_0 H = 7$ T decrease with increasing x . (III) The anisotropy observed for $T = \text{Mn}$ is significantly smaller than that observed for the other transition metals (except for concentrated Ni). (IV) Even though the sign and magnitude of the anisotropy of dilute Fe and Ni appear to be very similar, the large hysteresis found for Fe-substitution is absent for Ni. (It is also absent for the planar $T = \text{Mn}$ and Co.) Demagnetization fields amount to only a small fraction of the applied magnetic fields and can be neglected.

Further information about the orbital moment contributions can be obtained from the effective magnetic moments, determined from the temperature-dependence of the magnetization. Figure 2 shows the temperature-dependent magnetic susceptibility, $\chi(T) = M/H$, for both orientations of the applied field. Reasonable agreement with Curie-Weiss behavior is observed for $T > 150$ K. The contribution of the core diamagnetism of the Li_3N host significantly affects the diluted systems but can be neglected for the larger concentrations shown on the right hand panel of Fig. ?. Subtracting the ionic contributions of Li^{1+} [16] and N^{3-} [17] leads to better agreement with the expected linear behavior of $\chi^{-1}(T)$ over a wide temperature range (solid lines in Fig. 2).

The summary of the obtained μ_{eff} values and a comparison with the spin-only values are given in Table I (extracted from the temperature range $150 \text{ K} < T < 300 \text{ K}$).

In the diluted systems μ_{eff} significantly exceeds the spin-only value for the easy-axis systems with $T = \text{Fe}$ and $T = \text{Ni}$ in particular for field applied along the easy-axis. The diluted and the concentrated system of $T = \text{Fe}$ show the largest enhancement of μ_{eff} when compared to the spin-only value and accordingly the magnetic anisotropy observed in the isothermal magnetization measurements, $M(H)$, is by far the largest among the different transition metals (Fig. 1). In the easy-plane systems μ_{eff} is only slightly enhanced. For the case of $T = \text{Mn}$ this is directly reflected in the rather low magnetic anisotropy observed in $M(H)$. Furthermore, the observation of smaller effective moments for concentrated $T = \text{Mn}$ when compared with the dilute system goes hand in hand with a further decrease of the anisotropy in $M(H)$. In a similar fashion, the decrease of the effective moments for concentrated systems of both $T = \text{Co}$ and $T = \text{Ni}$ when compared to the dilute case is accompanied by a corresponding decrease of the magnetic anisotropy in $M(H)$.

However, for dilute $T = \text{Co}$, a large magnetic anisotropy is apparent in $M(H)$ (Fig. 1) even though the effective moments are only slightly enhanced when compared to the spin-only value. A more sophisticated analysis is needed to describe the observed behavior. The input parameters for the employed analytical model are obtained from a simplified representation (Fig. 3a) of the detailed electronic band structure. These were calculated earlier in the framework of local spin density approximation (LSDA) for two different supercells which correspond to Fe-concentrations of $x=0.17$ [13] and $x=0.50$ [18, 19, 13], respectively. The calculated densities of states (DOS) projected on the $3d$ states of isolated Fe-atoms turn out to be fairly similar. In particular, a

sharp peak in the minority spin channel that intersects the Fermi level appears in both cases. A further dilution of the Fe-concentration is not expected to cause tremendous changes of the projected Fe-DOS, since the Fe-atoms are already well separated.

In our analytical model we consider only the DOS of the four $3d$ states with $m=\pm 1$ and $m=\pm 2$ and model them by Lorentzian-shaped peaks with a half-width $w=60$ meV (m : orbital quantum number). The $m=0$ states ($3d_{z^2}$) are not included in the modeling since they are well below the Fermi level and have negligible effects on the MAE. The MAE depends on the crystal field splitting Δc (energy difference between $m=\pm 1$ and $m=\pm 2$ states), on the spin splitting Δs (energy difference between spin-up and spin-down), and on w [20]. To facilitate the calculation of the MAE for $T=\text{Mn}$, Co , and Ni , only the Fermi level is shifted according to the number of $3d$ electrons leaving the band structure unchanged (rigid band approximation). Since each degenerate state, and accordingly each Lorentzian in Fig. 3a, can accommodate two electrons, the Fermi level either intersects the degenerate peaks or sits in the middle, between two PDOS peaks (for an integer electron number). For the case of $T=\text{Mn}^{1+}$, six $3d$ electrons have to be considered. Five of these occupy the majority band (upper panel in Fig. 3a) and the remaining one the $m=0$ state of the minority band (lower panel in Fig. 3a, the $m=0$ state lies well below the Fermi level and is not shown). Accordingly, the Fermi level for $T=\text{Mn}^{1+}$ is located between the $m=\pm 1$ spin-up and the $m=\pm 2$ spin-down states. For the case of $T=\text{Fe}^{1+}$, one more electron has to be placed in the minority band. Therefore, one of the two $m=\pm 2$ spin-down states has to be occupied. Accordingly, the Fermi level intersects the center of the $m=\pm 2$ spin-down peak. Adding one more electron shifts the Fermi level right between the $m=\pm 2$ and $m=\pm 1$ spin-down states corresponding to $T=\text{Co}^{1+}$ with eight $3d$ electrons. For $T=\text{Ni}^{1+}$, one more $3d$ electron has to be considered and,

similar to the case of $T=\text{Fe}^{1+}$, the Fermi level intersects the center of the $m=\pm 1$ spin-down peak. Furthermore, this allows for the calculation of the MAE as a continuous function of the band filling. It is worth mentioning that the spin orbit coupling is not included in the schematic band structure.

The pairwise orbital susceptibility, and therefore the MAE, is now fully determined by w and the energy difference between the Fermi level and the involved orbitals. The later one includes the effect of spin splitting and crystal electric field splitting. The pair susceptibility is proportional to the term $w/[(\varepsilon_{\text{F}}-\varepsilon_m^\sigma)^2+w^2]$, where ε_{F} is the Fermi energy, ε_m^σ the DOS peak position with $\sigma = \{\text{spin-up, spin-down}\}$ [20]. For $T=\text{Fe}$ the $m=\pm 2$ spin-down state is located right at the Fermi level, that is $\varepsilon_{\text{F}}=\varepsilon_2^\downarrow$. This leads to a resonance-like enhancement of the pair susceptibility that is only limited by the peak width w . The MAE for $T=\text{Fe}$ is therefore dominated by the contribution of the $m=\pm 2$ spin-down state. This result is in full analogy to the LSDA-based calculation, that revealed a splitting of this state caused by spin-orbit coupling which leads to large MAE values [18, 19]. For $T=\text{Mn}$ and Co no such resonance of the pair susceptibility occurs and the resulting MAE, which is determined by the sum over all orbital pairs, turns out to be negative.

The MAEs calculated in our analytical model are shown in Fig. 3b as solid line (positive values correspond to an easy-axis, negative ones to an easy-plane system). Values obtained by LSDA methods [20] are given for comparison (square data points). The MAE of Mn, Fe, Co, and Ni correspond to the respective integer number of $3d$ electrons. Most remarkably, this simplified model is sufficient to capture all basic features of the magnetic anisotropy even though the 'exact' band structure [11, 13] differs in several details from the schematic representation shown in

Fig. 3a. The largest MAE is calculated for $T=\text{Fe}$. Given the simplicity of the model, the calculated value of 15 meV is in reasonable agreement with our experimental result of 13 meV for the dilute and 27 meV for the more concentrated case (estimated from the linearly extrapolated anisotropy field and the measured saturation magnetization) and with the LSDA result. The MAE calculated for $T=\text{Co}$ is significantly smaller and of opposite sign. The smallest MAE is calculated for $T=\text{Mn}$. Both, sign and relative magnitude of the calculated MAE fit well to the experimentally observed magnetic anisotropy (Fig. 1). One exception is observed for the $T=\text{Ni}$ system. The single-ion model gives a MAE of about half of the $T=\text{Fe}$ value that results mainly from an $|m|^2$ dependence of the MAE [20]. However, the experiment suggests that the MAE for *concentrated* $T=\text{Ni}$ is reduced by more than an order of magnitude when compared to $T=\text{Fe}$. This discrepancy is mainly caused by an underestimation of the DOS peak width of the $|m|=1$ spin-down states that turns out to be larger than the $|m|=2$ state (the MAE decreases with increasing band width, roughly following $1/w$). Such a peak-broadening corresponds to an increasing delocalization which is indeed manifested in the decreasing electrical resistivity of $\text{Li}_2(\text{Li}_{1-x}\text{Ni}_x)\text{N}$ for $x \geq 0.8$ [7]. Furthermore, spin-splitting and crystal field splitting for $T=\text{Ni}$ are smaller than for $T=\text{Fe}$ [13, 20]. Adjusting the schematic band structure accordingly leads to a better agreement between single-ion model and experiment. There is also good agreement between our experimental results and recent calculations of the MAEs based on LSDA calculations [13].

The orbital magnetic moment and the associated large MAE are likely direct consequences of the local symmetry of the transition metal. This actual linear, two-fold coordination between the nearest-neighbor nitrogen atoms gives rise to an effective, linear molecule (N- T -N). And as such, it is not subject to the Jahn-Teller effect [21] which is driven by lifting the orbital degeneracy. Therefore, a quenching of the orbital magnetic moment by a lattice

distortion does not take place in $\text{Li}_2(\text{Li}_{1-x}\text{T}_x)\text{N}$. Within this symmetry the changing of the transition metal gives rise to a dramatic change of both experimental and calculated anisotropies. It remains to be seen whether this behavior is generic to linear complexes or restricted to the special case of $\text{Li}_2(\text{Li}_{1-x}\text{T}_x)\text{N}$. Further indications for the relevance of a linear arrangement to the formation of orbital magnetic moments and large MAE in $3d$ transition metals can be found in seemingly unrelated systems: Ad-atoms on surfaces ^[22] (diatomic molecules built from substrate oxygen and adsorbed cobalt) and some linear transition metal complexes ^[23] indeed show significant orbital contributions to the magnetic moment.

In summary, we found significant orbital contributions to the magnetic moment of the transition metals Mn, Fe, Co, and Ni substituted in Li_3N . In accordance, large magnetic anisotropies are observed. A sharp peak of the DOS which is intersected by the Fermi level gives rise to the uniaxial magnetic anisotropy of Fe and Ni. Even though this is not the case for Mn and Co, the latter one does also show a sizable magnetic anisotropy which is, however, of easy-plane type. This behavior can be described in an analytical, single-ion model based on only three parameters: crystal field splitting, spin splitting, and peak width of the DOS. Based on these considerations, it could be possible to identify, or even design, further magnetically ordered transition metal compounds with large orbital magnetic moments and magnetic anisotropy without relying on detailed band structure calculations and excessive computer power.

Acknowledgments

The authors want to thank V. Taufour, A. Kreyssig, S. Thimmaiah, W. R. Meier, and R. W. McCallum for fruitful discussions. This work was supported by the U.S. Department of Energy, Office of Basic Energy Science, Division of Materials Sciences and Engineering. The theoretical work was supported by the U.S. Department of Energy - Energy Efficiency and

Renewable Energy, Vehicles Technology Office, PEEM program. The research was performed at the Ames Laboratory. Ames Laboratory is operated for the U.S. Department of Energy by Iowa State University under Contract No. DE-AC02-07CH11358.

References

- [1] A. Jesche, R. W. McCallum, S. Thimmaiah, J. L. Jacobs, V. Taufour, A. Kreyssig, R. S. Houk, S. Bud'ko and P. C. Canfield, *Nature Commun.* **5:3333** (2014).
- [2] W. Sachsze and R. Juza, *Z. Anorg. Chem.* **259**, 278 (1949).
- [3] A. G. Gordon, D. H. Gregory, A. J. Blake, D. P. Weston and M. O. Jones, *Int. J. Inorg. Mater.* **3**, 973 (2001).
- [4] D. H. Gregory, P. M. O'Meara, A. G. Gordon, D. J. Siddons, A. J. Blake, M. G. Barker, T. A. Hamor and P. P. Edwards, *J. Alloys Compd.* **317-318**, 237 (2001).
- [5] R. Niewa, Z. L. Huang, W. Schnelle, Z. Hu and R. Kniep, *Z. Anorg. Allg. Chem.* **629**, 1778 (2003).
- [6] R. Niewa, Z. Hu and R. Kniep, *Eur. J. Inorg. Chem.* **2003**, 1632 (2003).
- [7] W. Schnelle, R. Niewa and F. R. Wagner, *J. Magn. Magn. Mater.* **272-276**, 828 (2004).
- [8] Z. Stoeva, R. Gomez, D. H. Gregory, G. B. Hix and J. J. Titman, *Dalton Trans.* , 3093 (2004).
- [9] D. -L. Liu, F. Du, Y. -J. Wei, C. -Z. Wang, Z. -Z. Huang, X. Meng, G. Chen, Y. Chen and S. -H. Feng, *Mater. Lett.* **63**, 133 (2009).
- [10] D. Muller-Bouvet, J. -P. Pereira-Ramos, S. Bach, P. Willmann and A. Michalowicz, *Inorg. Chem.* **53**, 6127 (2014).
- [11] P. Novak and F. R. Wagner, *J. Magn. Magn. Mater.* **272-276**, e269 (2004).
- [12] S. Wu, Z. Dong, P. Wu and F. Boey, *J. Mater. Chem.* **21**, 165 (2011).
- [13] V. P. Antropov and V. N. Antonov, *Phys. Reb. B* **90**, 094406 (2014).
- [14] A. Jesche and P. C. Canfield, *Philos. Mag.* **94**, 2372 (2014).
- [15] P. C. Canfield and I. R. Fisher, *J. Cryst. Growth* **225**, 155 (2001).

- [16] C. M. Hurd and P. Coodin, *J. Phys. Chem. Solids* **28**, 523 (1967).
- [17] P. Hohn, S. Hoffmann, J. Hunger, S. Leoni, F. Nitsche, W. Schnelle and R. Kniep, *Chem. Eur. J.* **15**, 3419 (2009).
- [18] J. Klatyk, W. Schnelle, F. R. Wagner, R. Niewa, P. Novak, R. Kniep, M. Waldeck, V. Ksenofontov and P. Gutlich, *Phys. Rev. Lett.* **88**, 207202 (2002).
- [19] P. Novak and F. R. Wagner, *Phys. Rev. B* **66**, 184438 (2002).
- [20] L. Ke and M. van Schilfgaard, ArXiv : 1503.000663.
- [21] H. A. Jahn and E. Teller, *Proc. R. Soc. London, Ser. A* **161**, 220 (1937).
- [22] I. G. Rau, S. Baumann, S. Rusponi, F. Donati, S. Stepanow, L. Gragnaniello, J. Dreiser, C. Piamonteze, F. Nolting, S. Gangopadhyay, O. R. Albertini, R. M. Macfarlane, C. P. Lutz, B. A. Jones, P. Gambardella, A. J. Heinrich and H. Brune, *Science* **344**, 988 (2014).
- [23] P. P. Power, *Chem. Rev.* **112**, 3482 (2012).

Figures and Tables

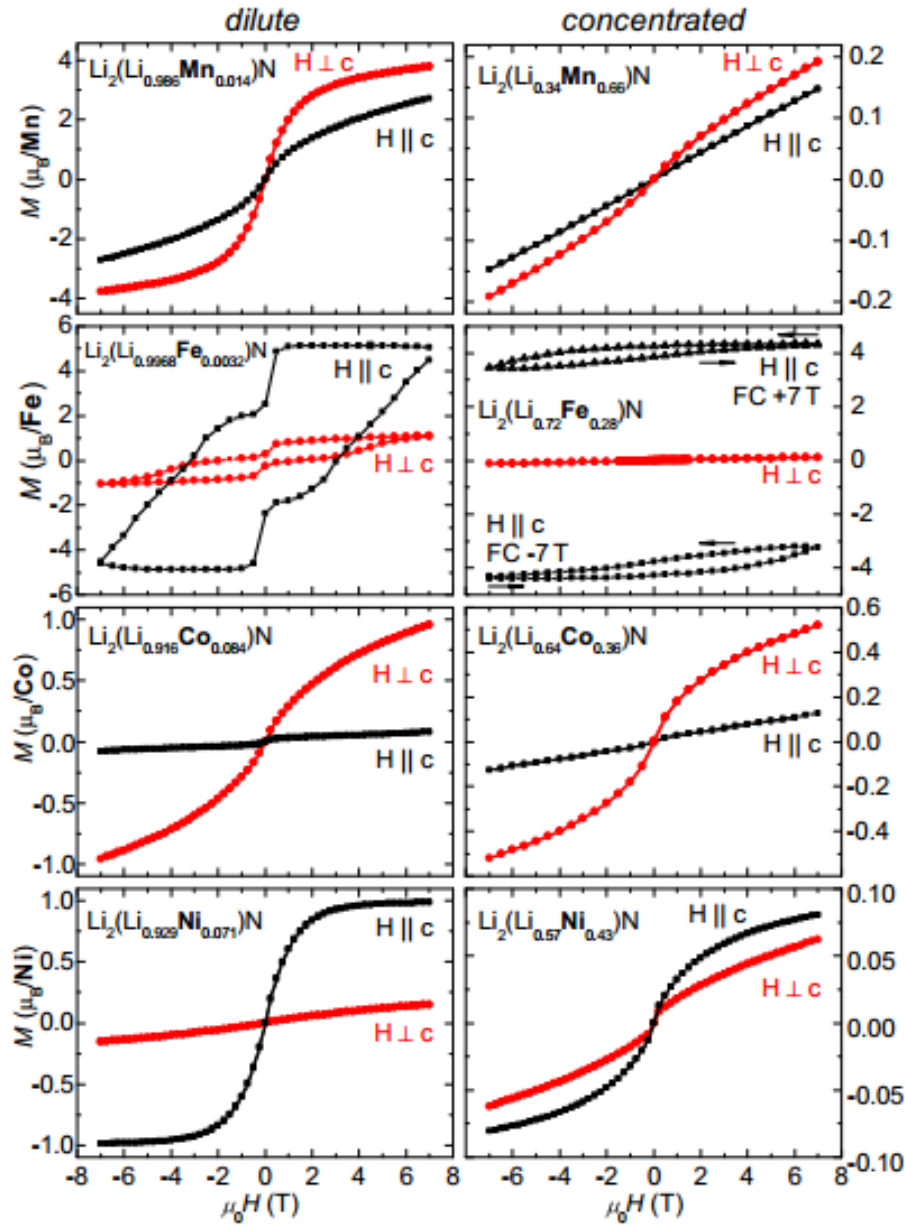


Figure 1: (color online) Isothermal magnetization loops at $T=2\text{K}$ in Bohr magnetons per transition metal ion (FC $\pm 7\text{T}$ refers to a field cooled measurement in $+7\text{T}$ and -7T , respectively). The sign of the magnetic anisotropy changes in an alternating fashion from easy plane to easy axis independent from the concentration of the transition metal.

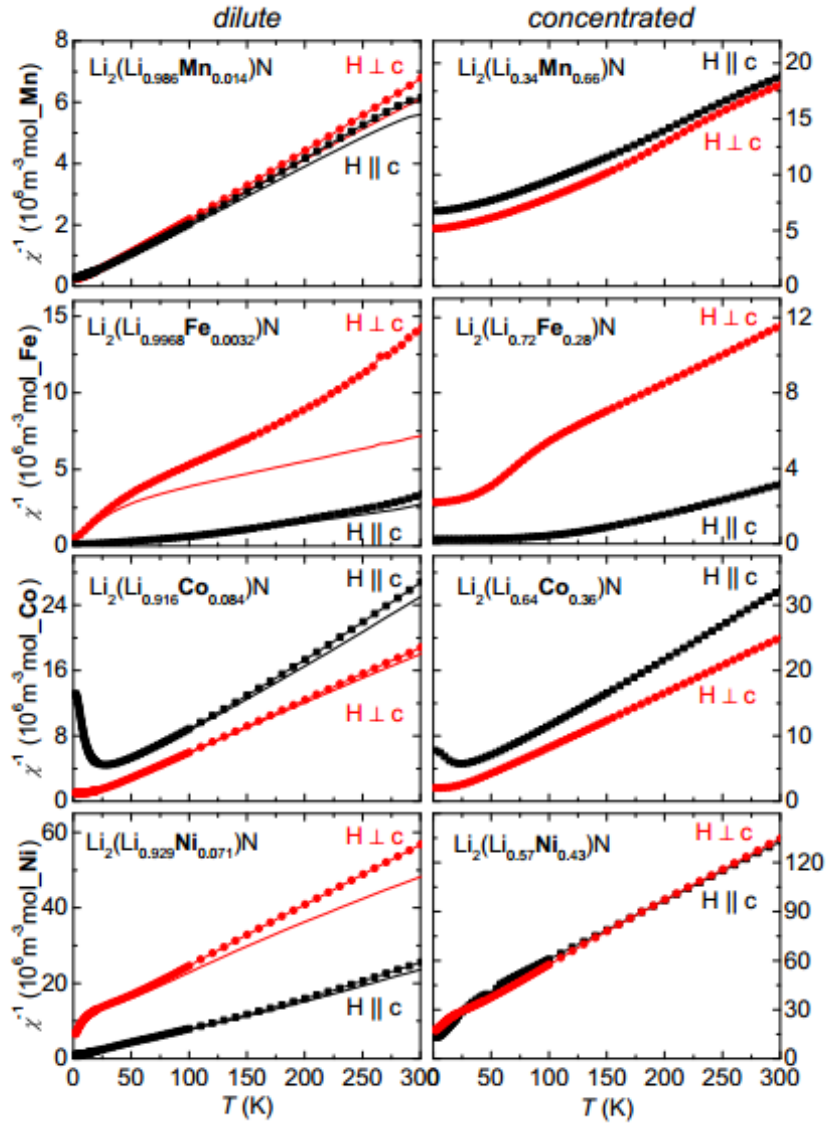


Figure 2: (color online) Inverse magnetic susceptibility per mol transition metal as a function of temperature ($\chi^{-1}=H/M$, $\mu_0 H=7\text{T}$). A pronounced magnetic anisotropy is observed over the whole temperature range except for $T=\text{Mn}$ and concentrated, $T=\text{Ni}$ $\text{Li}_2(\text{Li}_{1-x}\text{T}_x)\text{N}$. The solid lines given for the dilute case (left panel) show the inverse susceptibility after subtracting the core diamagnetism of Li_3N .

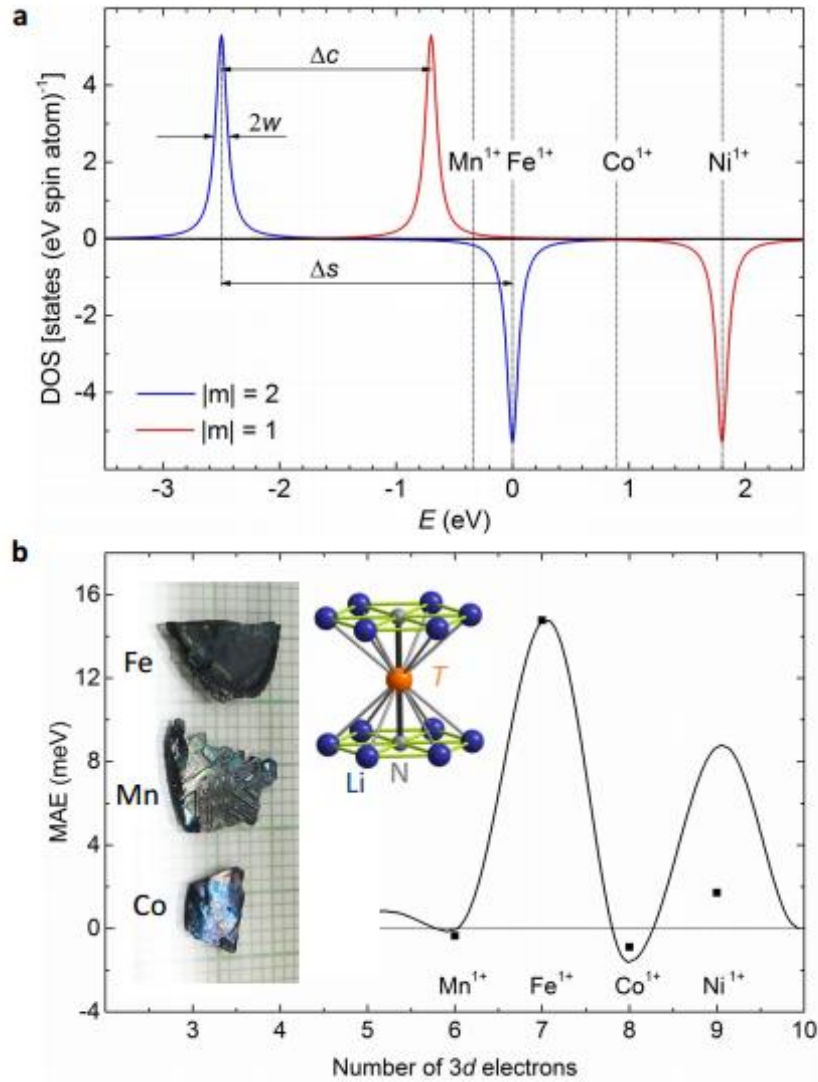


Figure 3: (color online) a) Schematic density of states projected on the $3d$ states of isolated Fe atoms. The MAE in the analytical model is determined by crystal field splitting (Δc), spin splitting (Δs), and peak width (w). For $T=\text{Mn}$, Co, and Ni the position of the Fermi level is shifted according to the number of $3d$ electrons (rigid band approximation). b) The magnetic anisotropy energy (MAE) per isolated T atom as a function of the number of $3d$ electrons calculated in the analytical single-ion model is shown by the solid line. The MAE calculated by LSDA is shown for comparison (black squares). Inset are three single crystals on a millimeter grid and the local crystal structure of the transition metal with nearest and next-nearest neighbors.

Table I: Measured effective magnetic moments per transition metal ion in $\text{Li}_2(\text{Li}_{1-x}\text{T}_x)\text{N}$ and the spin-only value calculated for T^{1+} in units of Bohr magneton.

T	dilute		concentrated		spin-only
	$H\parallel c$	$H\perp c$	$H\parallel c$	$H\perp c$	
Mn	5.5	5.2	3.6	3.6	4.9
Fe	6.7	3.7	6.5	4.6	3.8
Co	2.6	3.1	2.5	2.7	2.8
Ni	2.6	2.0	1.3	1.3	1.7

ACKNOWLEDGEMENTS

This work was performed at the Ames Laboratory under Contract No. DE-AC02-07CH11358 with the U.S. Department of Energy (USDOE). The Aurora Elite instrument and accessories were donated for research purposes by Analytik Jena (formerly Bruker Daltonics). Special thanks to Iouri Kalinitchenko and Andrew Toms for making this research possible.

There are numerous people that I would like to thank for their support during my graduate career at Iowa State University. First of all, thank you to Dr. R. S. Houk for his knowledge, guidance, and instruction over the past 5 years of my research. I can honestly say that I would not have the knowledge that I have today without his advice. I would also like to thank Stan Bajic and Dan Zamzow for their willingness to assist when things weren't quite working like they were supposed to. And last, but definitely not least, I would like to thank the Houk group members, past and present, for their support and friendship over the past 5 years. I am honored to have worked with all of you. I would especially like to thank Jonna Berry who has shared an office with me since the beginning and has helped me maintain my sanity through all the ups and downs of graduate school.

I would like to send a special thank you to my parents, Rod and Lisa Jacobs, for supporting me through my entire life. I consider myself to be very fortunate to have such loving, caring, and selfless people teaching me and helping me grow as an individual. I would also like to thank my "little" brother, Brandon Jacobs, and the rest my very extended family for being my rocks. I would not be who I am today without them in my life as a support system.